

Graph Neural Network Flavour Tagging and Boosted Higgs Measurements at the LHC

Samuel John Van Stroud
University College London

Submitted to University College London in fulfilment
of the requirements for the award of the
degree of **Doctor of Philosophy**

December 2, 2022

Declaration

I, Samuel John Van Stroud confirm that the work presented in this thesis is my own. Where information has been derived from other sources, I confirm that this has been indicated in the thesis.

Samuel Van Stroud

Abstract

This thesis presents investigations into the challenges of, potential improvements to, and the application of b -jet identification at the ATLAS experiment at the Large Hadron Collider (LHC). A focus is placed on the high transverse momentum regime, which is a critical region in which to study the Standard Model, but within which successful b -jet identification becomes difficult.

As b -jet identification relies on the successful reconstruction of charged particle trajectories (tracks), the tracking performance is investigated and potential improvements are assessed. Track reconstruction becomes increasingly difficult at high transverse momentum due to the increased multiplicity and collimation of tracks, and also due to the presence of displaced tracks that may occur as the result of the decay of a long-flying b -hadron. The investigations revealed that the track quality selections applied during track reconstruction are suboptimal for tracks inside high transverse momentum b -jets, motivating future studies into the optimisation of these cuts.

To improve b -tagging performance two novel techniques are employed: the classification of the origin of tracks and the application of graph neural networks. An algorithm has been developed to classify the origin of tracks, which allows a more optimal collection of tracks to be selected for use in other algorithms. A graph neural network (GNN) jet flavour tagger has also been developed. This tagger requires only tracks and jet variables as inputs, making a break from previous algorithms, which relied on the outputs of several other algorithms. This model is trained to simultaneously predict the jet

flavour, track origins, and track-pair compatibility (i.e. vertexing), and demonstrates markedly improvements in b -tagging performance, both at low and high transverse momenta. The closely related task of c-jet identification also benefits from these methods.

Analysis of high transverse momentum $H \rightarrow b\bar{b}$ decays, where the Higgs boson is produced in association with a vector boson, was also performed using 139 fb^{-1} of 13 TeV proton-proton collision data from Run 2 of the LHC. The analysis is described, with a focus on the detailed modelling studies performed by the author. The analysis measured provided first measurements in this channel of the Higgs boson production in two high transverse momentum regions. The impact of applying the improved GNN-based b -tagging algorithms to the analysis is also studied.

Impact Statement

impact statement 500 words [link to ucl info](#)

Acknowledgements

Here is an example of how to declare commands for use in a single file that will not be needed elsewhere. Additionally, it serves to illustrate the chapter referencing system.

J. Shlomi for GNN.

Brian Moser and Francesco Di Bello provided useful guidance and insights into the studies in Chapter 7.

This thesis was made in L^AT_EX 2 _{ε} using the “heptesis” class [1].

Contents

1	Introduction	11
2	Theoretical Framework	13
2.1	The Standard Model	13
2.1.1	Quantum Electrodynamics	14
2.1.2	Quantum Chromodynamics	16
2.1.3	The Electroweak Sector	17
2.2	The Higgs Mechanism	18
2.2.1	Electroweak Symmetry Breaking	19
2.2.2	Fermionic Yukawa Coupling	22
2.2.3	Higgs Sector Phenomenology	24
3	The Large Hadron Collider and the ATLAS Detector	27
3.1	The Large Hadron Collider	28
3.2	Coordinate System & Collider Definitions	29
3.2.1	ATLAS Coordinate System	30
3.2.2	Track Parameterisation	31
3.2.3	Hadron Collider Definitions	31
3.3	The ATLAS Detector	35
3.3.1	Inner Detector	36
3.3.2	Calorimeters	39
3.3.3	Muon Spectrometer	41
3.3.4	The Trigger	42
3.4	Reconstructed Physics Objects	43
3.4.1	Tracks	43
3.4.2	Vertices	45
3.4.3	Jets	47
3.4.4	Leptons	49

3.4.5	Missing Transverse Momentum	50
4	Tracking and b-tagging	52
4.1	b -hadron Reconstruction	53
4.1.1	Decay Topology	53
4.1.2	Challenges Facing b -hadron Reconstruction	55
4.2	Investigations into High p_T b -hadron Tracking	58
4.2.1	Pseudo-tracking	59
4.2.2	Global χ^2 Fitter Outlier Removal	59
4.3	Conclusion	62
5	Track Classification MVA	64
5.1	Machine Learning Background	64
5.1.1	Neural Networks	66
5.1.2	Training with Gradient Descent	67
5.2	Track Truth Origin Labelling	68
5.3	Fake Track Identification Tool	69
5.3.1	Datasets	70
5.3.2	Model Inputs	72
5.3.3	Results	72
5.4	Conclusion	75
6	Graph Neural Network Flavour Tagger	79
6.1	Motivation	80
6.2	Graph Neural Network Theory	83
6.3	Experimental Setup	84
6.3.1	Datasets	84
6.4	Model Architecture	85
6.4.1	Model Inputs	85
6.4.2	Auxiliary Training Objectives	86
6.4.3	Architecture	88
6.4.4	Training	92
6.5	Results	93
6.5.1	b -tagging Performance	94
6.5.2	c -tagging Performance	99
6.5.3	Jet Display Diagrams	100

6.5.4	Ablations	102
6.5.5	Inclusion of Low-Level Vertexing Algorithms	104
6.5.6	Vertexing Performance	107
6.5.7	Track Classification Performance	110
6.5.8	Looser Track Selection	113
6.6	Conclusion	113
7	Boosted VHbb Analysis	118
7.1	Analysis Overview	119
7.1.1	Data & Simulated Samples	120
7.1.2	Object Reconstruction	121
7.1.3	Selection Criteria	123
7.1.4	Control Regions	125
7.1.5	Background Composition	125
7.2	Systematic Uncertainties & Background Modelling	127
7.2.1	Sources of Systematic Uncertainties	128
7.2.2	Implementation of Variations	130
7.2.3	Vector Boson + Jets Modelling	131
7.2.4	Diboson Modelling	138
7.3	Statistical Treatment	140
7.3.1	Likelihood Function	141
7.3.2	Background Normalisations	143
7.3.3	Asimov Dataset & Expected Results	144
7.4	Results	144
7.4.1	Post-fit Distributions	145
7.4.2	Observed Signal Strength & Significance	145
7.4.3	Impact of Systematics	149
7.5	Improved b -tagging using GNNs	152
7.6	Conclusion	152
8	Conclusion	154
Bibliography		155
List of figures		168
List of tables		179

² Chapter 1

³ Introduction

- ⁴ This thesis describes various efforts in improving the understanding of the Higgs boson and its coupling to heavy flavour quarks, primarily through the improvement of the algorithms used to reconstruct and analyse jets.
- ⁷ Chapter 2 describes the theoretical foundations of the work presented in the rest of the thesis.
- ⁹ Chapter 3 describes the ATLAS detector at the CERN accelerator complex. Details of reconstructed physics objects are also provided.
- ¹¹ Chapter 4 provides an overview of tracking and *b*-tagging at ATLAS, and studies into the challenges of high transverse momentum *b*-tagging.
- ¹³ Chapter 5 describes a tool to predict the origins of tracks. The tool is used to improve *b*-tagging performance by the identification and removal of fake tracks before their input to the *b*-tagging algorithms.
- ¹⁶ Chapter 6 introduces a novel monolithic approach to *b*-tagging using graph neural networks and auxiliary training objectives.
- ¹⁸ Chapter 7 describes the measurement of the associated production of a Higgs boson decaying into a pair of *b*-quarks at high transverse momentum.
- ²⁰ Chapter 8 contains some concluding remarks.

- 21 The author's contribution to the work presented in this thesis is as follows.
- 22 **Tracking:** The author was been an active member of the Cluster and Tracking
23 in Dense Environments group for the duration of their qualification task on the
24 understanding of tracking performance at high transverse momentum. The author
25 played a key role in software r22 validation studies for the tracking group, including
26 the validation of the quasi-stable particle interaction simulation and the radiation
27 damage Monte-Carlo simulation. The author helped design and improve several
28 tracking software frameworks, and contributed to heavy flavour tracking efficiency
29 studies in dense environments.
- 30 ***b*-tagging:** The author has been an active member of the Flavour Tagging group
31 since September 2014. The author played a key role in investigating the performance
32 of the low level taggers at high transverse momentum and led studies into the
33 labelling and classification of track origins. Based on work by J. Shlomi, the author
34 helped develop a new flavour tagging algorithm which offers a large performance
35 improvement with respect to the current state of the art. The author also played a key
36 role in software r22 validation studies for the Flavour Tagging group, including the
37 validation of the quasi-stable particle interaction simulation. The author maintains
38 and contributes to various software frameworks used in the Flavour Tagging group,
39 and contributes to group documentation.
- 40 **Higgs:** The author was an active member of the Boosted VHbb analysis group The
41 author performed various studies deriving systematic uncertainties for the $V+jets$
42 and diboson backgrounds. The author also produced and maintained samples, ran fit
43 studies and cross checks, and gave the diboson unblinding approval talk to the Higgs
44 group. The author also contributed to the developement of the analysis software.

⁴⁵ **Chapter 2**

⁴⁶ **Theoretical Framework**

⁴⁷ The Standard Model (SM) of particle physics is the theory describing all known
⁴⁸ elementary particles and their interactions via three of the four fundamental forces.
⁴⁹ Developed by merging the successful theories of quantum mechanics and relativity
⁵⁰ in the second half of the 20th century, the SM's position today at the centre of our
⁵¹ understanding of the nature of the Universe is firmly established by an unparalleled
⁵² level of agreement between the predictions from the model and experimental results
⁵³ [2, 3].

⁵⁴ The SM has predicted the discovery of the top and bottom quarks [4–6], the W
⁵⁵ and Z bosons [7], and the tau neutrino [8]. The last missing piece of the SM to be
⁵⁶ discovered was the Higgs boson, first theorised in the 1960s [9–11], and eventually
⁵⁷ observed at the LHC in 2012 [12, 13]. After its discovery, much ongoing work has
⁵⁸ been carried out performing detailed measurements of its mass and interactions with
⁵⁹ other particles.

⁶⁰ In this chapter, an overview of the SM is given in Section 2.1, and a more detailed
⁶¹ discussion of the Higgs sector and Higgs phenomenology is provided in Section 2.2.

⁶² **2.1 The Standard Model**

⁶³ The SM is formulated in the language of Quantum Field Theory (QFT). In this
⁶⁴ framework, particles are localised excitations of corresponding quantum fields, which
⁶⁵ are operator-valued distributions across spacetime.

Central to QFT is the Lagrangian density which describes the kinematics and dynamics of a field. Observations of conserved quantities are linked, via Noether's theorem, to symmetries which are expressed by the Lagrangian. Alongside Global Poincaré symmetry, the SM Lagrangian observes a local non-Abelian $SU(3)_C \otimes SU(2)_L \otimes U(1)_Y$ gauge symmetry. Gauge symmetries leave observable properties of the system unchanged when the corresponding gauge transformations are applied to the fields. The full Lagrangian of the SM can be broken up into distinct terms corresponding to the different sectors, as in Eq. (2.1). An overview of each sector is given in the following chapters.

$$\mathcal{L}_{\text{SM}} = \mathcal{L}_{\text{EW}} + \mathcal{L}_{\text{QCD}} + \mathcal{L}_{\text{Higgs}} + \mathcal{L}_{\text{Yukawa}} \quad (2.1)$$

The SM provides a mathematical description of how three of the four fundamental forces interact with the matter content of the Universe. The SM contains 12 spin-1/2 fermions, listed in Table 2.1, and five bosons listed in Table 2.2.

Generation	Leptons			Quarks		
	Flavour	Mass [MeV]	Charge [e]	Flavour	Mass [MeV]	Charge [e]
First	e	0.511	-1	u	2.16	$2/3$
	ν_e	$< 1.1 \times 10^{-6}$	0	d	4.67	$-1/3$
Second	μ	105.7	-1	c	1.27×10^3	$2/3$
	ν_μ	< 0.19	0	s	93.4	$-1/3$
Third	τ	1776.9	-1	t	173×10^3	$2/3$
	ν_τ	< 18.2	0	b	4.18×10^3	$-1/3$

Table 2.1: The fermions of the SM [14]. Three generations of particles are present. Also present (unlisted) are the antiparticles, which are identical to the particles up to a reversed charge sign.

77

2.1.1 Quantum Electrodynamics

Quantum electrodynamics (QED) is the relativistic quantum theory which describes the interaction between the photon and charged matter. Consider a Dirac spinor field $\psi = \psi(x)$ and its adjoint $\bar{\psi} = \psi^\dagger \gamma^0$, where ψ^\dagger denotes the Hermitian conjugate of ψ . The field ψ describes fermionic spin-1/2 particle, for example an electron. The

Name	Symbol	Mass [GeV]	Charge [e]	Spin
Photon	γ	$< 1 \times 10^{-27}$	$< 1 \times 10^{-46}$	1
Charged Weak boson	W^\pm	80.377 ± 0.012	± 1	1
Neutral Weak boson	Z	91.1876 ± 0.0021	0	1
Gluon	g	0	0	1
Higgs	H	125.25 ± 0.17	0	0

Table 2.2: The bosons of the SM [14]. The photon, weak bosons and gluons are gauge bosons arising from gauge symmetries, and carry the four fundamental forces of the SM. The recently discovered Higgs boson is the only fundamental scalar particle in the SM.

⁸³ Dirac Lagrangian density is

$$\mathcal{L}_{\text{Dirac}} = \bar{\psi}(i\cancel{\partial} - m)\psi, \quad (2.2)$$

⁸⁴ where $\cancel{\partial} = \gamma^\mu \partial_\mu$ denotes the contraction with the Dirac gamma matrices γ^μ (summation over up-down pairs of indices is assumed). Application of the Euler-Lagrange equation on Eq. (2.2) yields the Dirac equation

$$(i\cancel{\partial} - m)\psi = 0. \quad (2.3)$$

⁸⁷ Suppose some fundamental symmetry that requires invariance under a local $U(1)$
⁸⁸ gauge transformation

$$\psi \rightarrow \psi' = \psi e^{-iq\alpha(x)}, \quad (2.4)$$

⁸⁹ where α varies over every spacetime point x . Under this transformation, the Dirac
⁹⁰ equation transforms as

$$(i\cancel{\partial} - m)\psi e^{-iq\alpha(x)} + q\cancel{\partial}\alpha(x)\psi e^{-iq\alpha(x)} = 0. \quad (2.5)$$

⁹¹ For the Dirac equation to remain invariant under the transformation in Eq. (2.4),
⁹² a new field A_μ which transforms as $A_\mu \rightarrow A'_\mu = A_\mu + \partial_\mu \alpha(x)$ must be added. The
⁹³ transformed interaction term

$$-q\cancel{A}\psi \rightarrow -q\cancel{A}\psi e^{-iq\alpha(x)} - q\cancel{\partial}\alpha(x)\psi e^{-iq\alpha(x)} \quad (2.6)$$

will then cancel the asymmetric term in Eq. (2.5) as required. The $U(1)$ invariant Lagrangain can therefore be constructed by adding an interaction between ψ and A_μ to Eq. (2.2). For completeness, the kinetic term for the new field A_μ is also added in terms of $F_{\mu\nu} = \partial_\mu A_\nu - \partial_\nu A_\mu$, which is trivially invariant under the transformation in Eq. (2.4). The interaction term is typically absorbed into the covariant derivative $D_\mu = \partial_\mu + iqA_\mu$, thus named as it transforms in the same way as the field ψ . Collecting these modifications to Eq. (2.2) yields the QED Lagrangain

$$\mathcal{L}_{\text{QED}} = -\frac{1}{4}F_{\mu\nu}F^{\mu\nu} + \bar{\psi}(iD^\mu - m)\psi. \quad (2.7)$$

The quadratic term $A_\mu A^\mu$ is not invariant and therefore the field A_μ must be massless. Requiring invariance under local $U(1)$ gauge transformations necessitated the addition of a new field A_μ , interpreted as the photon field, which interacts with charged matter. In the SM, the QED Lagrangian is absorbed into the electroweak sector, discussed in Section 2.1.3.

2.1.2 Quantum Chromodynamics

Quantum Chromodynamics (QCD) is the study of quarks, gluons and their interactions. Quarks and gluons carry colour charge, which comes in three kinds, called red, green and blue. While the $U(1)$ symmetry group in Section 2.1.1 was Abelian, the QCD Lagrangian is specified by requiring invariance under transformations from the non-Abelian $SU(3)$ group, making it a Yang-Mills theory [15] which requires the addition of self-interacting gauge fields. The infinitesimal $SU(3)$ group generators are given by $T_a = \lambda_a/2$, where λ_a are the eight Gell-Mann matrices. These span the space of infinitesimal group transformations and do not commute with each other, instead satisfying the commutation relation

$$[T_a, T_b] = if_{abc}T_c, \quad (2.8)$$

where f_{abc} are the group's structure constants. Consider the six quark fields $q_k = q_k(x)$. Each flavour of quark q_k transforms in the fundamental triplet representation, in which each component of the triplet corresponds to the colour quantum number for red, green and blue colour charged respectively. $G_{\mu\nu}^a$ are the eight gluon field

120 strength tensors, one for each generator T_a , defined as

$$G_{\mu\nu}^a = \partial_\mu A_\nu - \partial_\nu A_\mu - g_s f^{abc} A_\mu^b A_\nu^c, \quad (2.9)$$

121 where A_μ^a are the gluon fields and g_s is the strong coupling constant. The covariant
122 derivative is written as

$$D_\mu = \partial_\mu + i g_s T_a A_\mu^a. \quad (2.10)$$

123 The full QCD Lagrangian is then given by

$$\mathcal{L}_{\text{QCD}} = -\frac{1}{4} G_{\mu\nu}^a G_a^{\mu\nu} + q_k (i \not{D} - m_k) q_k. \quad (2.11)$$

124 Cubic and quartic terms of the gauge fields A_μ^a appear in the Lagrangian, leading to
125 the gluon's self interaction.

126 The QCD coupling constant g_s varies, or “runs”, with energy. At lower energy
127 scales (and corresponding larger distance scales) the interaction is strong. This
128 leads to quark confinement, whereby an attempt to isolate individual colour-charged
129 quarks requires so much energy that additional quark-antiquark are produced. At
130 higher energy scales (and corresponding smaller distance scales), asymptotic freedom
131 occurs as the interactions become weaker, allowing perturbative calculations to be
132 performed. Hadrons are bound states of quarks. They are invariant under $SU(3)$
133 gauge transformations (i.e. are colour-charge neutral, or *colourless*).

134 2.1.3 The Electroweak Sector

135 The weak and electromagnetic forces are unified in the Glashow-Weinberg-Salam
136 (GWS) model of electroweak interaction [16–18]. The Lagrangian is specified by
137 requiring invariance under the symmetry group $SU(2)_L \otimes U(1)_Y$, as motivated by a
138 large amount of experimental data. Here, $SU(2)_L$ is referred to as weak isospin and
139 $U(1)_Y$ as weak hypercharge.

- 140 The generators of $SU(2)_L$ are $T_a = \sigma_a/2$, where σ_a are the three Pauli spin matrices
141 which satisfy the commutation relation

$$[T_a, T_b] = i\varepsilon_{abc}T_c. \quad (2.12)$$

- 142 The generator of $U(1)_Y$ is $Y = 1/2$. Each generator corresponds to a gauge field,
143 which, after symmetry breaking (discussed in Section 2.2), give rise to the massive
144 vector bosons, W^\pm and Z , and the massless photon. The massive vector bosons
145 are the carriers of the weak force. Due to the mass of the force carriers, the weak
146 force has a short range and so it appears weak even though its intrinsic strength is
147 comparable to that of QED.

- 148 The charge operator Q can be written as a combination of the third $SU(2)_L$ generator
149 and the $U(1)_Y$ generator as in

$$Q = T_3 + Y. \quad (2.13)$$

- 150 The weak force violates parity conservation [19–21], i.e. invariance under parity
151 transformations (mirror reflections). Only left handed fermions participate in the
152 weak interaction. Since there is no other force through which neutrinos interact with
153 other particles, there are no right handed neutrinos in the standard model.

154 2.2 The Higgs Mechanism

- 155 The Brout-Englert-Higgs mechanism (henceforth just “Higgs mechanism”) is the
156 mechanism through which the fundamental particles of the SM acquire mass [9–11].
157 Experimentally it was known that the weak force had a weak effective strength,
158 which was suggestive of a massive mediating gauge particle. However, directly
159 adding mass to the weak gauge bosons violates the non-Abelian symmetry of the
160 SM. Instead, the gauge bosons can gain mass through the interaction with a scalar
161 Higgs field which results from the spontaneous breakdown of symmetry as discussed
162 in Section 2.2.1. Similarly, the Higgs mechanism gives mass to the fermions, as
163 discussed in Section 2.2.2. Section 2.2.3 described some basic phenomenology of the
164 Higgs particle relevant to hadron colliders.

¹⁶⁵ 2.2.1 Electroweak Symmetry Breaking

¹⁶⁶ Spontaneous symmetry breaking (SSB) is a key part of the Higgs mechanism. It
¹⁶⁷ is the transition of a physical system from a state of manifest symmetry to a state
¹⁶⁸ of hidden, or *broken*, symmetry. In particular, this applies to physical systems
¹⁶⁹ where the Lagrangian observes some symmetry, but the lowest energy vacuum states
¹⁷⁰ do not exhibit that same symmetry. In other words, the symmetry is broken for
¹⁷¹ perturbations around the vacuum state.

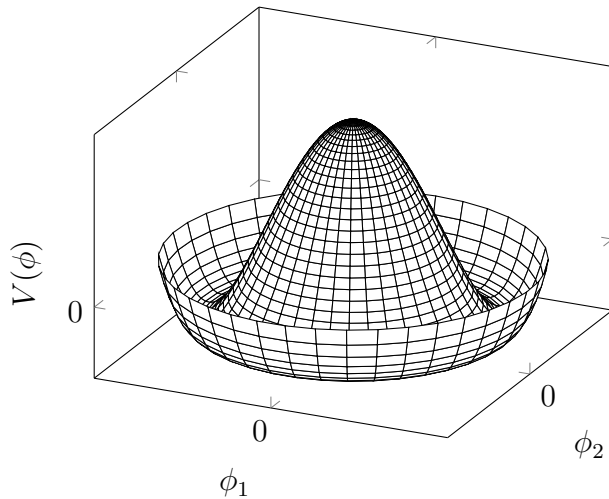


Figure 2.1: The Higgs potential $V(\phi)$ of the complex scalar field singlet $\phi = \phi_1 + i\phi_2$, with a choice of $\mu^2 < 0$ leading to a continuous degeneracy in the true vacuum states. A false vacuum is present at the origin. The SM Higgs mechanism relies on a complex scalar doublet with a corresponding 5-dimensional potential.

¹⁷² Consider gauge fields from the local $SU(2)_L \otimes U(1)_Y$ symmetry group discussed in
¹⁷³ Section 2.1.3 coupled to a complex scalar field $\phi = \phi(x)$. The scalar field ϕ transforms
¹⁷⁴ as a weak isospin doublet. Omitting the kinetic term of the gauge fields, and writing
¹⁷⁵ $\phi^2 \equiv \phi^\dagger \phi$, the Lagrangian is

$$\mathcal{L}_{\text{Higgs}} = (D_\mu \phi)^\dagger (D^\mu \phi) - [\mu^2 \phi^2 + \lambda \phi^4], \quad (2.14)$$

¹⁷⁶ where the covariant derivative is given by

$$D_\mu = \partial_\mu + igA_\mu^a T^a + ig' B_\mu, \quad (2.15)$$

and T^a are the generators of $SU(2)$. The potential term $V(\phi)$ is made up of a quadratic and quartic term in the scalar field ϕ , which each contain an arbitrary parameter, respectively λ and μ . The quartic term gives the field self-interaction, and cannot be negative as this would lead to a potential that was unbounded from below. The quadratic term can be positive or negative. In the case where the quadratic term is positive, it is interpreted as a mass term for the scalar field. By choosing $\mu^2 < 0$ the field becomes unphysical due to its negative mass. In order to obtain a physical interpretation of the Lagrangian in Eq. (2.14) for the case where $\mu^2 < 0$, the field ϕ is expanded around the vacuum state. The vacuum expectation value (VEV) is the expected value of the field ϕ which minimises the potential $V(\phi)$ (equivalently the expected value of the field operator ϕ when the system is in a vacuum state, $|\langle \phi \rangle_0|^2 \equiv |\langle 0 | \phi | 0 \rangle|^2 \equiv \phi_0^2$). Minimising the potential gives a VEV of

$$\phi_0^2 = -\mu^2/\lambda = v^2. \quad (2.16)$$

Due to the shape of the potential in Fig. 2.1, there is a degeneracy in the direction that the complex doublet ϕ points. As all the different vacuum states minimise the potential and therefore yield identical physics, one can arbitrarily choose the state to lie along the second component of the doublet. Application of Eq. (2.13) shows this choice is manifestly invariant under the charge operator. This allows the identification of the unbroken subgroup $U(1)_Q$, under which the ground state is invariant. The generator of $U(1)_Q$ is the charge operator Q .

Adding the particle content back to the theory by expanding the field around the vacuum state, and making a transformation to the unitary gauge to remove unphysical Nambu-Goldstone modes (which arise in the context of global symmetries [22, 23]), yields

$$\phi = \frac{1}{\sqrt{2}} \begin{bmatrix} 0 \\ v + H \end{bmatrix}, \quad (2.17)$$

where H is a real scalar field, the *true vacuum* Higgs field. Substituting this into Eq. (2.14) and identifying physical fields from the quadratic terms of linear combinations of unphysical fields, one can write the physical fields W_μ^\pm , Z_μ and A_μ

203 in terms of the original fields A_μ^a and B_μ . This gives

$$W_\mu^\pm = \frac{1}{\sqrt{2}}(A_\mu^1 \mp iA_\mu^2) \quad \begin{bmatrix} A_\mu \\ Z_\mu \end{bmatrix} = \begin{bmatrix} \cos \theta_W & \sin \theta_W \\ -\sin \theta_W & \cos \theta_W \end{bmatrix} \begin{bmatrix} B_\mu \\ A_\mu^3 \end{bmatrix}. \quad (2.18)$$

204 where θ_W is the weak mixing angle defined by

$$\cos \theta_W = \frac{g}{\sqrt{g^2 + g'^2}}. \quad (2.19)$$

205 The corresponding masses of the now massive vector bosons can be read off as

$$m_W = \frac{1}{2}gv \quad m_Z = \frac{m_W}{\cos \theta_W}, \quad (2.20)$$

206 while the photon remains massless. The Higgs mass is $m_H = v\sqrt{\lambda} = \mu$.

207 This is the Higgs mechanism. It maintains the renormalisability and unitarity of
208 the SM whilst allowing the weak vector bosons to acquire mass. In summary, an
209 unphysical complex scalar field ϕ with a nonzero VEV leads to spontaneous symmetry
210 breaking. Due to the non-Abelian symmetry breaking, would-be massless Nambu-
211 Goldstone modes, which arise after expansion around the true vacuum state, are
212 exactly cancelled out by making a local gauge transformation to the unitary gauge,
213 and instead are absorbed by the vector bosons, allowing them to acquire mass.

214 This sector of the SM contains four fundamental parameters that must be determined
215 from experiment. These can be specified by the Lagrangian parameters g , g' , v
216 and λ or the physically measurable parameters m_Z , $\sin \theta_W$, m_H and e . In the
217 local neighbourhood around the true vacuum, the macroscopic symmetry of the
218 system is not realised, and therefore the physical particles do not obey the original
219 symmetry. However, information about the symmetry is retained through some
220 additional constraints on the parameters of the theory. Prior to symmetry breaking,
221 the potential contained two terms and two constants. After symmetry breaking
222 there are three terms but still only two constants that relate these terms. This is the
223 vestige of the original symmetry.

224 Spontaneous symmetry breaking has modified the original symmetry group of the SM
225 $SU(2)_L \times U(1)_Y \rightarrow SU(3)_C \otimes U(1)_Q$. Three broken generators from the symmetry
226 group $SU(2)_L \times U(1)_Y$ have been absorbed into the definition of the physical weak

227 vector bosons, giving them mass. The same methodology can be used to generate
228 the fermion masses, as shown in the next section.

229 2.2.2 Fermionic Yukawa Coupling

230 Adding the masses of the fermions by hand breaks the gauge invariance of the
231 theory. Instead, we can use a Yukawa coupling between the fermion fields and the
232 Higgs field in order to generate mass terms after spontaneous electroweak symmetry
233 breakdown [17]. In this way, the fermion masses are determined by both the respective
234 couplings to the Higgs field and the VEV of the Higgs field itself, which sets the
235 basic mass scale of the theory.

236 The Higgs field ϕ transforms as an $SU(2)$ doublet with $Y = 1/2$, as does the left-
237 handed fermion field ψ_L . The right-handed fermion field ψ_R transforms as an $SU(2)$
238 singlet.

239 Lepton Masses

240 The renormalisable and gauge invariant coupling between a fermionic field ψ and a
241 scalar Higgs field ϕ can be written as

$$\mathcal{L}_{\text{Yukawa}} = -g_f(\bar{\psi}_L \phi \psi_R + \bar{\psi}_R \phi^\dagger \psi_L). \quad (2.21)$$

242 where $\psi_L = (\nu_L, e_L)$ and $\psi_R = e_R$ for the first generation leptons. After spontaneous
243 symmetry breaking (see Section 2.2.1), the scalar Higgs field in unitary gauge
244 Eq. (2.17) consists of a VEV and the true vacuum Higgs field H . Substituting this
245 in to Eq. (2.21) yields

$$\mathcal{L}_{\text{Yukawa}} = -\frac{v g_e}{\sqrt{2}} \bar{e} e - \frac{g_e}{\sqrt{2}} \bar{e} H e, \quad (2.22)$$

246 using $\bar{e} e = (\bar{e}_L + \bar{e}_R)(e_L + e_R) = \bar{e}_L e_R + \bar{e}_R e_L$. The VEV component of ϕ provides
247 the first term in Eq. (2.22) which is quadratic in the electron field, and can therefore
248 be identified as the electron mass term. An interaction term between the electron
249 field e and the true vacuum Higgs field H is also present. Mass is generated for the
250 other lepton generations in the same way.

251 Quark Masses

252 The down-type quarks acquire their mass analogous to the leptons, with $\psi_L = (u_L, d_L)$
 253 and $\psi_R = d_R$ for the first quark generation. Mass is generated for the up-type quarks
 254 using the conjugate field to ϕ which transforms under $SU(2)$ as a doublet with
 255 $Y = -1/2$. The conjugate field $\tilde{\phi}$ is constructed as

$$\tilde{\phi} = i\sigma_2 \phi^\dagger = \begin{bmatrix} 0 & 1 \\ -1 & 0 \end{bmatrix} \begin{bmatrix} \phi_1^\dagger \\ \phi_2^\dagger \end{bmatrix} = \frac{1}{\sqrt{2}} \begin{bmatrix} v + H \\ 0 \end{bmatrix}, \quad (2.23)$$

256 and transforms in the same way as ϕ . This field can be used to write an additional
 257 Yukawa coupling which provides mass for the up-type quarks in a similar way as
 258 before.

$$\mathcal{L}_{\text{Yukawa}}^{\text{up}} = -g_q (\bar{\psi}_L \tilde{\phi} \psi_R + \bar{\psi}_R \tilde{\phi}^\dagger \psi_L) \quad (2.24)$$

259 Considering the first generation of up-type quarks with $\psi_L = (u_L, d_L)$ and $\psi_R = u_R$,
 260 substitution into Eq. (2.24) yields

$$\mathcal{L}_{\text{Yukawa}}^{\text{up}} = -\frac{vg_u}{\sqrt{2}} \bar{u}u - \frac{g_u}{\sqrt{2}} \bar{u}Hu. \quad (2.25)$$

261 The Yukawa terms mix quarks of different generations of lepton and quark. Physical
 262 particles are detected in their mass eigenstates q , which diagonalise the mass matrix,
 263 but interact via the weak interaction according to their weak eigenstates \tilde{q} , which
 264 are superpositions of the mass eigenstates. This feature of the weak sector leads to
 265 mixing between different generations of quarks and leptons. Quark mixing can be
 266 expressed using the Cabibbo-Kobayashi-Maskawa (CKM) matrix, which specifies the
 267 strength of flavour-changing weak currents. The entries in the matrix are enumerated
 268 as

$$\begin{bmatrix} \tilde{d} \\ \tilde{s} \\ \tilde{b} \end{bmatrix} = \begin{bmatrix} V_{ud} & V_{us} & V_{ub} \\ V_{cd} & V_{cs} & V_{cb} \\ V_{td} & V_{ts} & V_{tb} \end{bmatrix} \begin{bmatrix} d \\ s \\ b \end{bmatrix}, \quad (2.26)$$

269 where the size of the elements $|V_{pq}|^2$ measures the probability of a transition between
 270 states p and q .

2.2.3 Higgs Sector Phenomenology

As previous discussed in this section, the Higgs field plays a key role in the SM, giving mass to fundamental particles. The strength of the coupling between the Higgs field and another particle is proportional to that particle's mass. This fact dictates which production mechanisms and decay modes are dominant at the LHC. The cross sections for different production mechanisms at a centre of mass energy $\sqrt{s} = 13$ TeV are shown as a function of the Higgs mass m_H in Fig. 2.3. Higgs boson production occurs mainly through four modes, shown in Fig. 2.2. The dominant production mode is gluon-gluon fusion ($pp \rightarrow H$), which is predominantly mediated by a virtual top quark loop. Vector boson fusion ($pp \rightarrow qqH$) is the second most dominant production mechanism, in which a pair of W or Z bosons fuse to produce a Higgs after being radiated by two quarks, which also occur in the final state. Next most common is the associated production of a Higgs boson and a vector boson ($pp \rightarrow VH$), in which a pair of quarks fuse to produce a single W or Z boson which radiates a Higgs. The final of the four leading production modes is top quark fusion, in which two gluons each radiate a quark-antiquark pair, and a quark from each pair fuses to produce a Higgs boson.

Although gluon-gluon fusion is the dominant production mode, for hadronic decays of the Higgs boson the associated production with a vector boson has the advantage of leading to a more conspicuous final state due to the likelihood of the vector bosons decaying leptons. Leptons provide a clean signals to detect and trigger on.

Since the Higgs boson couples proportional to mass as already mentioned, decays to heavier particles are favoured. The branching ratios of different Higgs boson decay modes are shown as a function of m_H in Fig. 2.4. Approximately 58% of the time the Higgs boson decays to a pair of b -quarks, the dominant decay mode. The next heaviest fermions are the tau lepton and the c -quark, decays to pairs of these particles happen approximately an order of magnitude less often. Decays to pairs of vector bosons are via a virtual off shell Higgs boson only. While the $H \rightarrow \gamma\gamma$ and $H \rightarrow ZZ$ branching ratios are small compared with fermionic decay modes (around 0.2% for $H \rightarrow \gamma\gamma$), these decay channels were instrumental in the initial discovery of the Higgs due to the low level of background processes which mimic the final state.

This thesis presents a measurement of the Higgs bosons production rate using events with a Higgs boson produced in association with vector boson and decaying to a pair

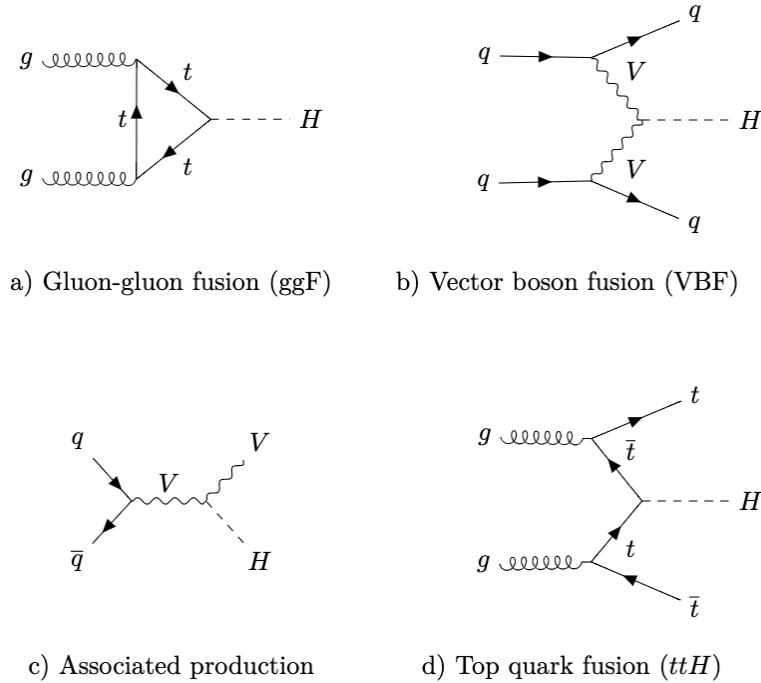


Figure 2.2: Diagrams for the four main Higgs boson production modes at the LHC for a Higgs mass $m_H = 125$ GeV at a centre of mass energy $\sqrt{s} = 13$ TeV.

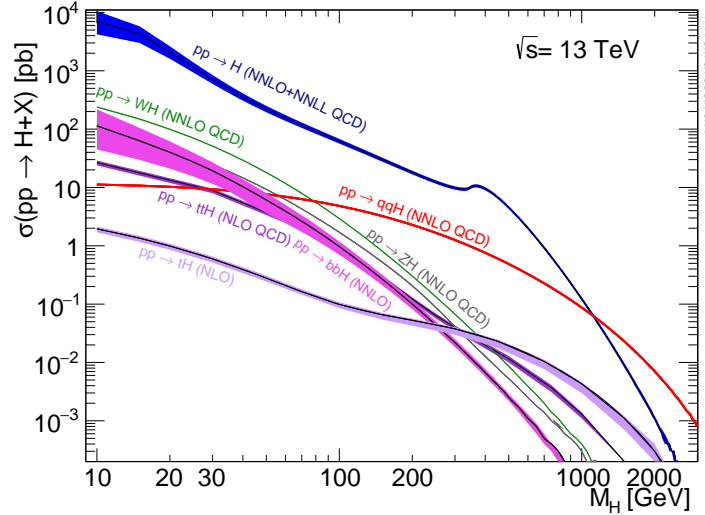


Figure 2.3: Higgs boson production cross sections as a function of Higgs mass (m_H) at $\sqrt{s} = 13$ TeV [24]. Uncertainties are shown in the shaded bands. At $m_H = 125$ GeV, Higgs boson production is dominated by gluon-gluon fussion, vector boson fusion, associated production with vector bosons, and top quark fusion.

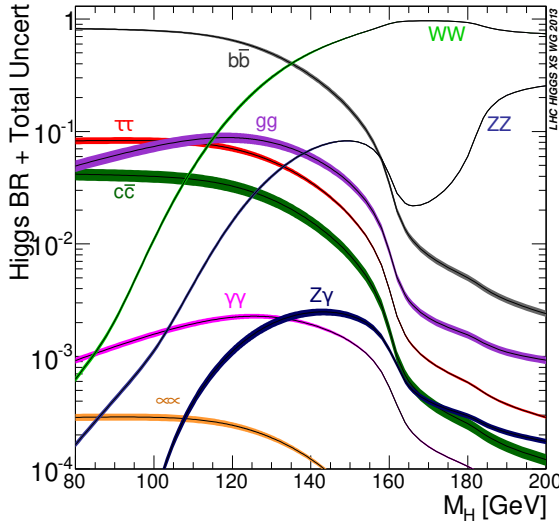


Figure 2.4: Higgs boson branching ratios as a function of Higgs mass (m_H) at $\sqrt{s} = 13 \text{ TeV}$ [24]. Uncertainties are shown in the shaded bands. At $m_H = 125 \text{ GeV}$, the Higgs predominantly decays to a pair of b -quarks, around 58% of the time. The leading subdominant decay mode is to a pair of W bosons.

of b -quarks, i.e. $pp \rightarrow VH(b\bar{b})$. The $H \rightarrow b\bar{b}$ decay mode directly probes the Higgs coupling to the second generation fermions, and more specifically to the bottom quark. This coupling was first observed in 2018 [25, 26]. Ongoing work measuring the coupling strengths, in particular in the high energy regime, is the focus of the analysis presented in this thesis in Chapter 7.

309 Chapter 3

310 The Large Hadron Collider and the
311 ATLAS Detector

312 Since the completion of its construction in 2008, the Large Hadron Collider (LHC) [27]
313 at CERN has extended the frontiers of particle physics through its unprecedented
314 energy and luminosity. The LHC accelerates protons around a 27 km ring until they
315 are travelling just 3 m s^{-1} slower than the speed of light, at which point they
316 are made to collide. The protons travel round the ring 11,000 times per second in
317 two concentric beams, which are guided by superconducting magnets cooled using
318 liquid helium to -271.3°C (1.9 K). The beams travel in opposite directions around
319 the ring and are crossed at four locations so that collisions between protons can
320 take place. Around these collision points four specialised detectors, ALICE [28],
321 CMS [29], LHCb [30] and ATLAS [31], are located to capture information about the
322 products of the collisions.

323 In this chapter, a brief overview of the LHC and the accelerator complex at CERN
324 is given in Section 3.1. The coordinate system used at the ATLAS detector and
325 other common definitions are introduced in Section 3.2. Next, an overview of the
326 different detector systems is provided in Section 3.3, and finally descriptions of
327 various commonly used reconstructed objects is given in Section 3.4.

³²⁸ 3.1 The Large Hadron Collider

³²⁹ The LHC is operated in multi-year *runs* during which beams of protons are circulated
³³⁰ and collided. Between runs there are periods of shutdown while the accelerator and
³³¹ detector machinery is maintained and upgraded. Run 1 began in 2010 when the LHC
³³² collided proton bunches, each containing more than 10^{11} particles, 20 million times
³³³ per second, providing 7 TeV proton-proton collisions at instantaneous luminosities
³³⁴ of up to $2.1 \times 10^{32} \text{ cm}^{-2} \text{ s}^{-1}$. The centre-of-mass energy was increased to 8 TeV
³³⁵ towards the end of Run 1 in 2012. Run 2, which spanned in 2015–2018, further
³³⁶ increased the the proton-proton collision energy to 13 TeV. During Run 2 the bunch
³³⁷ spacing was reduced, leading to a collisison rate of 40 MHz. Over the course of
³³⁸ Run 2 a total usable integrated luminosity of 139 fb^{-1} was recorded. 2022 marked the
³³⁹ beginning of Run 3 which, with a higher center of mass energy and peak luminosity,
³⁴⁰ is expected to culminate in the approximate tripling of the dataset size. A summary
³⁴¹ of key information about each run is listed in Table 3.1.

Period	Year	\sqrt{s} [TeV]	$\langle\mu\rangle$	Bunch spacing [ns]	Luminosity [$\text{cm}^{-2} \text{ s}^{-1}$]
Run 1	2010–2012	7–8	18	50	8×10^{33}
Run 2	2015–2018	13	34	25	$1\text{--}2 \times 10^{34}$
Run 3	2022–2025	13.6	50	25	2×10^{34}

Table 3.1: Overview of the different LHC runs [32,33]. The average number of interactions per bunch-crossing is denoted as $\langle\mu\rangle$ (see Section 3.2.3), and is here averaged over the entire run. Numbers for Run 3 are preliminary and are only provided to give an indication of expected performance.

³⁴² An overview of the accelerator complex at CERN is shown in Fig. 3.1. The LHC is
³⁴³ at the final stage of a chain of accelerators which incrementally step-up the energy
³⁴⁴ of incoming protons. The first accelerator is Linac4, a linear accelerator which
³⁴⁵ accelerates negative hydrogen ions to an energy of 160 MeV. Upon leaving Linac4,
³⁴⁶ the ions are stripped of both electrons and the resulting protons are fed into the
³⁴⁷ Proton Synchrotron Booster (PSB), which increases the energy of the protons to
³⁴⁸ 2 GeV. The protons leaving the PSB are passed to the Proton Synchrotron (PS),
³⁴⁹ which increases the energy to 26 GeV, and then from the PS to the Super Proton
³⁵⁰ Synchrotron (SPS) which further increases the energy to 450 GeV. Finally, the proton

³⁵¹ beams are injected in the LHC where they are accelerated to their final energy of
³⁵² 6.5 TeV (for Run 2).

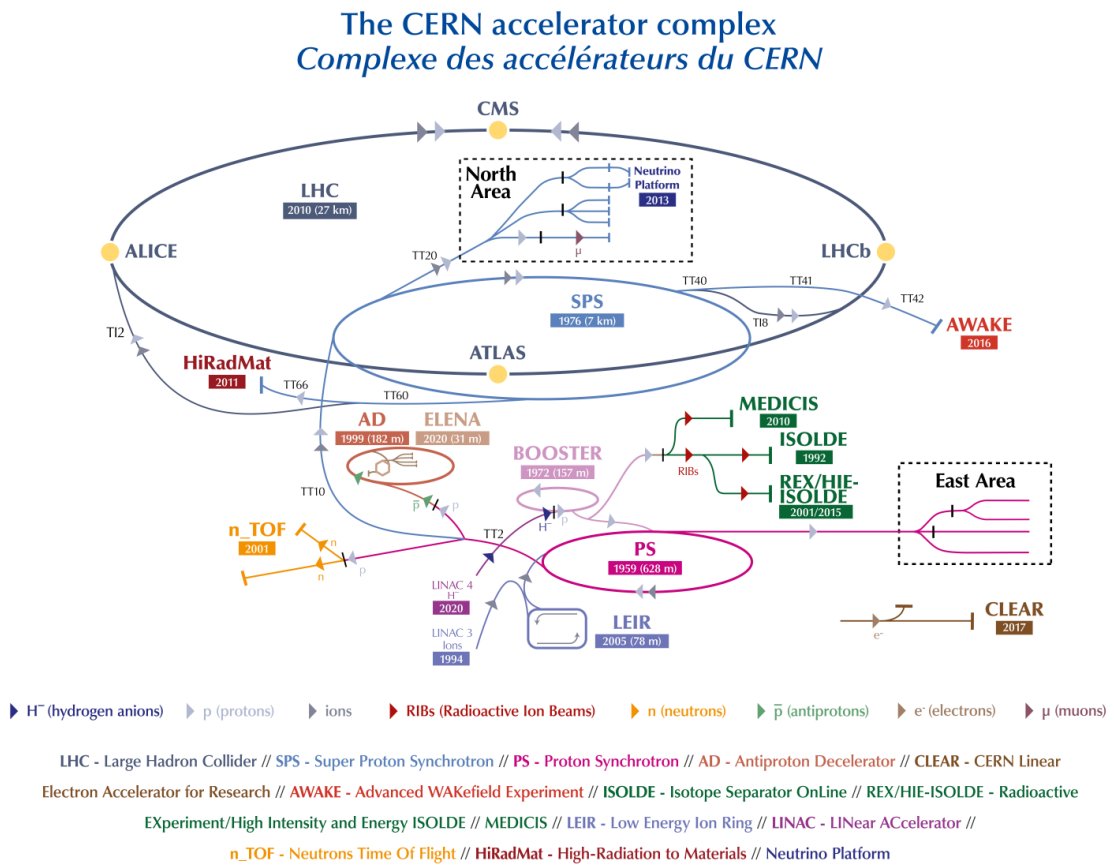


Figure 3.1: An overview of the CERN accelerator complex [34]. The LHC is fed by a series of accelerators starting with Linac4. Next are the Proton Synchrotron Booster, the Proton Synchrotron, and finally the Super Proton Synchrotron which injects protons into the LHC.

³⁵³ 3.2 Coordinate System & Collider Definitions

354 In Section 3.2.1, the coordinate system used at ATLAS is introduced. The parameter-
355 isation used for the specifying the trajectory of charged particle tracks is described in
356 Section 3.2.2, and definitions for some frequently occurring concepts and quantities
357 is provided in Section 3.2.3.

358 3.2.1 ATLAS Coordinate System

359 The origin of the coordinate system used by ATLAS is the nominal interaction point
 360 in the centre of the detector. As shown in Fig. 3.2, the z -axis points along the
 361 direction the beam pipe, while the x -axis points from the interaction point to the
 362 centre of the LHC ring, and the y -axis points upwards. The transverse plane lies
 363 in x - y while the longitudinal plane lies along the z -axis. A cylindrical coordinate
 364 system with coordinates (r, ϕ) is used in the transverse plane, where r is the radius
 365 from the origin and ϕ is the azimuthal angle around the z -axis.

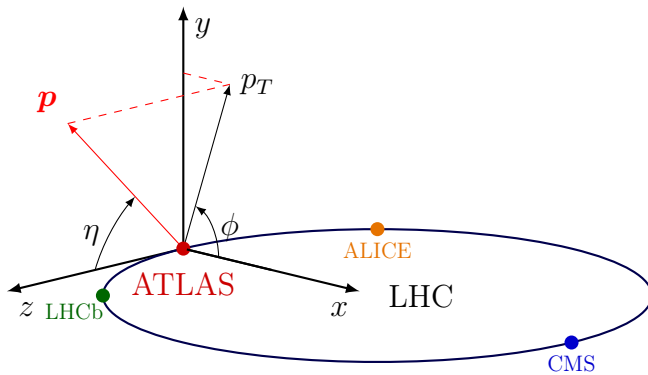


Figure 3.2: The coordinate system used at the ATLAS detector, showing the locations of the four main experiments located at various points around the LHC. The 3-vector momentum $\mathbf{p} = (p_x, p_y, p_z)$ is shown by the red arrow. Reproduced from Ref. [35].

366 The polar angle θ is commonly specified in terms of the pseudorapidity η , defined as

$$\eta = -\ln \left[\tan \left(\frac{\theta}{2} \right) \right]. \quad (3.1)$$

367 The pseudorapidity is a convenient quantity to work with as differences in η are
 368 invariant under Lorentz boosts. In addition, particle production is constant as a
 369 function of η .

370 The transverse momentum p_T of an object is the sum in quadrature of the momenta
 371 in the transverse plane

$$p_T = \sqrt{p_x^2 + p_y^2}. \quad (3.2)$$

³⁷² Angular distance between two objects is measured in units of ΔR and is defined as
³⁷³ the sum in quadrature of the η and ϕ displacements

$$\Delta R = \sqrt{(\Delta\eta)^2 + (\Delta\phi)^2}. \quad (3.3)$$

³⁷⁴ 3.2.2 Track Parameterisation

³⁷⁵ The trajectories of charged particle tracks are parameterised as a helix which is
³⁷⁶ fully specified using five parameters: $(d_0, z_0, \phi, \theta, q/p)$. Transverse and longitudinal
³⁷⁷ impact parameters (IP) d_0 and z_0 specify the closest approach of the trajectory of
³⁷⁸ a particle to the origin. The transverse IP d_0 and longitudinal IP z_0 are measured
³⁷⁹ with respect to the hard scatter primary vertex (see Section 3.4.2). ϕ and θ are
³⁸⁰ the azimuthal and polar angles respectively, and q/p is the measured charge on the
³⁸¹ track¹ divided by the scalar 3-momentum. Fig. 3.3 shows each of these parameters
³⁸² diagrammatically.

³⁸³ Impact parameter significances are defined as the IP divided by its corresponding
³⁸⁴ uncertainty, $s(d_0) = d_0/\sigma(d_0)$ and $s(z_0) = z_0/\sigma(z_0)$. When used in flavour tagging
³⁸⁵ (see Chapter 4), track IP significances are lifetime signed according to the track's
³⁸⁶ direction with respect to the jet axis and the primary vertex [37]. The sign IP
³⁸⁷ significances is positive if the track crosses the jet axis in front of the primary vertex
³⁸⁸ and negative if the crossing is behind the primary vertex.

³⁸⁹ 3.2.3 Hadron Collider Definitions

³⁹⁰ Cross Section

³⁹¹ The cross section σ is closely related to the probability of an interaction between
³⁹² two colliding particles, and is analogous to an effective cross-sectional area of the
³⁹³ particles. The cross section of a process depends on the transition matrix element,
³⁹⁴ obtained using the Feynman rules of the theory which are derived using QFT, and a
³⁹⁵ phase space integral. At hadron colliders such as the LHC, the proton-proton cross

¹Reconstructed charged particles are assumed to have a charge of ± 1 .

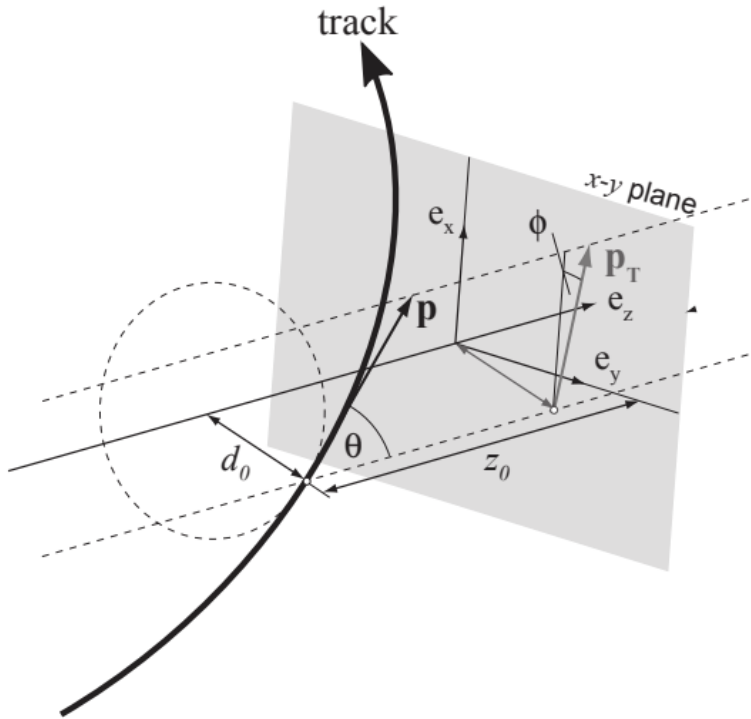


Figure 3.3: The track parameterisation used at the ATLAS detector. Five coordinates ($d_0, z_0, \phi, \theta, q/p$) are specified, defined at the track's point of closest approach to the nominal interaction point at the origin of the coordinate system. The figure shows the three-momentum \mathbf{p} and the transverse momentum p_T (defined in Eq. (3.2)). The basis vectors e_x, e_y and e_z are also shown. Reproduced from Ref. [36].

³⁹⁶ section can be factorised as

$$\sigma(pp \rightarrow X) \approx \text{PDFs} \cdot \text{partonic cross section.} \quad (3.4)$$

³⁹⁷ The partonic cross section can be calculated at sufficiently high energies such as
³⁹⁸ those found at the LHC, while the parton distribution functions (PDFs) have to be
³⁹⁹ extracted from experimental results.

⁴⁰⁰ Luminosity

⁴⁰¹ The total number of proton-proton collisions N is related to the total pp cross σ
⁴⁰² section by the integrated luminosity L , as in

$$N = \sigma L = \sigma \int \mathcal{L} dt. \quad (3.5)$$

⁴⁰³ The instantaneous luminosity \mathcal{L} relates the cross section to the number of collisions
⁴⁰⁴ per unit time. For two colliding bunched proton beams, it is defined as

$$\mathcal{L} = \frac{1}{\sigma} \frac{dN}{dt} = \frac{fn_1 n_2}{4\pi\sigma_x\sigma_y}, \quad (3.6)$$

⁴⁰⁵ where n_1 and n_2 are the number of protons in the colliding bunches, f is the bunch
⁴⁰⁶ crossing frequency, and σ_x and σ_y are the rms width of the beam in the horizontal
⁴⁰⁷ and vertical directions.

⁴⁰⁸ The total luminosity recorded over the course of Run 2 is shown in Fig. 3.4. In
⁴⁰⁹ total, 139 fb^{-1} of usable physics data was collected over the three-year run. The
⁴¹⁰ uncertainty on the total integrated luminosity is 1.7% [38].

⁴¹¹ Pile-up

⁴¹² At the centre of the ATLAS detector, bunches of more than 10^{11} protons meet at a
⁴¹³ small crossing angle. Each bunch-crossing is called an *event*. There is generally at
⁴¹⁴ most one hard proton-proton scatter per event. Additional interactions are typically
⁴¹⁵ relatively soft and are known as *pile-up*. Pile-up from interactions within the same
⁴¹⁶ bunch-crossing is known as *in-time* pile-up while residual signatures from previous
⁴¹⁷ bunch-crossings is known as *out-of-time* pile-up. The number of pile-up interactions

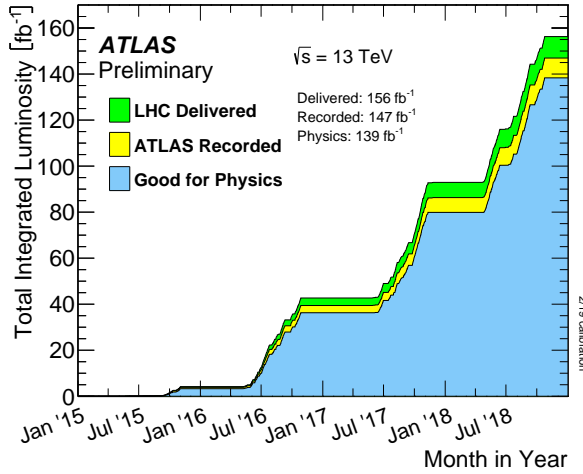


Figure 3.4: Delivered, recorded, and usable integrated luminosity as a function of time over the course of Run 2 [33]. A total of 139 fb^{-1} of collision data is labelled as good for physics, meaning all sub-detector systems were operating nominally.

is denoted μ , which is often given as a time-averaged value $\langle \mu \rangle$. Histograms showing the number of pile-up interactions over the course of Run 2 are shown in Fig. 3.5.

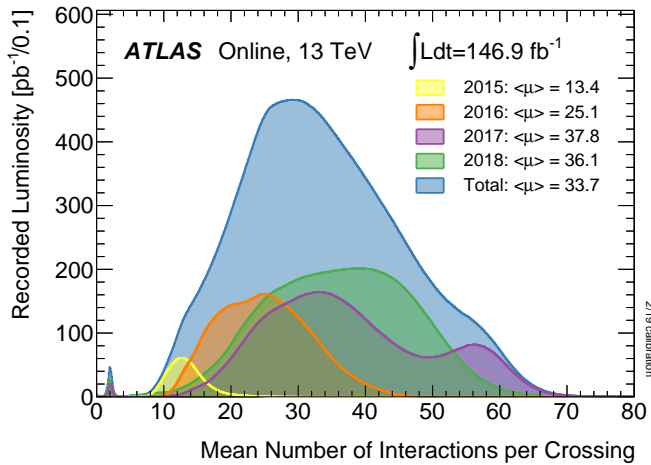


Figure 3.5: Average pile-up profiles measured by ATLAS during Run 2 [33]. Higher levels of pile-up are planned for Run 3.

420 3.3 The ATLAS Detector

421 The ATLAS² detector is made up of several specialised sub-detectors which are
422 arranged concentrically around the nominal interaction point at the centre of the
423 detector. The detector is designed to cover nearly the entire solid angle around the
424 collision point. In this section a condensed overview of each sub-detector is given, in
425 order of increasing radial distance from the point of collision. The inner tracking
426 detector is described in Section 3.3.1, the electromagnetic and hadronic calorimeters
427 in Section 3.3.2, the muon spectrometer in Section 3.3.3, and finally the trigger is
428 described in Section 3.3.4. More complete information on the detector can be found
429 in Ref. [31], while an overview of physics performance is given in [39].

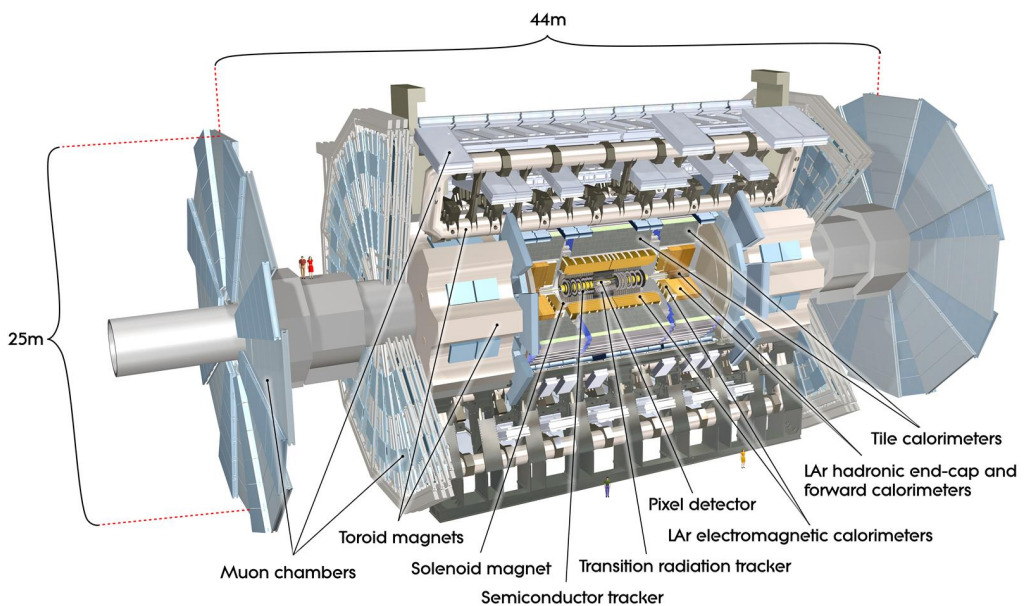


Figure 3.6: A 3D model of the entire ATLAS detector [40]. The detector is 46 m long and 25 m in diameter. Cutouts to the centre of the detector reveal the different subdetectors which are arranged in concentric layers around the nominal interaction point.

²A Toroidal LHC ApparatuS.

430 3.3.1 Inner Detector

431 The inner-detector system (ID) provides high-resolution charged particle trajectory
432 tracking in the range $|\eta| < 2.5$. The ID is immersed in a 2 T axial magnetic field,
433 produced by a superconducting solenoidal magnet, which enables the measurement
434 of particle momentum and charge. After Run 3, the ID will be replaced by the
435 ITk [41, 42].

436 The inner detector is made up of several sub-systems, shown in Figs. 3.7 and 3.8. The
437 high-granularity silicon pixel detector covers the vertex region and typically provides
438 four spacepoint measurements per track. It is followed by the silicon microstrip
439 tracker (SCT), which usually provides a further four spacepoint measurements per
440 track. These silicon detectors are complemented by the Transition Radiation Tracker
441 (TRT), which enables radially extended track reconstruction up to $|\eta| = 2.0$.

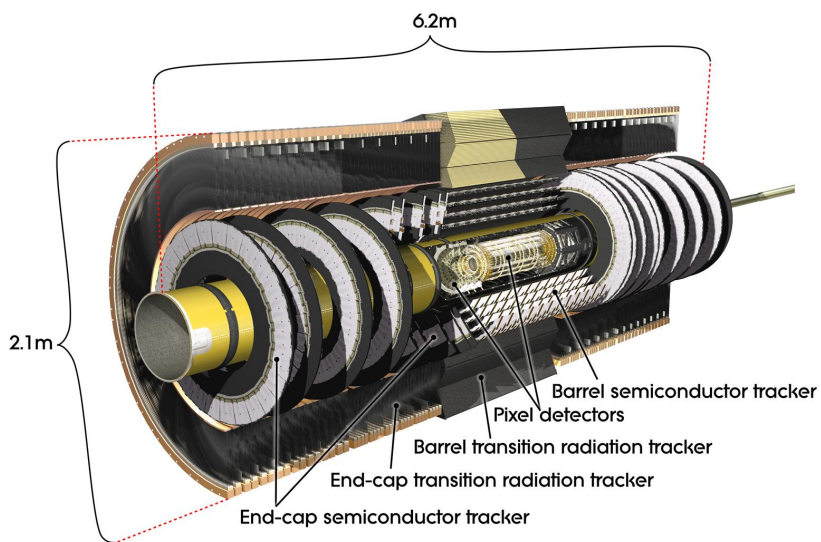


Figure 3.7: A 3D model of the ATLAS ID, made up of the pixel and SCT subdetectors, showing the barrel layers and end-cap disks [43].

442 The target inverse momentum resolution for the combined ID measurement is
443 parameterised as a function of the track transverse momentum and polar angle [39].
444 The parameterisation is given by

$$\sigma(1/p_T) = 0.36 \oplus \frac{13}{p_T \sin \theta} \text{TeV}^{-1}, \quad (3.7)$$

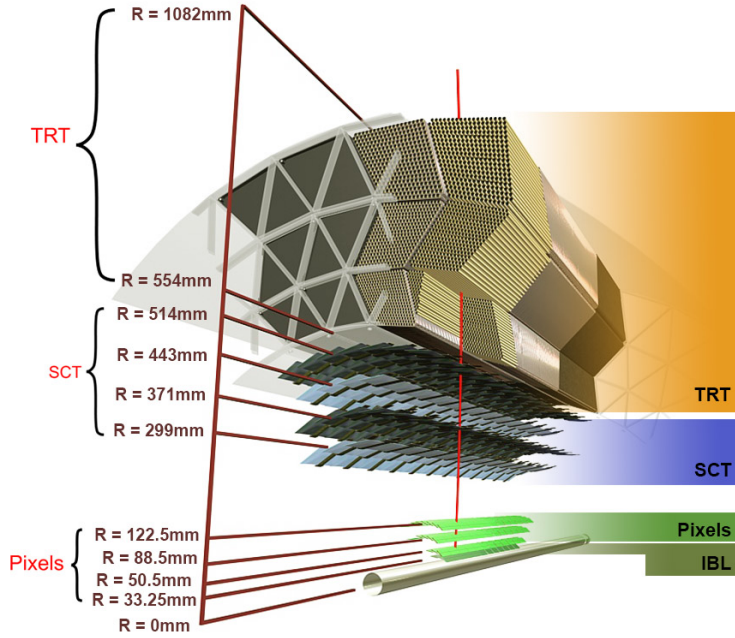


Figure 3.8: A cross-sectional view of the ATLAS ID, with the radii of the different barrel layers shown [36].

445 where \oplus denotes a sum in quadrature. For high- p_T tracks (e.g. $p_T \approx 100$ GeV) in
 446 the central region, $\sigma(1/p_T) \approx 0.4$ TeV $^{-1}$ corresponding to a relative error of 4%. The
 447 momentum resolution generally good enough to correctly identify the sign of the
 448 charge on particles up to the highest energies expected at the LHC. The transverse
 449 impact parameter resolution $\sigma(d_0)$ is parameterised similarly as

$$\sigma(d_0) = 11 \oplus \frac{115}{p_T \sin \theta} \mu\text{m}. \quad (3.8)$$

450 Pixel Detector

451 The silicon pixel detector is comprised of four cylindrical barrels at increasing radii
 452 from the beamline, and four disks on each side. The innermost barrel layer is
 453 the insertable B-layer (IBL), which was installed before Run 2 [44, 45] and lies
 454 approximately just 33 mm from the beam axis. The second-to-innermost layer is
 455 often referred to as the B-layer. The specification of the pixel detector determines the
 456 impact parameter resolution and the ability to reconstruct primary and secondary

vertices. The detector is required to have a high granularity (i.e. resolution) to maintain the low occupancy required to resolve nearby particles. Individual pixels are 50 μm in the transverse direction $R\phi$ and 400 μm in the longitudinal z direction (250 μm for the IBL). Cluster positions have a resolution of approximately 10 μm in $R\phi$ and 100 μm in z .

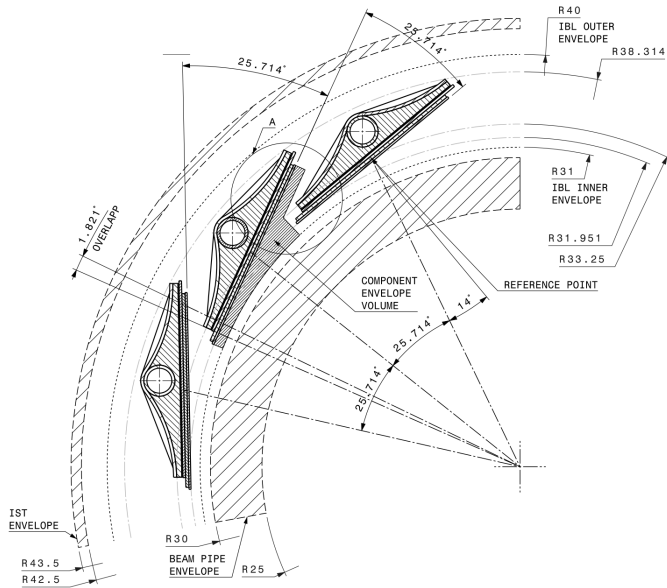


Figure 3.9: A schematic cross-sectional view of the ATLAS IBL [44].

462 Semi-Conductor Tracker (SCT)

463 The SCT is made up of four concentric barrel layers in the central region, and nine
 464 disks in each end-cap. Each layer is itself made of a pair of silicon microstrip layers,
 465 with a small stereo angle (20 mrad) between the two layers enabling the z -coordinate
 466 to be measured from a pair of strip measurements. The SCT typically provides four
 467 precision spacepoint measurements (eight strip measurements) per track in the barrel
 468 region. These have intrinsic uncertainties of 17 μm in the transverse direction $R\phi$, and
 469 580 μm in the longitudinal direction z [46]. The measurements provide a contribution
 470 to the measurement of charged particle momentum and impact parameter, along
 471 with vertex position. Charge-particle tracks can be distinguished if separated by
 472 more than $\sim 200 \mu\text{m}$.

473 Transition Radiation Tracker (TRT)

474 The TRT is a straw-tube tracker which complements the higher-resolution silicon-
475 based tracks by offering a larger number of hits per track (typically around 30) and
476 a long lever arm, which aids the accurate measurement of particle momentum. It is
477 made up of approximately 300 000 drift tubes with a diameter of 4 mm which are filled
478 with an argon/xenon gas mixture. The walls of each tube are electrically charged,
479 and a thin conducting wire runs along the center. When a charged particle traverses
480 a tube, it ionises the gas and the resulting liberated electrons drift along the electric
481 field to the wire, where an associated charge is registered. In the barrel the straws
482 run parallel to the z -axis and therefore the TRT only provides tracking information
483 in $R\phi$. Straws are arranged radially in the end-caps. The resulting two-dimensional
484 spacepoints have a resolution of approximately 120 μm . The spaces between the
485 straws are filled with a polymer which encourages the emission of transition radiation,
486 aiding electron identification.

487 3.3.2 Calorimeters

488 The calorimeter system measures the energy of incident particles over the range
489 $|\eta| < 4.9$. There are two main sub-systems: the electromagnetic calorimeter (ECal),
490 which focuses on the measurement of electrons and photons, and the hadronic
491 calorimeter (HCal), which measures the energy of hadrons. Upon entering the
492 calorimeter, incident particles will interact with the detector material to produce a
493 shower of secondary particles with reduced energies. The charge deposited in this
494 process is measured to reconstruct the energy of the initial incident particle. The
495 two calorimeter sub-systems must provide strong containment of showering particles
496 to prevent punch-through of EM and non-muon particles to the HCal and muon
497 system respectively.

498 Liquid Argon (LAr) Electromagnetic Calorimeter

499 The more granular lead/liquid-argon ECal covers the region $|\eta| < 3.2$ and is split
500 into barrel (covering $|\eta| < 1.475$) and end-cap (covering $1.375 < |\eta| < 3.2$) regions.
501 EM calorimetry works by encouraging electrons and photons to interact with electri-

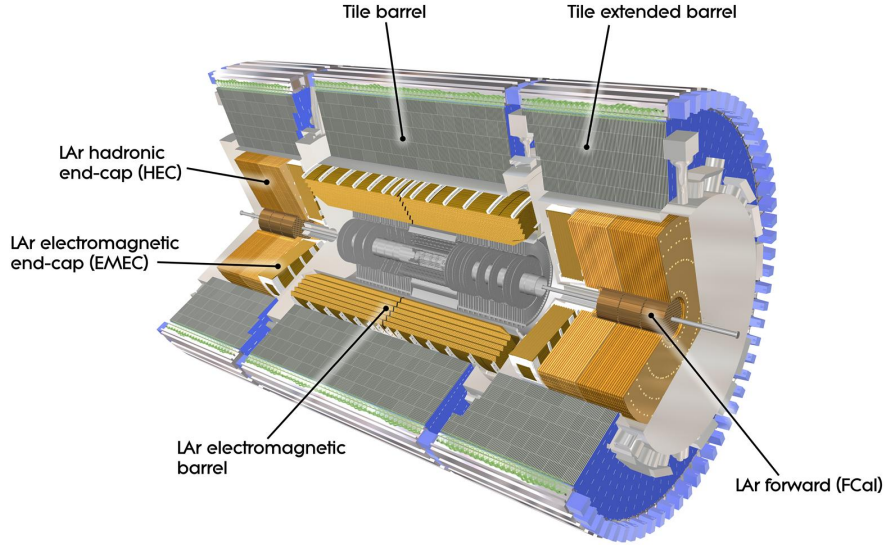


Figure 3.10: The ATLAS calorimeters [47]. The ECal uses LAr-based detectors, while the HCal uses mainly scintillating tile detectors. In the forward region the HCal also includes the LAr hadronic endcaps.

502 cally charged particles in detector material via bremsstrahlung ($e \rightarrow e\gamma$) and pair
 503 production ($\gamma \rightarrow e^+e^-$). The EM calorimeter uses lead absorber plates to initiate
 504 EM showers, resulting in secondary particles which ionise the surrounding liquid
 505 argon. The charge is collected on copper electrodes and read out. The accordion
 506 geometry of the ECal allows for a full coverage in ϕ without any azimuthal cracks.

507 The energy resolution of the LAr calorimeter is made up of a sampling and a constant
 508 term, which are summed in quadrature to produce the overall energy resolution. The
 509 sampling term contributes approximately $10\%/\sqrt{E}$, while the constant term adds an
 510 additional 0.7%. Photons with moderate transverse energy $E_T \approx 50 \text{ GeV}$ have an
 511 overall energy resolution of at most 1.6% over most of the pseudorapidity range. At
 512 lower $E_T \approx 10 \text{ GeV}$, the resolution is degraded to approximately 5%. The resolution
 513 measurements are obtained from test beam data [39].

514 **Hadronic Tile Calorimeter**

515 In the central barrel region with $|\eta| < 1.7$, the HCal uses a tile calorimeter with
 516 steel as an absorbing material, and scintillating tiles as the active material. Two

517 copper/liquid-argon calorimeter end-caps are also used. Incident hadrons interact
518 via the strong and electromagnetic forces with the absorber material, mainly loosing
519 energy due to multiple inelastic nuclear collisions. The active material captures the
520 resulting electrons and photons to measure the energy of the incident hadron.

521 The jet energy resolution of the HCal is parameterised as a function of the jet
522 transverse energy

$$\sigma(E_T)/E_T = 50\% \sqrt{E_T} \oplus 3\%, \quad (3.9)$$

523 corresponding to a jet energy resolution of 10% at a jet p_T of approximately 100 GeV
524 [48].

525 3.3.3 Muon Spectrometer

526 Due to their higher mass, muons easily pass unimpeded through the ID and calorime-
527 ters and therefore require specialised detectors for their measurement. The Muon
528 Spectrometer (MS) is made up of dedicated tracking and triggering hardware. The
529 precision tracking system uses three layers of monitored drift tubes with a barrel
530 region covering $|\eta| < 1.2$ and end-caps covering $1 < |\eta| < 2.7$. The inner layers of
531 the end-caps use cathode strip chambers to better cope with the high occupancy
532 in the forward region. Precision tracking resolution is approximately 50 μm . The
533 trigger system is comprised of resistive plate chambers in the barrel region covering
534 $|\eta| < 1.0$ and thin gap chambers in the end-cap regions covering $1 < |\eta| < 2.4$. A set
535 of three superconducting air-core toroidal magnets, each made up of eight coils, is
536 used in each of the barrel and end-caps to deflect the muons as they pass through
537 the MS, allowing their momentum and charge to be measured from the direction
538 and magnitude of curvature. The toroidal magnets generate a field which is largely
539 orthogonal to the muon trajectories which allows for maximum deflection. The
540 transverse momentum resolution has been measured to be approximately 1.7% in the
541 central region for low- p_T muons, increasing to 4% for high- p_T muons in the forward
542 regions [49].

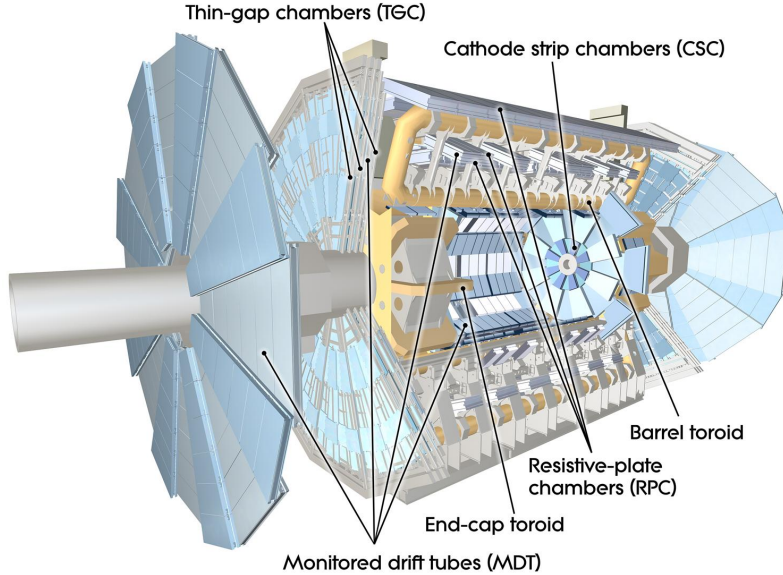


Figure 3.11: The ATLAS muon spectrometer [50].

543 3.3.4 The Trigger

544 The 25 ns bunch spacing used over the course of Run 2 corresponds to a bunch-
 545 crossing or event rate of 40 MHz (see Table 3.1). If the full information for the
 546 detector was written out for each event, this would correspond to the generation
 547 of 60 TB of data each second. This is more than can be feasibly read out from
 548 the hardware, processed and stored, requiring the use of a trigger system which
 549 quickly makes a decision about whether or not an event is potentially interesting
 550 and should be kept for further analysis. The trigger system is comprised of two
 551 levels which search for signs of electrons, muons, taus, photons, and jets, as well as
 552 events with large total or missing transverse energy. The hardware-based Level-1
 553 (L1) trigger uses coarse information from the calorimeters and MS to accept events at
 554 an average rate of 100 kHz approximately 2.5 μ s after the event. After the L1 trigger,
 555 the software-based High Level Trigger (HLT) makes use of 40 000 CPU cores to make
 556 a final selection on surviving events in approximately a few hundred milliseconds.
 557 The final event read-out rate is approximately 1.2 kHz, corresponding to 1.2 GB s^{-1}
 558 of permanent data storage. More information is provided in [51].

559 3.4 Reconstructed Physics Objects

560 Event reconstruction is the process of analysing the output from the detector to
561 determine the type and properties of particles present in an event. The reconstructed
562 event provides information about the underlying physics process that led to these
563 observable final state particles. Events passing the trigger selection (described in
564 Section 3.3.4) undergo offline reconstruction, which makes use of the full information
565 from the detector. Reconstruction and analysis of events relies on the extensive
566 ATLAS software stack, see Ref. [52] for more information.

567 Several different reconstructed objects are used for physics analyses. Objects relevant
568 to this thesis are described below.

569 3.4.1 Tracks

570 The reconstructed trajectories of charged particles are referred to as *tracks*. Track are
571 reconstructed from the energy depositions (called *hits*) left by the particles as they
572 traverse the the inner detector. Tracks are widely used for a variety of downstream
573 applications, including vertexing and jet tagging, so their accurate reconstruction
574 is a critical task. A comprehensive introduction to ATLAS tracking is available
575 in Ref. [53], while specific optimisations for dense environments are detailed in
576 Refs. [54, 55]. An overview of track reconstruction is given below.

577 Space-point Formation (Clustering)

578 When a charged particle traverses a silicon layer, charge can be collected in more
579 than one pixel or strip. This is due to the incident angle of the particles with respect
580 to the sensor, and also the drift of electrons between sensors caused by the magnetic
581 field. Clusters (also called *hits* or *space-points*) are formed by clustering neighbouring
582 pixels or strips and estimating locations of space-points using the shape and energy
583 distribution of the clusters.

584 Track Finding

585 Space-points are used to build track seeds. These are groups of three hits which
586 are geometrically compatible with being part of a track segment. A combinatorial
587 Kalman filter (KF) is used to build track candidates by extending track seeds. The
588 filter can create multiple track candidates per seed, with bifurcations along the track
589 occurring when more than one compatible space-point exists on a given layer. In
590 this way, the KF creates an excess of *track candidates*, which are only required to
591 satisfy basic quality requirements. Track candidates are allowed to reuse or *share*
592 hits freely (a single hit may be used by multiple track candidates). Typically, the
593 presence of shared hits is a predictor of a bad track due to the high granularity of
594 the ATLAS tracking detectors. At this stage, there can also be a large number of
595 incorrect hits assigned to otherwise good tracks, and additionally large number of
596 *fake* tracks, which are comprised of a majority of wrong hits and do not correspond
597 to the trajectory of any one physical particle (fake tracks are defined as those where
598 the majority of associated hits do not originate from one single truth particle, see
599 Eq. (5.5)). The low quality of tracks at this stage necessitates an ambiguity solving
600 step, in which candidates are cleaned, and the highest quality track are selected.

601 Ambiguity Solving

602 Ambiguity solving was introduced as part of the ATLAS New Tracking effort [53],
603 which was intended to improve track reconstruction performance in dense envi-
604 ronments. In the ambiguity solver, track candidates are processed individually in
605 descending order of a track score. The track score quantifies the likelihood of the
606 track corresponding to the trajectory of a real particle. Scoring uses a number of
607 variables, including the number and positions of hits (preferring hits in more precise
608 regions of the detector), the transverse momentum of the track and the track fit
609 quality. The track fit quality describes the quality of the track as the χ^2 divided
610 by the number degrees of freedom on the track. A preference for high transverse
611 momentum tracks promotes the successful reconstruction of the more physically
612 interesting energetic particles, and suppresses the large number of wrong hits assigned
613 to low momentum tracks. The ambiguity solver also penalises tracks with missing
614 hits on the innermost detector layers.

615 During the processing of a given highest-scoring track candidate, the track is cleaned
616 (whereby problematic hits are removed), and, if the resulting track satisfies the quality
617 selection criteria, a high precision fit of the track parameters using the surviving hits
618 is performed. The high precision fit makes full use of all available information, and
619 uses an updated position and uncertainty estimate for each cluster obtained from
620 a Neural Network (NN) [56]. If the track has reached this stage without rejection
621 by passing various quality regiments, it is re-scored and returned to the list of track
622 candidates. If the same track is then processed again without requiring modification,
623 it is added to the final track collection. Track candidates that fall below a certain
624 quality cut are rejected. This selection does allow for the possibility of a track having
625 small number of shared hits.

list shared
hit cut?

626 Neural Network Cluster Splitting

627 As part of track cleaning, shared hits are classified by a NN to determine if they are
628 compatible with the characteristic features of a merged cluster [54, 56]. A merged
629 cluster is one made up of a combination of energy deposits from more than one
630 particle, which have become merged due to the closeness of the associated particles
631 and the limited resolution of the detector. While in general this event is rare, it
632 is common for clusters to become merged in dense environments, as discussed in
633 Section 4.1. If the cluster is predicted to be merged it is labelled as being freely
634 shareable, or *split*. Hits not compatible with the merged hypothesis can still be
635 shared by a limited number of tracks, but come with a penalty for the track which
636 may hinder its acceptance into the final track collection.

637 3.4.2 Vertices

638 Groups of reconstructed tracks can be examined to determine whether the particles
639 originated from a common spatial point of origin. This occurs when proton-proton
640 collisions take place (primary vertices), when a particle decays or radiates, and also
641 as a result of interaction with the detector material (secondary vertices). Vertex
642 reconstruction is made up of two stages. First, vertex finding takes place, which
643 is the process of grouping tracks into compatible vertices. Second, vertex fitting

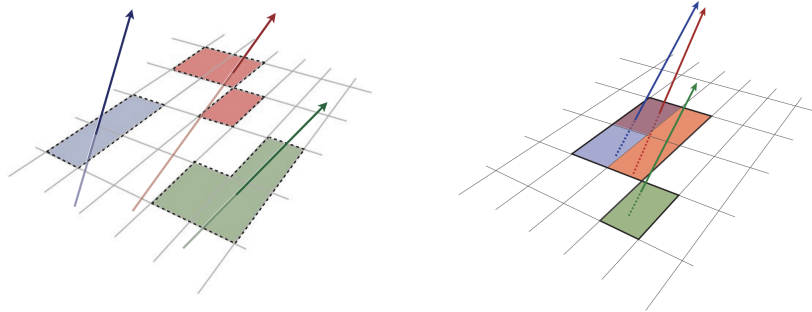


Figure 3.12: Particles (left) which have enough separation will leave charge depositions which are resolved into separate clusters. Sufficiently close particles (right) can lead to merged clusters. Their combined energy deposits are reconstructed as a single merged cluster [55].

644 combines information from compatible tracks to reconstruct the physical properties
645 of the vertex, such as mass and position.

646 Primary Vertices

647 Each proton-proton interaction happens at a *primary vertex* (PV). Primary vertices
648 are iteratively reconstructed with tracks using the iterative vertex finder (IVF) [57].
649 In Run 3, the IVF will be replaced with an adaptive multi-vertex finder (AMVF) [58].
650 The *hard scatter vertex* of an event is chosen as the primary vertex whose associated
651 tracks have the largest sum of transverse momentum squared, $\Sigma(p_T^2)$.

652 Secondary Vertices

653 Secondary vertices (SV) occur when a particle radiates or decays at a sufficient
654 distance from the primary vertex to be resolved from the primary vertex (see
655 Section 4.1.1). Two widely used secondary vertexing tools are used within ATLAS:
656 SV1 and JetFitter [59]. Each attempts to reconstruct secondary vertices inside a jet
657 using the tracks associated to that jet (see Section 3.4.3 for more information about
658 track association). SV1 by design attempts to reconstruct only a single inclusive
659 vertex per jet. This inclusive vertex groups all b -hadron decay products, including
660 tracks from the b -hadron decay itself and tracks from $b \rightarrow c$ decays. The second tool,
661 JetFitter attempts to resolve each displaced vertex inside the jet, such that secondary

662 vertices from b -hadron decays are reconstructed separately to tertiary vertices from
663 $b \rightarrow c$ decay chains.

664 **3.4.3 Jets**

665 Jets are an aggregate reconstructed object corresponding to a collection of collimated
666 stable particles which results from a decay chain of an quark or gluon progenitor. Jets
667 are built by clustering constituent objects (e.g. tracks or calorimeter clusters) using
668 a jet finding algorithm, for example the anti- k_t algorithm [60], which is implemented
669 in FASTJET [61].

670 **EMTopo Jets**

671 EMTopo jets are reconstructed from noise-suppressed topological clusters (topoclus-
672 ters) of calorimeter energy depositions. The clustering uses the energy significance
673 of each cell, defined as

$$S_{\text{cell}} = \frac{E_{\text{cell}}}{\sigma_{\text{noise, cell}}}, \quad (3.10)$$

674 where E_{cell} is the energy measured in a given calorimeter cell, and $\sigma_{\text{noise, cell}}$ is the
675 expected level of noise on the cell (e.g. from pile-up interactions). Topoclusters are
676 formed from a seed cell with a large S_{cell} , and expanded by iteratively adding neigh-
677 bouring cells with a sufficiently large energy significance. Collections of topoclusters
678 are then clustered into a jet using the anti- k_t algorithm with a radius parameter of
679 0.4 (small- R jets) or 1.0 (large- R jets). More information is available in Ref. [62].

680 **Particle Flow Jets**

681 Particle-flow (PFlow) jets are reconstructed from particle-flow objects [63] using
682 the anti- k_t algorithm with a radius parameter of 0.4. Particle-flow objects integrate
683 information from both the ID and the calorimeters, improving the energy resolution
684 at high transverse momenta and reducing pile-up contamination. The PFlow jet
685 energy scale is calibrated according to Ref. [64].

686 Tracks are associated to jets using a ΔR association cone, the width of which
687 decreases as a function of jet p_T , with a maximum cone size of $\Delta R \approx 0.45$ for jets
688 with $p_T = 20\text{ GeV}$ and minimum cone size of $\Delta R \approx 0.25$ for jets with $p_T > 200\text{ GeV}$.
689 If a track is within the association cones of more than one jet, it is assigned to the
690 jet which has a smaller $\Delta R(\text{track}, \text{jet})$.

691 Jet flavour labels are assigned according to the presence of a truth hadron within
692 $\Delta R(\text{hadron}, \text{jet}) < 0.3$ of the jet axis. If a b -hadron is found the jet is labelled a b -jet.
693 In the absence of a b -hadron, if a c -hadron is found the jet is called a c -jet. If no b -
694 or c -hadrons are found, but a τ is found in the jet, it is labelled as a τ -jet, else it is
695 labelled as a light-jet.

696 PFlow jets are used to train the algorithms discussed in Chapter 5 and Chapter 6.

697 Large- R Jets

698 Large- R jets have a radius parameter $R = 1.0$ and are built by clustering topological
699 calorimeter clusters using the anti- k_t algorithm [65]. The large radius parameter
700 is especially useful for containing the decay products of a boosted Higgs boson, as
701 discussed in Chapter 7. Due to their large size, large- R jets benefit from a grooming
702 procedure called trimming which remove soft contaminants inside the jet [66, 67].
703 Trimming aims to remove jet constituents from pile-up and the underlying event,
704 which helps to improve the jet mass resolution and its robustness to varying levels
705 of pile-up. The jet mass is computed using a combination of information from the
706 calorimeters and ID, and a calibration to data is applied [68].

707 Track-jets

708 Track-jets are built by clustering tracks using the anti- k_t clustering algorithm and
709 are used in the analysis described in Chapter 7. The radius parameter is allowed
710 to vary with transverse momentum such that a broader cone (up to $R = 0.4$) is
711 used for low- p_T track-jets and a narrower cone (down to $R = 0.02$) for high- p_T
712 track-jets [69, 70]. The narrower cone is better suited to clustering highly collimated
713 jet constituents at high- p_T . Truth flavour labels for track-jets are derived using the
714 same $\Delta R(\text{hadron}, \text{jet}) < 0.3$ matching scheme as used for PFlow jets.

715 3.4.4 Leptons

716 Electrons and muons leave characteristic signatures that are picked up in the ECal
 717 and MS respectively. The reconstruction of both types of stable lepton is briefly
 718 outlined below.

719 Electrons

720 Electrons candidates are reconstructed by matching PV-compatible³ inner detector
 721 tracks to topological calorimeter clusters. The track-cluster matching criteria takes
 722 into account the significant energy loss of the electron due to bremsstrahlung. If a
 723 match is found, a refit of the track is performed using the Gaussian Sum Filter (GSF)
 724 [71], which better handles trajectory reconstruction in the presence of bremsstrahlung.
 725 Various identification criteria are then applied to the candidates using a likelihood-
 726 based (LH) method to improve purity. These include requirements on the track
 727 quality and cluster matching, the shape of electromagnetic shower in the ECal,
 728 leakage into the HCal, and the amount of transition radiation detected in the TRT.
 729 Isolation criteria with respect to other nearby ID tracks and calorimeter clusters may
 also be applied. A full description can be obtained from Ref. [72].

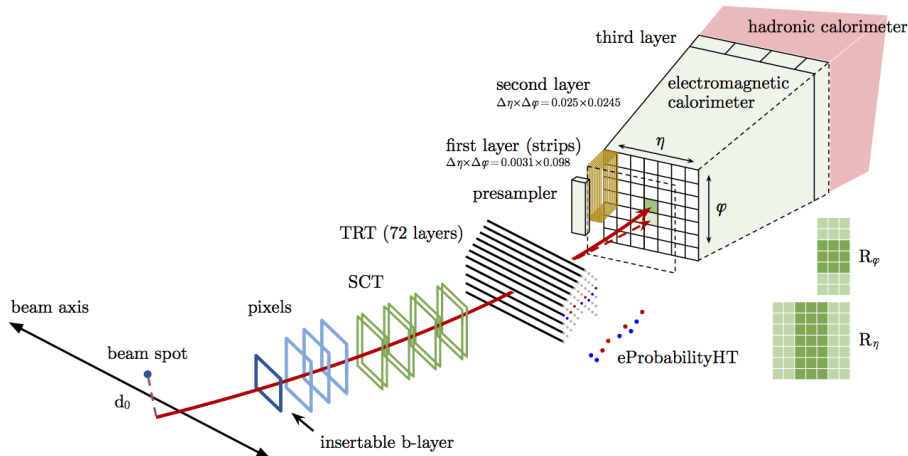


Figure 3.13: A sketch of electron reconstruction using the ATLAS detector [72]. Electron reconstruction makes use of the entire ID and the calorimeters. In particular, discriminating information comes from the TRT and ECal.

730

³The ID track associated with the electron is required to satisfy $d_0/s(d_0) < 5$ and $z_0 \sin \theta < 0.5$ mm.

731 **Muons**

732 Muon reconstruction makes use of the dedicated MS (see Section 3.3.3), the tracks
733 from the ID, and the presence of characteristic signatures in the calorimeters. Muon
734 tracks (i.e. a track reconstructed in the MS) are reconstructed by connecting straight-
735 line track segments, which are identified via a Hough transform, and combined into
736 a approximately parabolic trajectory. Finally, a global χ^2 fit is performed, taking
737 into account possible interactions between the muon and the detector material. A
738 reconstructed muon is called *combined* if it completes successful matching to an
739 ID track. Combined muons undergo a further fit with the combined ID and MS
740 hits, with the energy loss due to the traversal of the calorimeters being taking into
741 account.

742 After reconstruction, candidate muons further undergo an identification processes
743 which helps to efficiently identify prompt muons whilst rejecting background sig-
744 nals (e.g. non-prompt muons from pion and kaon decays, the punch-through of a
745 hadron from the calorimeter, or the semi-leptonic decay of a heavy flavour hadron).
746 Combined muon identification takes into account discrepancies in the p_T and charge
747 measurements in the MS and ID, and the χ^2 of the combined track fit. Selections
748 on the number of hits in the ID and MS are also applied. At the medium identifi-
749 cation working point, approximately 96% of muons with $20 \text{ GeV} < p_T < 100 \text{ GeV}$
750 are successfully identified. On top of the identification requirements, a number of
751 isolation requirements can also be applied to further suppress background signals. In
752 the region $|\eta| < 2.2$, the momentum resolution of reconstructed muons is 1.7%.

753 More information on muon reconstruction, identification and isolation can be found
754 in Ref. [73].

755 **3.4.5 Missing Transverse Momentum**

756 An imbalance in the final state transverse momentum can occur as a result of
757 incomplete measurement of the final state particles. In particular, neutrinos are
758 not measured by the detector and contribute to the missing transverse momentum
759 E_T^{miss} . Incomplete detector acceptance and inaccuracies in the reconstruction of the
760 final state can also contribute to the missing transverse momentum of an event. In
761 order to calculate the missing transverse momentum, the negative vector sum of

- 762 the momentum of all photons, leptons and small- R jets with $p_T > 20\text{ GeV}$ is taken.
763 The momenta of tracks associated to the primary vertex are also taken into account.
764 The magnitude of $\mathbf{E}_T^{\text{miss}}$ is written E_T^{miss} . More information about missing transverse
765 momentum reconstruction is provided in [74].

766 Chapter 4

767 Tracking and b -tagging

768 Many ATLAS analyses rely on b -tagging, which is the selection of instantiated by
769 b -quarks (b -jets) and rejecting jets created from other quarks (c and light flavours u ,
770 d , s). These b -tagging algorithms (also called *taggers*) work by discriminating for the
771 unique signatures of b -jets, which are outlined in Section 4.1. The various b -tagging
772 algorithms ultimately take as their input information about the reconstructed jet
773 and its associated tracks. Successful b -tagging relies therefore on the efficient and
774 accurate reconstruction of tracks, and especially those tracks corresponding to the
775 products of b -hadron decays.

776 Historically a two tiered approach to b -tagging has been taken, in which so called
777 *low-level* taggers take as inputs information about the jet and associated tracks, and
778 attempt to reconstruct or identify some aspect of a b -jet, such as displaced tracks
779 or secondary vertices. The outputs of several low-level taggers are then fed into a
780 *high-level* tagger, which uses a multivariate approach to discriminate between jet
781 flavours.

782 As the different b -tagging algorithms ultimately rely on tracks accurate and efficient
783 track reconstruction is essential. This chapter summarises the challenges facing
784 tracking and b -tagging at high transverse momentum with an investigation into track
785 reconstruction performance in Section 4.1. Some preliminary investigations into
786 improving tracking in this regime are investigated in Section 4.2.

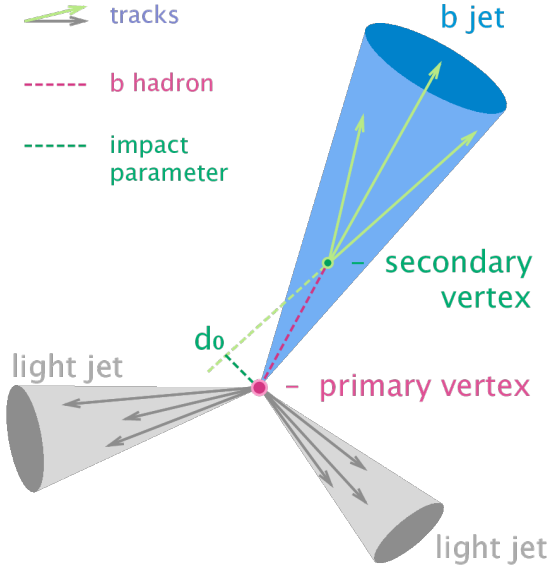


Figure 4.1: Diagram of a typical b -jet (blue) which has been produced in an event alongside two light jets (grey) [75]. The b -hadron has travelled a significant distance (pink dashed line) from the primary interaction point (pink dot) before its decay. The large transverse impact parameter d_0 is a characteristic property of the trajectories of b -hadron decay products.

787 4.1 b -hadron Reconstruction

788 This section outlines the typical detector signature of a b -hadron in Section 4.1.1
 789 and discusses some associated reconstruction difficulties in Section 4.1.2.

790 4.1.1 Decay Topology

791 b -hadrons are quasi-stable bound states of a bottom quark and one or more lighter
 792 quarks. Collectively, these are the b -mesons (e.g. $B^+ = u\bar{b}$, $B^0 = d\bar{b}$) and baryons
 793 with (e.g. $\Lambda_b^0 = udb$). After a b -quark is produced as the result of some proton-proton
 794 collision, they quickly hadronise. The hadronisation process is hard – around 70-80%
 795 of the b -quark’s momentum is passed to the b -hadron, with the rest being radiated
 796 as prompt hadronisation or fragmentation particles. See Ref. [76] for a more in
 797 depth discussion on hadronisation and the closely related process of fragmentation.
 798 Henceforth the combined hadronisation and fragmentation products will be referred
 799 to collectively as fragmentation.

800 *b*-hadrons are interesting objects of study due to their relatively long proper lifetimes
 801 $\tau \approx 1.5$ ps [77]. This lifetime corresponds to a proper decay length $c\tau \approx 450$ μm .
 802 Experiment has shown that *b*-hadrons do not couple strongly to light-flavour quarks
 803 [78]. The lifetime of *b*-hadrons is therefore approximately determined only by a single
 804 CKM matrix element V_{cb} (see Section 2.1.3). In the rest frame of the detector, the
 805 typical *b*-hadron travels a distance

$$d = \gamma\beta c\tau \approx \gamma c\tau \quad (4.1)$$

806 before decaying, where in the high energy limit $\gamma = E_b/m_b$ and $\beta = v/c = 1$. For
 807 a 1 TeV *b*-hadron, this gives $d \approx 90$ mm – well beyond the radius of the first pixel
 808 layer (the IBL) at a radius of 33 mm (see Fig. 4.2). This significant displacement is
 809 characteristic of *b*-jets and makes it possible to reconstruct secondary vertices at the
 810 *b*-hadron decay point.

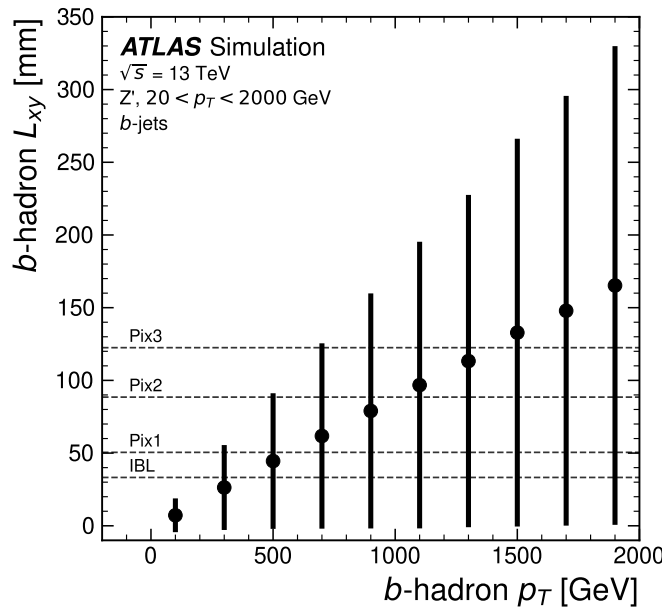


Figure 4.2: The truth *b*-hadron decay radius L_{xy} as a function of truth transverse momentum p_T for reconstructed *b*-jets in Z' events. Error bars show the standard deviation. The pixel layers are shown in dashed horizontal lines.

811 *b*-hadrons decay weakly to on average four or five collimated stable particles. These
 812 particles, along with any fragmentation particles, are reconstructed in the detector as
 813 a jet. A *b*-jet has several characteristic features which differentiate it from light-jets.

814 These features stem from the significant displacement of the b -hadron that can
 815 occur, in particular for high transverse momentum b -jets. The primary feature is
 816 the presence of a high mass secondary vertex that is significantly displaced from the
 817 primary vertex. Reconstruction of these vertices from tracks with common points of
 818 spatial origin is a common approach used in the identification of b -jets.

819 Additional signatures of b -hadrons are as follows. Associated tracks and SVs can
 820 have a large transverse impact parameter d_0 as a result of the b -hadron displacement
 821 (as shown in Fig. 4.1). Additionally, since it is common for the b -hadron to decay to
 822 a c -hadron with non-negligible lifetime, tertiary vertices can be found within b -jets
 823 resulting from $b \rightarrow c$ decay chains.

824 These signatures are primarily identified using tracks associated to jets. As such,
 825 efficient and accurate track reconstruction is essential for high performance flavour
 826 tagging.

827 4.1.2 Challenges Facing b -hadron Reconstruction

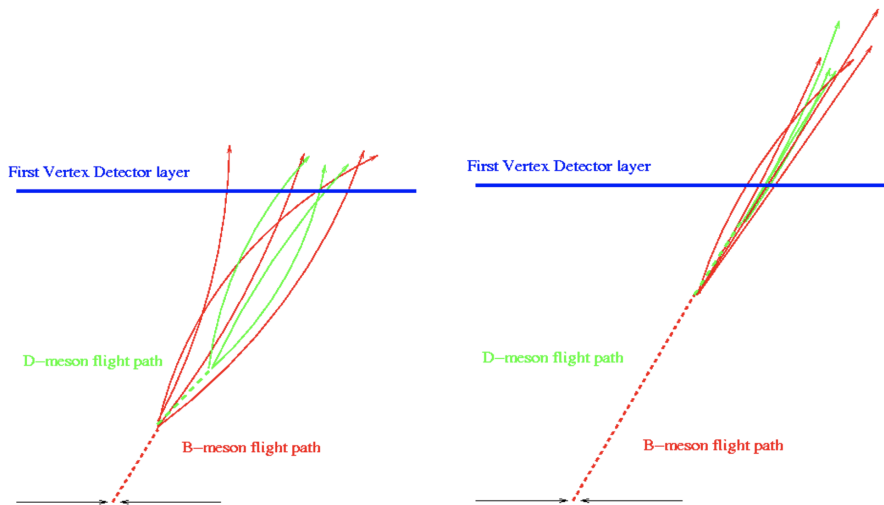


Figure 4.3: At lower p_T (left) the decay length of the b -hadron is reduced, and the resulting decay tracks are less collimated. At higher p_T (right) the b -hadron decay length increases and the resulting decay tracks are more collimated and have less distance over which to diverge before reaching detector elements. As a result, the ID may be unable to resolve charged depositions from different particles, instead reconstructing merged clusters.

828 As discussed, a necessary requirement for successful jet *b*-tagging is the efficient and
829 accurate reconstruction of the charged particle trajectories in the jet. For high p_T jets
830 ($p_T > 200$ GeV) this task becomes difficult due to a combination of effects. As the
831 jet energy increases, the multiplicity of tracks in the jet increases due to the presence
832 of additional fragmentation particles. Fragmentation and weak decay products also
833 become increasingly collimated as their inherited transverse momentum increases.
834 Together, these two effects lead to a high density of charged particles in the jet core,
835 which, given the finite resolution of the detector, makes reconstruction difficult.

836 At high energies, the increased decay length of *b*-hadrons (and *c*-hadrons) means
837 that decay products have less of an opportunity to diverge before reaching the
838 first tracking layers of the detector (shown in Fig. 4.3). If the weak decay takes
839 place close enough to a detector layer, or if the particles are otherwise sufficiently
840 collimated, charge deposits left by nearby particles may not be resolved individually,
841 instead being reconstructed as merged clusters. As discussed in Section 3.4.1, merged
842 clusters are generally rare, and so shared hits generally predict bad tracks and are
843 correspondingly penalised during track reconstruction. However, in the core of high
844 p_T *b*-jets the density of particles is high enough that the probability of cluster merging
845 increases dramatically. Successful reconstruction of such tracks requires the presence
846 of shared hits, but the presence of these can paradoxically end up impairing the
847 successfully reconstruction of the track. Furthermore, decays may also take place
848 inside the tracking detectors themselves, which at best leads to missing measurements
849 on the most sensitive detector layers, and at worst can lead to wrong inner layer hits
850 being added to displaced tracks, since the reconstruction process penalises tracks
851 without inner layer hits.

852 While the multiplicity of the fragmentation products increases with the *b*-hadron
853 p_T , the multiplicity of the products of the weak decay is unaffected. However, both
854 fragmentation and weak decay products have increased collimation at higher p_T . The
855 combination of effects described above makes reconstructing tracks in the core of
856 high p_T *b*-jets particularly challenging.

857 The above effects create two related, but distinct problems for *b*-tagging. The first
858 part is a drop in track reconstruction efficiency. As mentioned, tracks originating
859 from high energy *b*-hadron decay products can have a high rate of shared hits due
860 to the number of particles present in a high p_T *b*-jet and their relative collimation.
861 Additionally, tracks may be missing hits on the inner layers of the detector in the

can't find
source of
this image,
will have to
reproduce

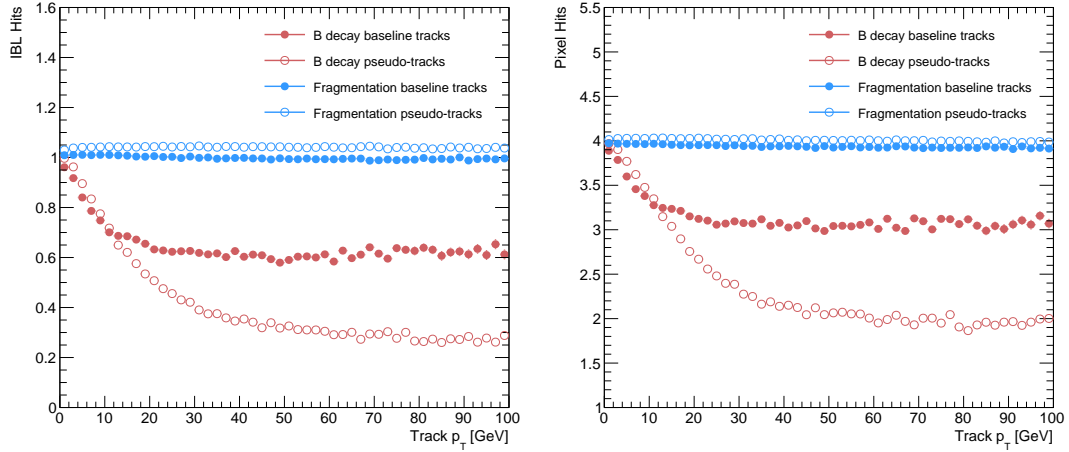


Figure 4.4: Hit multiplicities on the IBL (left) and the pixel layers (right) as a function of the p_T of the reconstructed track. Tracks from the weak decay of the b -hadron are shown in red, while fragmentation tracks (which are prompt) are in blue. For each of these, standard tracks and pseudo-tracks are plotted. Hit multiplicities on the pseudo-tracks at high p_T due to the increased flight of the b -hadron. The baseline tracks have more hits than the pseudo-tracks, indicating that they are being incorrectly assigned additional hits.

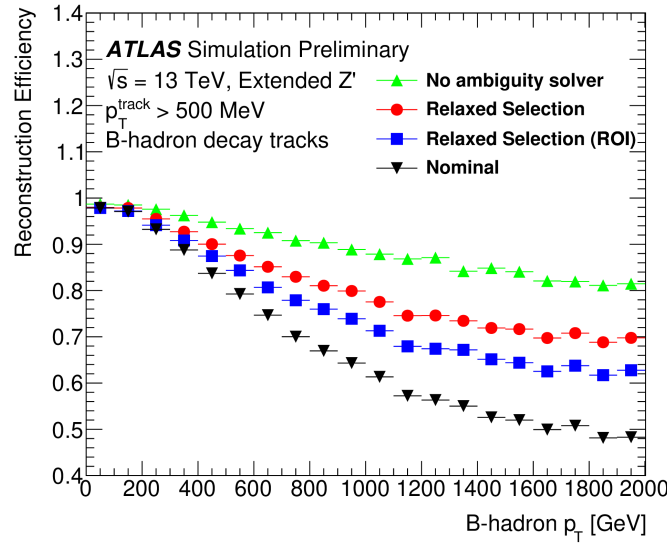


Figure 4.5: b -hadron decay track reconstruction efficiency as a function of truth b -hadron p_T [79]. Nominal track reconstruction is shown in black, while the track reconstruction efficiency for track candidates (i.e. the pre-ambiguity solver efficiency) is shown in green. For high- p_T b -hadrons, the ambiguity solver is overly aggressive in its removal of b -hadron decay tracks. Suggestions for the improvement of the track reconstruction efficiency in this regime by the loosening of cuts in the ambiguity solver are shown in blue and red.

862 case of displaced decays. The presence of shared and missing hits reduces a track's
863 score in the ambiguity solver meaning that higher ranking, but potentially worse,
864 track candidates are processed first and take ownership of the hits. This can make
865 it difficult for otherwise reasonable b -hadron decay tracks to meet the ambiguity
866 solver's stringent track quality requirements, leading to their rejection at this stage
867 as shown in Fig. 4.5.

868 The second part of the problem is that, due to the high multiplicity of clusters
869 available for assignment in the vicinity of the typical high energy b -hadron decay
870 track, and also given the strong positive bias of the ambiguity solver towards those
871 tracks with precise pixel measurements (especially the innermost IBL measurement),
872 many b -hadron decay tracks are assigned incorrect inner layer hits. This is only a
873 problem for those decay products which were produced inside the pixel detector
874 as a result of a long-flying b -hadron, and so do not have a correct hit available
875 for assignment. The incorrect hits may skew the parameters of the track, which
876 can in turn mislead the downstream b -tagging algorithms. In particular, b -tagging
877 algorithms rely heavily on the transverse impact parameter significance $s(d_0)$ of the
878 track. The quality of this measurement is expected to be adversely affected by wrong
879 inner-layer hits on the track.

880 The combination of reduced reconstruction efficiency and incorrectly assigned hits is
881 thought to be the cause of the observed drop in b -tagging efficiency at high energies,
882 however further study is required to determine which effect may dominate.

include plot
from sebs
study show-
ing they are
approx simi-
lar impacts?
or just men-
tion result?

883 4.2 Investigations into High p_T b -hadron Tracking

884 In Section 4.2.1 pseudotrack, a key tool for studying the ideal tracking performance
885 of the ATLAS detector, are used to study the baseline hit-to-track association in
886 the dense cores of high- p_T b -jets. Section 4.2.2 details a study which investigated
887 modifying the global track fitter to improve reconstruction performance in this
888 regime.

889 4.2.1 Pseudo-tracking

890 Pseudo-tracking uses Monte Carlo truth information to group together all the hits left
891 by each truth particle. Each group of hits which passes basic quality requirements is
892 directly used in a full resolution track fit. If the track fit is successful, a “pseudo-track”
893 track is created and stored. If the track fit fails, or the collection of hits does not pass
894 the basic quality requirements (for example because of a lack of hits) then the particle
895 is said to be un-reconstructable. In this way, pseudo-tracking performance represents
896 the ideal reconstruction performance given the ATLAS detector, with perfect hit-
897 to-track association and and track reconstruction efficiency. The approach was
898 introduced in [80] as a way to obtain a fast approximation of tracking reconstruction
899 for simulated data, however the technique has become a useful tool for studying
900 tracking performance in general [54].

901 The ambiguity solver is not run for pseudo-tracks. However, if the standard track
902 collection is produced alongside the pseudo-tracks, then cluster splitting neural
903 networks will be run for the standard tracks, and the resulting classification of
904 clusters will be propagated to hits on pseudo-tracks. This quirk allows one to study
905 the inefficiencies of the cluster splitting process, and relatedly to determine whether
906 shared hit cuts in the ambiguity solver are too loose or too tight. The fraction of
907 hits that are shared for the IBL and the B-layer is shown in Fig. 4.6. The shared
908 hits on pseudo-tracks represent correctly assigned hits from merged clusters that
909 were not able to be classified as split by the cluster splitting neural networks. As
910 such, these represent the number of shared hits the ambiguity solver should aim to
911 allow. For shared hits on the IBL for particles produced before the IBL, the cuts
912 appear to be successful in disallowing excessive numbers of shared hits. However, the
913 ambiguity solver fails to limit shared hits for those particles produced after the IBL,
914 reflecting the previously discussed problem of displaced tracks picking up incorrect
915 hits. Meanwhile, it is clear that for the B-layer, the ambiguity solver is being overly
916 aggressive in its rejection of shared hits.

917 4.2.2 Global χ^2 Fitter Outlier Removal

918

919 This section documents ongoing progress into improving hit assignments using the
920 Global χ^2 Fitter (GX2F) to prevent wrong hits from being assigned to tracks during

discuss
whether to
keep this
section

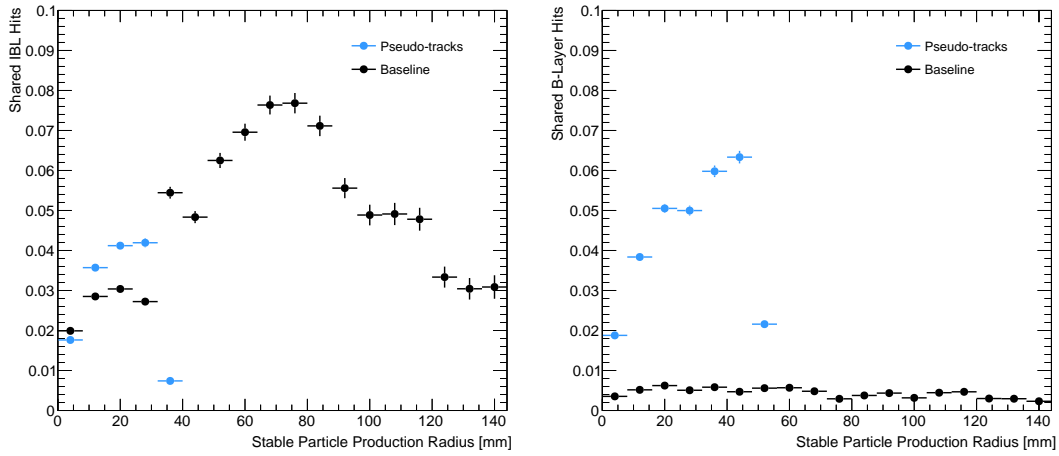


Figure 4.6: The rate of shared hits on b -hadron decay tracks on the IBL (left), and the B-layer (right), as a function of the production radius of the b -hadron decay product. Pseudo-tracks represent ideal performance given the ATLAS detector, and given also the efficiency of the NN cluster splitting algorithms.

the track fit. This is in contrast to the approach discussed in [cref sec:refit](#), which attempts to identify and remove wrong hits after the reconstruction of the track (of which the track fit is a part). As part of the track fit, an outlier removal procedure is run, in which suspicious hits are identified and removed. The GX2F code, as a relatively low-level component of track reconstruction, has not undergone significant modification for several years. During this time, a new tracking sub-detector, the IBL, was installed, and subsequently precise detector alignments have been derived. The motivation for looking at the GX2F is that these changes may require re-optimisation of the GX2F code, and in particular the outlier removal procedures. Further motivation for this approach comes from the low rate of labelled outliers in baseline tracking. For example, while approximately 15% of B hadron decay tracks have a wrong IBL hit (a value which only increases with the p_T of the B), less than 1% of these tracks have had their IBL hit labelled and removed as an outlier. This section documents an attempt to improve hit assignment the Global χ^2 Fitter (GX2F) to prevent wrong hits from being assigned to tracks during the track fit. This is in contrast to the approach discussed in [crefsec:refit](#), which attempts to identify and remove wrong hits after the reconstruction of the track (of which the track fit is a part). As part of the track fit, an outlier removal procedure is run, in which suspicious hits are identified and removed. The motivation for this approach comes from the low rate of labelled outliers in baseline tracking. For example, while

941 approximately 15% of B hadron decay tracks have a wrong IBL hit (a value which
 942 only increases with the p_T of the B), less than 1% of these tracks have had their IBL
 943 hit labelled and removed as an outlier.

944 Implementation

945 The outlier removal procedure for the pixel detector is described in this section. The
 946 states (also called measurements, or hits) on the track are looped over in order of
 947 increasing radial distance to the beam pipe. For each state, errors $\sigma(m_i)$ on the
 948 measurement of the transverse and longitudinal coordinates are calculated. These
 949 errors are dependent on the sub-detector which recorded the measurement (as some
 950 sub-detectors are more precise than others). Additionally, a residual displacement
 951 $r_i = m_i - x_i$ between the predicted position of the track x_i (inclusive of the current
 952 measurement), and the position of the measurement itself, m_i , is calculated. The
 953 pull p_i on the track state due to the current measurement is calculated according to

$$p_i = \frac{m_i - x_i}{\sqrt{\sigma(m_i)^2 - \sigma(x_i)^2}} \quad (4.2)$$

954 This pull is computed for the transverse and longitudinal coordinates of the mea-
 955 surement, and the maximum of the two is selected and checked to see if it exceeds a
 956 certain threshold. If it does, the hit will be removed, after some additional checks are
 957 made to confirm or deny the presence of the outlier. The threshold is set as a member
 958 variable `m_outlcut`. The results of varying this cut are described in Section 4.2.2.

959 Cut Optimisation

960 A systematic variation of the cut point `m_outlcut` has been carried out. The value of
 961 `m_outlcut` was reduced from 4 down to 1.75, a change which affects all silicon layers
 962 (the TRT has separate outlier removal logic). Furthermore, a specific cut for the IBL
 963 was introduced, and is set to 1.25. A second cut, `TrackChi2PerNDFCut`, is also used
 964 in the outlier removal. This value was reduced from 7 to 4. Finally, instead of taking
 965 the maximum of the pulls in the longitudinal and transverse directions, a quadrature
 966 sum is taken of these two values and used. This variation is labelled “Mod GX2F” in
 967 plots.

968 The results, demonstrating a reduction in wrong hit assignment whilst also improving
 969 slightly the good good hits assigned to tracks, are shown in Fig. 4.7. The improve-
 970 ments are also observed when looking inclusively in all tracks, which removes the
 need for a specific b -jet ROI. An improvement, though modest, of all track parameter

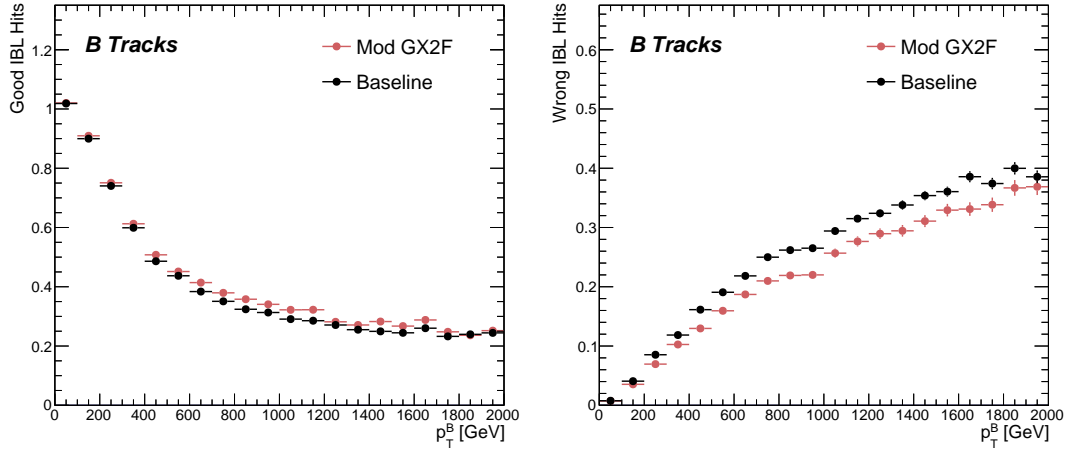


Figure 4.7: Profiles, as a function of parent b -hadron p_T , of good (left) and wrong (right) hit assignment rates on the IBL for tracks using baseline tracking (black), the modified version of the outlier removal procedure (red).

971 resolutions and pulls is observed. Some results are shown in Figs. 4.7 and 4.8, whilst
 972 the remainder of the plots can be found in the talks linked on the task’s Jira page.
 973 The results demonstrate an improvement in hit assignment, unchanged reconstruction
 974 efficiency, and modest improvement in track parameter resolutions and pulls. In
 975 addition, the truth match probability of track is unchanged, suggesting that there is
 976 no increase in fake track rates. The changes are expected to have a negligible impact
 977 on computational resources.

979 4.3 Conclusion

980 In this section, the difficulties facing efficient and accurate track reconstruction,
 981 and hence performant b -tagging, have been outlined. The ambiguity solver, which
 982 attempts to clean or reject tracks which have excessive number shared hits, is shown
 983 to be overly aggressive in the removal of b -hadron decay product track candidates.
 984 The ambiguity solving process relies on many pre-defined cuts which have not been

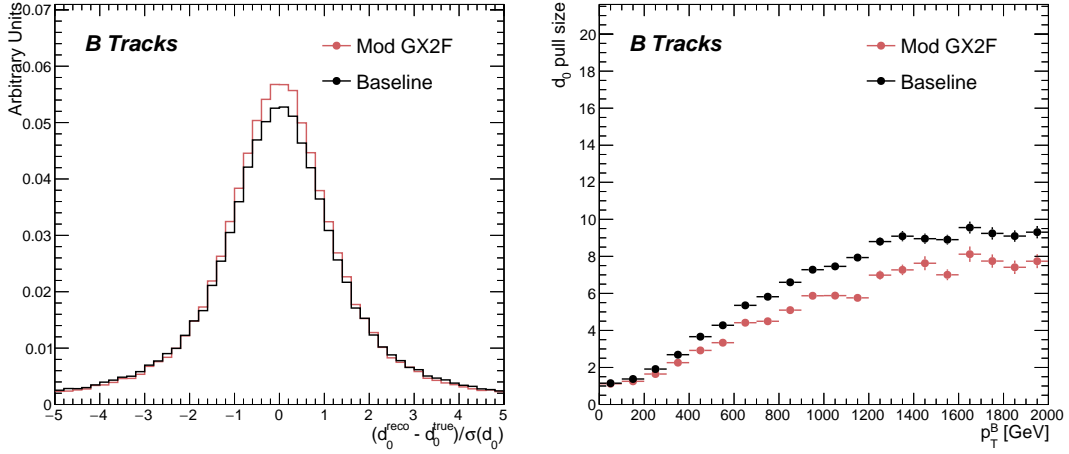


Figure 4.8: (left) B hadron decay track d_0 pulls for baseline and modified GX2F tracks. (right) The magnitude of the decay track d_0 pull as a function of B hadron transverse momentum.

985 optimised for high transverse momentum *b*-hadron track reconstruction. These
 986 conclusions have motivated further ongoing studies into the improvement of the
 987 track reconstruction in dense environments and the high- p_T regime, such as those in
 988 Ref. [79].

989 An optimisation of the outlier removal process in the global χ^2 fitter was also carried
 990 out. Though the results show some improvement over the baseline tracking scenario,
 991 these results need to be expanded upon by looking at the impact on the downstream
 992 *b*-tagging algorithms before putting them into production. As there are some known
 993 data-MC discrepancies, fine tuned optimisation such as the work presented here
 994 presents an opportunity to over-optimize the tracking algorithms to MC. The studies
 995 were carried out in Release 21 of the ATLAS software, and need to be reproduced
 996 using the newer Release 22 to confirm the results against other changes in the baseline
 997 tracking configuration.

998 **Chapter 5**

999 **Track Classification MVA**

1000 The chapter details work on implementing a multivariate algorithm (MVA) to predict
1001 the truth origin of reconstructed tracks. An introduction to formalisms of machine
1002 learning is given in Section 5.1. In Section 5.2, the truth origin label is defined,
1003 and in Section 5.3 these labels are used to train a machine learning model that can
1004 effectively discriminate between good and fake tracks. Several studies motivated this
1005 work by demonstrating that at high p_T , b -tagging performance was degraded by the
1006 presence of large numbers of poorly reconstructed or fake tracks. If an algorithm
1007 could be trained to detect fake tracks, these could be removed before their input to
1008 the b -tagging algorithms with the aim of improving performance.

1009 **5.1 Machine Learning Background**

1010 Over the past few decades, machine learning (ML) techniques have become in-
1011 creasingly popular in high energy physics experiments due the increased volumes
1012 of high-dimensional data and improvements in the field of machine learning (in
1013 particular deep learning). Machine learning is the process in which a computer
1014 program uses data to learn suitable parameters for a predictive model model. This
1015 is opposed to explicitly providing instructions on how to perform a task. A subfield
1016 known as *supervised learning* is used in this work, and consists of exposing a model
1017 to a large number of labelled examples in order to extract relationships between the
1018 input data and their labels. These relationships are often complex, and explicitly

1019 programmed rules can fail to fully capture the relationships between inputs and
1020 outputs.

1021 In the simplest case, a set of m labelled training examples $S = \{(x_1, y_1), \dots, (x_m, y_m)\}$
1022 is collected. Each element (x_i, y_i) consists of a input vector $x_i \in \mathbb{R}^{\text{input}}$, and the
1023 corresponding label y_i . In classification problems, these labels are integer *class*
1024 *labels* $y_i \in \{0, \dots, N - 1\}$, where N is the number of classes, which specify which
1025 of a pre-determined set of categorical classes the training example belongs to. The
1026 rest of the discussion in this chapter is limited to binary classification problems
1027 ($N = 2$). The two classes are often referred to as signal ($y_i = 1$) and background
1028 ($y_i = 0$), which need to be separated. Collecting sufficient and suitable data is one
1029 of the primary challenges of machine learning, as such data is not always readily
1030 available. Fortunately, sophisticated tools to simulate particle collisions have already
1031 been developed by the scientific community [81, 82]. These tools play a key role in
1032 generating a suitably large amount of labelled data which is used to train algorithms.
1033 More detail on the input datasets is given in Section 5.3.1.

1034 After obtaining suitable training data, the next step is to define a model. Given an
1035 input domain $\mathbb{R}^{\text{input}}$ and an output domain $(0, 1)$, the model $f_\theta : \mathbb{R}^{\text{input}} \rightarrow (0, 1)$ is a
1036 parameterised functional mapping from input space to output space. Given an input
1037 example x_i and a set of parameters θ , the model outputs a prediction $\hat{y}_i \in (0, 1)$ for
1038 the true label y_i , as in

$$f_\theta(x_i) = \hat{y}_i. \quad (5.1)$$

1039 The output \hat{y}_i is in the interval $(0, 1)$ so as to be interpreted as the probability
1040 that the input example x_i belongs to the signal class. The parameters θ of the
1041 model are randomly initialised, however the model is designed to be expressive
1042 enough to correctly map the inputs x_i to the outputs y_i given the correct choice of
1043 parameters. The model is then trained, which amounts to showing the model a series
1044 of labelled training examples and modifying the parameters of the model based on
1045 its performance.

5.1.1 Neural Networks

Neural networks (NNs) are a common choice for the machine learning model f since they have the ability to approximate any function [83] and are easy to train via backpropagation [84].

Artificial Neurons

The basic functional component of a NN is the *artificial neuron* or node, which is loosely inspired by a mathematical model of a biological neuron [85, 86]. An artificial neuron is defined by its parameters or *weights* θ and a choice of activation function. Each neuron takes a fixed number of inputs and computes the dot product of the input and weight vectors $x^T \theta$ and additionally adds a constant bias term θ_0 . This term plays the role of a trainable constant value that is independent of the inputs.

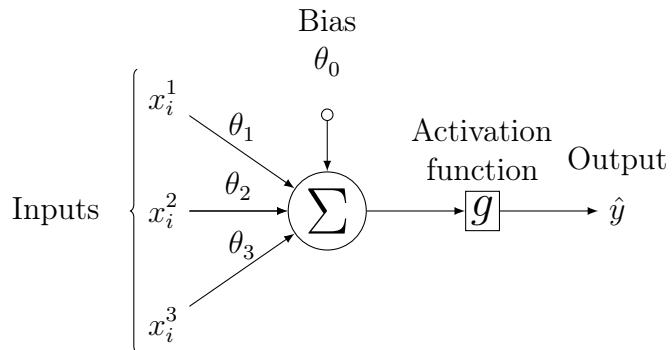


Figure 5.1: A diagram displaying the logical flow of a single neuron with three inputs x_i^j . Each input is multiplied by a weight θ_j , and the resulting values are summed. A bias term θ_0 is added, and the result is passed to an activation function. Each neuron can be thought of as a logistic regression model.

The dot product is fed into an activation function g . The activation function has several uses, most notably acting as a source of non-linearity and bounding the output of the neuron. Some common activation functions are shown in Fig. 5.2. The choice of activation function can have implications for the performance and convergence of the network, since the gradient of g is used to compute the weight updates during training. This is also why input data is normalised to have zero mean and unity variance [87].

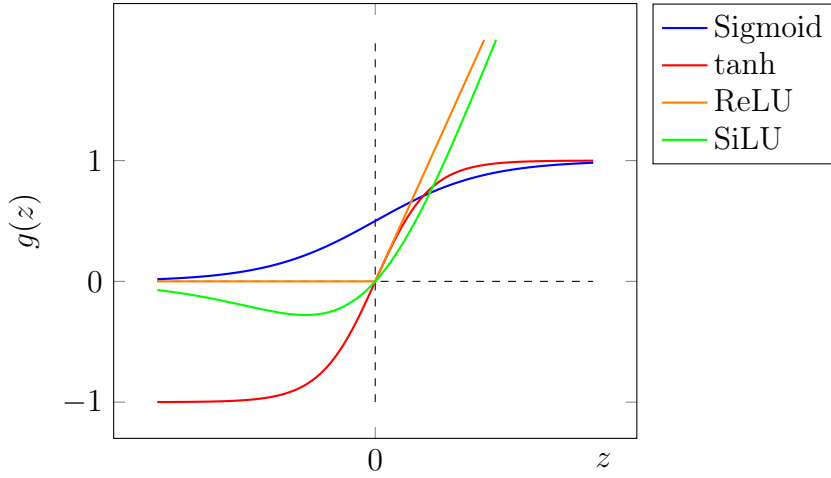


Figure 5.2: Several common choices for the activation function g of an artificial neuron.

1064 Networks

1065 Several neurons are linked together in layers to form a neural network. The inputs
 1066 are propagated layer-by-layer through the network until reaching the final output
 1067 layer. The number of layers and neurons per layer are important hyperparameters
 1068 (those parameters which are not optimised as part of the training process) which
 1069 influence the performance of the model. In the case of binary classification, the final
 1070 output layer consists of a single neuron with a sigmoid activation

$$g(z) = \frac{1}{1 + e^{-z}}, \quad (5.2)$$

1071 which is bounded between zero and one allowing the final output to be interpreted
 1072 as the probability that the input sample belongs to the signal class. NNs have the
 1073 crucial property of being differentiable functions, which facilitates training process
 1074 described in the next section.

1075 5.1.2 Training with Gradient Descent

1076 A training algorithm is used to optimise the weights of a NN after exposure to the
 1077 training data. The training algorithm works minimising a loss function L , which
 1078 quantifies the error in the model's predictions for a given input. NNs are commonly
 1079 trained using backpropagation in combination with a variant of stochastic gradient

descent to iteratively update the model parameters. In binary classification problems, the binary cross entropy given in Eq. (5.3) loss if often used.

$$L(x_i, \theta) = y_i \ln[f_\theta(x_i)] + (1 - y_i) \ln[1 - f_\theta(x_i)] \quad (5.3)$$

Since the model f is differentiable, the error for each parameter θ_i can be computed by taking partial derivative of L with respect to the parameter. Updated parameters θ'_i are calculated by updating the original parameter in the direction which reduces the loss.

$$\theta'_i = \theta_i - \alpha \frac{\partial L}{\partial \theta_i} \quad (5.4)$$

The hyperparameter α is known as the *learning rate* and dictates the size of the step taken in the direction of the slope. The errors for each parameter are efficiently calculated using the backpropagation algorithm [84]. The process of updating weights is repeated until the weights converge the network is trained. In practice, small batches of the input data are shown to the network at a time. For each batch the average loss is calculated and the network's weights are updated. There are many extensions and variations of the gradient descent algorithm. This work uses the Adam optimiser which adds momentum to the weight updates (dampening oscillations) and an adaptive per-parameter learning rate [88].

5.2 Track Truth Origin Labelling

Crucial to supervised learning techniques are the ground truth class labels which the machine learning model is trained to predict. A set of track truth labels which a high degree of granularity have been implemented in the ATLAS software stack, and are listed in Table 5.1. The labelling scheme has designed to be useful beyond the classification of good and fake tracks. The origins are determined by analysing the detailed simulated truth record for the truth particle associated with each track. Tracks are associated with truth particles by selecting the truth particle with the highest *truth-matching probability* (TMP), defined in Eq. (5.5). This is a weighted sum of the number of hits on a track which are from the same truth particle, versus the total number of hits on the track. The weights are subdetector-dependent are designed to account for the varying number of layers (and therefore expected number

1107 of hits) in each of the subdetectors.

$$\text{TMP} = \frac{10N_{\text{Pix}}^{\text{good}} + 5N_{\text{SCT}}^{\text{good}} + N_{\text{TRT}}^{\text{good}}}{10N_{\text{Pix}}^{\text{all}} + 5N_{\text{SCT}}^{\text{all}} + N_{\text{TRT}}^{\text{all}}} \quad (5.5)$$

1108 For the fake track classification tool, the origins in Table 5.1 are used to construct a
1109 binary label by labelling all fake tracks background, and all other tracks as signal.
1110 The fake track classifier is then trained to distinguish between these two categories
1111 of tracks. Fake tracks are also defined using the TMP, with a $\text{TMP} < 0.5$ giving a
1112 track the label of fake. Fake tracks are made up of combinatorial fakes, which are
1113 tracks which do not correspond to the trajectory of any truth particle, and poorly
1114 reconstructed tracks, which may somewhat resemble the trajectory of a truth particle
1115 but may be off due to the presence of some wrong hits on the track.

Truth Origin	Description
Pileup	From a pp collision other than the primary interaction
Fake	Created from the hits of multiple particles
Primary	Does not originate from any secondary decay
fromB	From the decay of a b -hadron
fromBC	From a c -hadron decay which itself is from the decay of a b -hadron
fromC	From the decay of a c -hadron which is not from the decay of a b -hadron
OtherSecondary	From other secondary interactions and decays

Table 5.1: Truth origins which are used to categorise the physics process that led to the production of a track. Tracks are matched to charged particles using the truth-matching probability [55]. A truth-matching probability of less than 0.5 indicates that reconstructed track parameters are likely to be mismeasured and may not correspond to the trajectory of a single charged particle. The “OtherSecondary” origin includes tracks from photon conversions, K_S^0 and Λ^0 decays, and hadronic interactions.

1116 5.3 Fake Track Identification Tool

1117 The rate of fake tracks increases at high transverse momentum as shown in Fig. 5.3 due
1118 to the difficulties in track reconstruction outlined in Section 4.1.2. The performance
1119 of b -tagging algorithms is reduced as a direct result of the presence of these fake
1120 tracks as shown for SV1 in Fig. 5.4, where the light-efficiency decreases by up to 35%
1121 at a b -efficiency of 35%.

To identify and remove fake tracks, a NN classification tool was trained with good tracks as the signal class and fake tracks as the background class. Due to the imbalance between the two classes (with fake tracks being relatively uncommon), a weight was added to the loss function for the background class to account for this. The NN was made up of two hidden layers with 100 nodes per layer. The ReLU activation function was used in conjunction with the Adam optimiser with a learning rate of $1e-3$. Optimisation of the networks architecture has been carried out to ensure good performance with a relatively small number of learnable parameters. The model was trained using 40 million tracks with a further 1 million tracks each used for validation and testing.

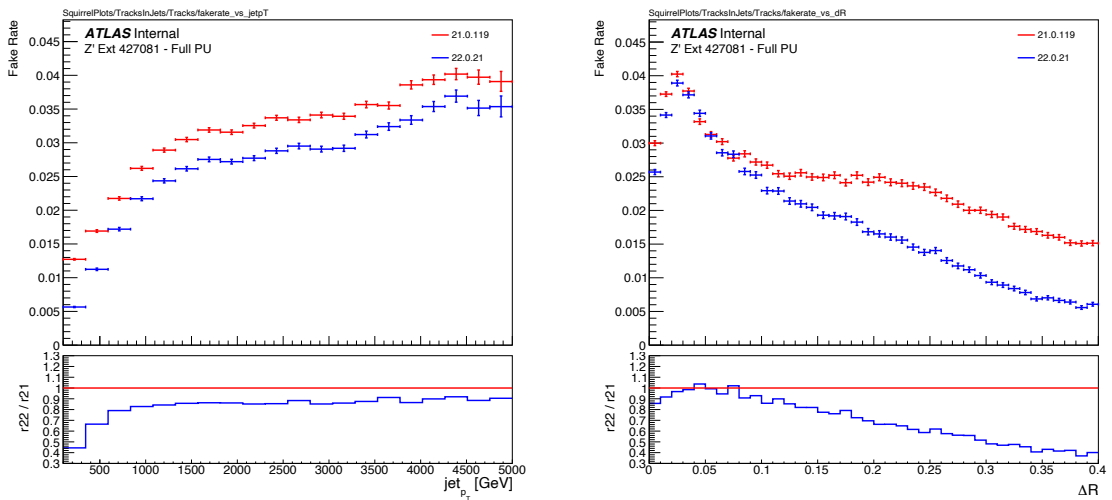


Figure 5.3: Rate of fake tracks as a function of jet transverse momentum (left) and ΔR (track, jet) (right). The rate of fake tracks increases significantly as a function of p_T , and also increases as the distance to the jet axis decreases, and the number of tracks in the jet increases (not shown).

Inputs to the model are described in Section 5.3.2, while fake track removal performance is given in Section 5.3.3.

5.3.1 Datasets

To train and evaluate the model, simulated SM $t\bar{t}$ and BSM Z' events initiated by proton-proton collisions at a center of mass energy $\sqrt{s} = 13$ TeV are used. The Z' sample is constructed in such a manner that it has a relatively flat jet p_T spectrum

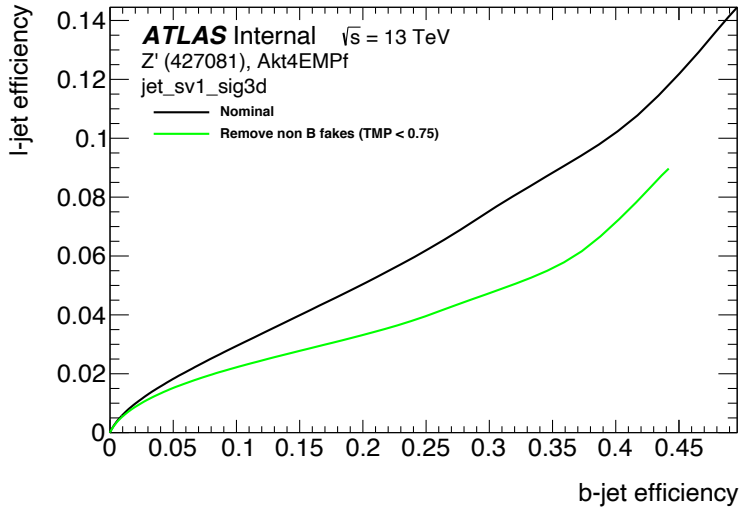


Figure 5.4: The light-jet efficiency of the low level tagger SV1 as a function of b -jet efficiency for the nominal tracking setup (black) and for the case where fake tracks which are not from the decay of a b -hadron are removed. The light-jet efficiency is decreased, demonstrating that the presence of fake tracks is detrimental to algorithm performance.

up to 5 TeV and decays democratically to an equal numbers of b -, c - and light- jets.
 The generation of the simulated event samples includes the effect of multiple pp interactions per bunch crossing with an average pileup of $\langle \mu \rangle = 40$, which includes the effect on the detector response due to interactions from bunch crossings before or after the one containing the hard interaction.
 The $t\bar{t}$ events are generated using the POWHEGBOX [89–92] v2 generator at next-to-leading order with the NNPDF3.0NLO [93] set of parton distribution functions (PDFs). The h_{damp} parameter¹ is set to 1.5 times the mass of the top-quark (m_{top}) [94], with $m_{\text{top}} = 172.5$ GeV. The events are interfaced to PYTHIA 8.230 [95] to model the parton shower, hadronisation, and underlying event, with parameters set according to the A14 tune [96] and using the NNPDF2.3LO set of PDFs [97]. Z' events are generated with PYTHIA 8.2.12 with the same tune and PDF set. The decays of b - and c -hadrons are performed by EVTGEN v1.6.0 [98]. Particles are passed through the ATLAS detector simulation [99] based on GEANT4 [100].

¹The h_{damp} parameter is a resummation damping factor and one of the parameters that controls the matching of POWHEG matrix elements to the parton shower and thus effectively regulates the high- p_T radiation against which the $t\bar{t}$ system recoils.

1152 Additionally, all jets are required not to overlap with a generator-level electron or
1153 muon from W boson decays. Jets are required to have a pseudorapidity $|\eta| < 2.5$
1154 and $p_T > 20 \text{ GeV}$. Additionally, a standard selection using the Jet Vertex Tagger
1155 (JVT) algorithm at the tight working point is applied to jets with $p_T < 60 \text{ GeV}$ and
1156 $|\eta| < 2.4$ in order to suppress pile-up contamination [101].

1157 5.3.2 Model Inputs

1158 The fake track MVA is given two jet variables and 20 tracking related variables
1159 for each track fed into the network. The jet transverse momentum and signed
1160 pseudorapidity constitute the jet-level inputs, with the track-level inputs listed in
1161 Table 5.2. The track parameters and hit pattern are key indicators of whether or
1162 not a track is fake. The FracRank variable is the ordered index of the track divided
1163 by the total number of tracks in the event. The ambiguity solver processes track
1164 candidates iteratively (see Section 3.4.1), and the order in which tracks are accepted
1165 is preserved. Tracks which do not require cleaning (i.e. the removal of suspect shared
1166 hits) are likely to be accepted earlier on. Hence the FracRank variable gives an
1167 indication of how easy it was for the track to be reconstructed.

1168 Track selection follows the loose selection described in Ref. [102] and outlined in
1169 Table 5.3, which was found to improve the flavour tagging performance compared to
1170 previous tighter selections, whilst ensuring good resolution of tracks and a low fake
1171 rate [55]. Inputs are scaled to have a central value of zero and a variance of unity
1172 before training and evaluation.

1173 5.3.3 Results

1174 In order to evaluate the of the fake track classification tool, a orthogonal test sample
1175 of 1 million tracks in jets in the combined $t\bar{t}$ and Z' samples was used. The continuous
1176 scalar output from the NN model is interpreted as the probability that a given track
1177 is a good track (i.e. not fake). Fig. 5.5 shows the performance of the fake track
1178 classification MVA. The signal and background classes are well separated in the
1179 output of the tool. Also shown is a receiver operating characteristic (ROC) curve,

Jet Input	Description
p_T	Jet transverse momentum
η	Signed jet pseudorapidity
Track Input	Description
p_T	Track transverse momentum
ΔR	Angular distance between the track and jet
d_0	Closest distance from the track to the PV in the longitudinal plane
z_0	Closest distance from the track to the PV in the transverse plane
nIBLHits	Number of IBL hits
nPixHits	Number of pixel hits
nSCTHits	Number of SCT hits
nTRTHits	Number of TRT hits
nBLHits	Number of B-layer hits
nIBLShared	Number of shared IBL hits
nIBLSplit	Number of split IBL hits
nPixShared	Number of shared pixel hits
nPixSplit	Number of split pixel hits
nSCTShared	Number of shared SCT hits
r_{first}	Radius of first hit
nDOF	Number of degrees of freedom on the track
FracRank	Ambiguity solver ordering variable

Table 5.2: Input features to the fake track classification NN. Basic jet kinematics, along with information about the reconstructed track parameters and constituent hits are used. Shared hits, are hits used on multiple tracks which have not been classified as split by the cluster-splitting neural networks [55], while split hits are hits used on multiple tracks which have been identified as merged.

Parameter	Selection
p_T	> 500 MeV
$ d_0 $	< 3.5 mm
$ z_0 \sin \theta $	< 5 mm
Silicon hits	≥ 8
Shared silicon hits	< 2
Silicon holes	< 3
Pixel holes	< 2

Table 5.3: Quality selections applied to tracks, where d_0 is the transverse IP of the track, z_0 is the longitudinal IP with respect to the PV and θ is the track polar angle. Shared hits are hits used on multiple tracks which have not been classified as split by the cluster-splitting neural networks [55]. Shared hits on pixel layers are given a weight of 1, while shared hits in the SCT are given a weight of 0.5. A hole is a missing hit, where one is expected, on a layer between two other hits on a track.

1180 which plots the rate of true positives against the rate of false positives over a scan of
 1181 cut points on the NN output ranging from zero to one. The area under the curve
 1182 (AUC) gives a summary of the aggregate classification power of the model. The fake
 1183 track classification tool achieves an AUC of 0.935 for all tracks, which is indicative of
 1184 a well-performing model. Considering only tracks from b -hadron decays, this value
 1185 drops slightly to 0.928.

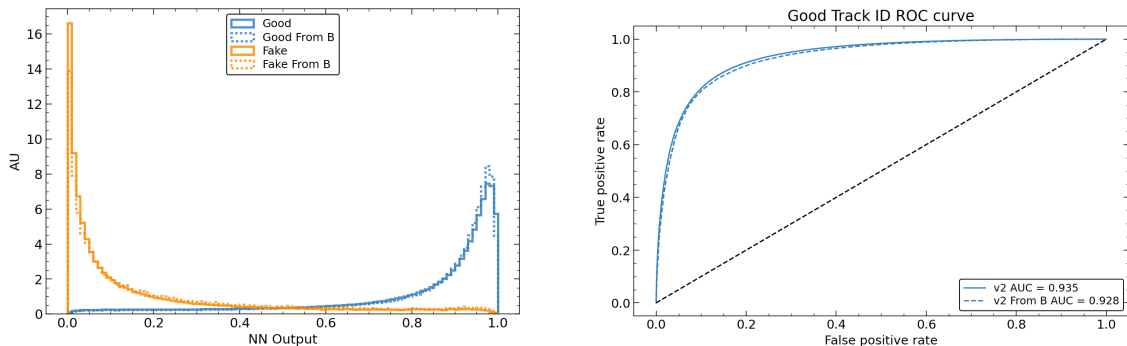


Figure 5.5: (left) Normalised histogram of the model output separated for good and fake tracks, and further separated by those tracks which are from the decay of a b -hadron.
 (right) The ROC curve for all tracks (solid line) and tracks from the decay of a b -hadron (dashed line).

1186 Good and fake track efficiencies at two different NN output cut points are shown
 1187 in Table 5.4. The results demonstrate that the tool is effective in retaining 98.8%

1188 of good tracks, while correctly identifying (and therefore enabling the removal of)
1189 45.6% of fake tracks. Table 5.4 also shows that a significant amount of tracks which
1190 are labelled as both fake and from the decay of a b -hadron are also removed.

MVA Output Cut	Good Track Efficiency		Fake Track Efficiency	
	All	From b	All	From b
0.06	98.8%	98.9%	45.6%	39.8%
0.12	97.3%	97.5%	59.4%	53.6%

Table 5.4: Good and fake track selection efficiencies for the combined $t\bar{t}$ and Z' samples. Two working points are defined, cutting on the NN output at 0.06 and 0.12. The continuous output of the model allows for the tuning of good and fake track identification efficiencies.

1191 After initial tests and investigation, it was found that fake tracks which were the
1192 result of b -hadron decays actually aided b -tagging performance. The application of a
1193 single tool which removed all fake tracks was therefore not optimal. A second tool
1194 was trained in the same manner of the first, this one was designed to distinguish
1195 between those tracks which were from the decay of a b -hadron and those which were
1196 not. A 2-dimensional cut was then used to only reject those tracks that had a high
1197 probability of being fake, and also a low probability of being a b -hadron decay track.

1198 The light-jet efficiency of SV1 is successfully reduced when using the combined tools
1199 to remove fake tracks that are not from a b -hadron decay, as shown in Fig. 5.6. At
1200 a b -efficiency of 70%, the light-jet mistag rate for jets with $250 < p_T < 400$ GeV is
1201 reduced from 0.054 to 0.044, a relative improvement of approximately 20%. For jets
1202 in $400 < p_T < 1000$ GeV the mistage rate drops from 0.1 to 0.08 for a similar relative
1203 improvement of 20%. The performance of the track classification tools is also shown
1204 for JetFitter in Fig. 5.7. The results are generally consistent as for those from SV1,
1205 with up to a 20% improvement in the light-jet rejection for a given b -efficiency WP
1206 in the two jet p_T bins.

1207 5.4 Conclusion

1208 Fake tracks, which are prevalent in the core of high p_T jets, are shown to have an
1209 adverse impact on b -tagging performance. A ML tool to identify fake tracks has

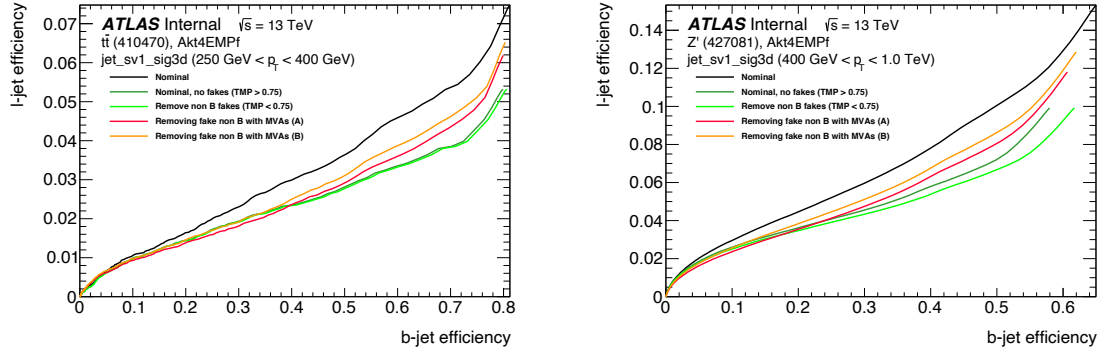


Figure 5.6: The effect of applying the fake track identification algorithm alongside the b -hadron decay track identification on the jet tagging performance of SV1 for jets with $250 \text{ GeV} < p_T < 400 \text{ GeV}$ (left) and for jets with $400 \text{ GeV} < p_T < 1 \text{ TeV}$ (right). The nominal SV1 light-jet rejection (black) is compared to two working points, labelled “A” (red) and “B” (orange) of fake track removal, which represent two different 2D working points of the track classification tools. Removal of fake tracks based on truth information is shown by the green curves.

been developed, which can be used to limit the number of fake tracks being inputted to downstream b -tagging algorithms. It was found that, since many b -hadron decay tracks are poorly reconstructed and thus marked as fake, it was necessary also to train a second algorithm to detect b -hadron decay tracks so that the removal of these tracks could be avoided. Removing fake and non- b decay tracks in this way was found to improve the light-jet mistagging rate of SV1 and JetFitter by up to 20% at high transverse momentum.

While removing tracks prior to their input to the low level tagging algorithms is shown here beneficial, a more performant alternative might be to keep these tracks but label them as being fake (for example using the output of the classification tool), and allow the tagging algorithms to take this into consideration, potentially still making use of some of the information. This is not straightforward with manually optimised taggers such as SV1 and JetFitter, but is possible with approaches such as those described in Chapter 6.

Tools which identify the origin of a given track have other potential uses. One application is to isolate a relatively pure sample of fake tracks which can be used to estimate the fake track rate in data, which would be useful for producing the recommendations for tracking systematic uncertainties. Another application would

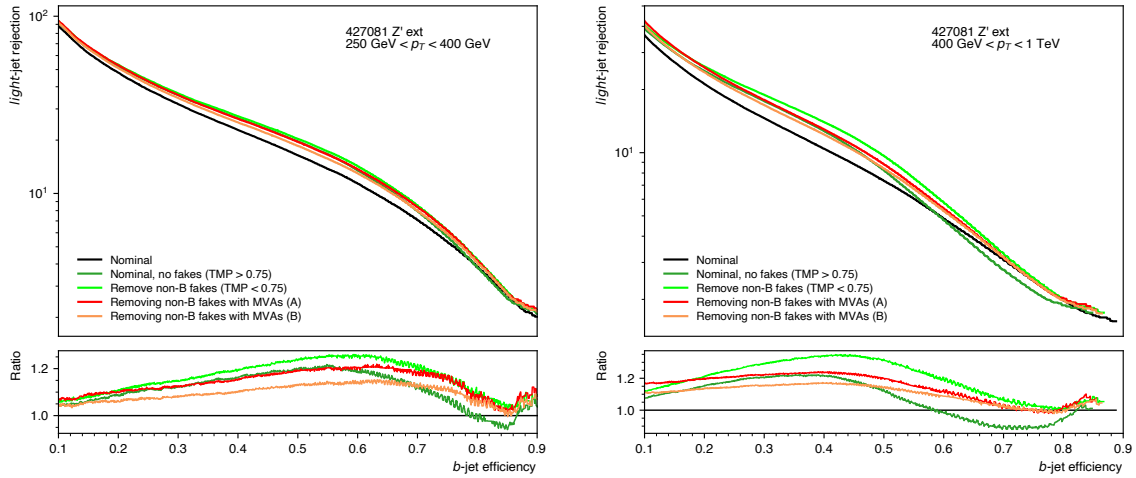


Figure 5.7: The effect of applying the fake track identification algorithm alongside the b -hadron decay track identification on the jet tagging performance of SV1 for jets with $250 \text{ GeV} < p_T < 400 \text{ GeV}$ (left) and for jets with $400 \text{ GeV} < p_T < 1 \text{ TeV}$ (right). The nominal SV1 light-jet rejection (black) is compared to two working points of fake track removal (orange and red). Removal of fake tracks based on truth information is shown by the green curves.

- 1228 be to use the b -hadron track identification tool to improve the track-to-jet association.
1229 Both applications are currently under investigation.
- 1230 The approach here works on a track-by-track basis, but a more sophisticated approach
1231 would consider the correlations between the tracks inside a jet, as shown in Chapter 6.
- 1232 Also left for future work is to simultaneously train a single tool which discriminates
1233 between all the truth origins listed in Table 5.1. Such a tool would be useful as a
1234 general purpose multiclass classifier.

₁₂₃₅

Chapter 6

₁₂₃₆

Graph Neural Network Flavour ₁₂₃₇ Tagger

₁₂₃₈ Some of the work in this chapter has previously been published in Ref. [103]. The
₁₂₃₉ author of this thesis was on the editorial team and was the primary author. As such,
₁₂₄₀ figures, tables and some text from the published note are reproduced here.

₁₂₄₁ As discussed in Chapter 4, flavour tagging is the identification of jets originating from
₁₂₄₂ b - and c -quarks. Flavour tagging is a critical component of the physics programme of
₁₂₄₃ the ATLAS experiment. It is crucial importance for the study of the Standard Model
₁₂₄₄ (SM) Higgs boson and the top quark, which decay preferentially to b -quarks [104, 105],
₁₂₄₅ and additionally for several Beyond Standard Model (BSM) resonances that readily
₁₂₄₆ decay to heavy flavour quarks [106].

₁₂₄₇ Existing flavour tagging algorithms, such as DL1r [107, 108], use as inputs the outputs
₁₂₄₈ from a number of low-level algorithms. The low-level algorithms each reconstruct
₁₂₄₉ various features of jets using the tracks which have been associated to the jet. The
₁₂₅₀ outputs from the low-level algorithms are then combined in a machine learning model.
₁₂₅₁ This chapter introduces GN1, a novel ML-based flavour tagging algorithm based on
₁₂₅₂ graph neural networks (GNNs).

₁₂₅₃ As opposed to the previous two-tiered approach described in Chapter 4, which requires
₁₂₅₄ the use of both low- and high-level algorithms, GN1 takes as inputs information from
₁₂₅₅ an unordered variable number of tracks to predict the jet flavour without requiring
₁₂₅₆ outputs from the intermediate low-level algorithms. In addition to predicting the
₁₂₅₇ flavour of the jet, the model predicts which physical processes produced the various

1258 jet tracks, and groups the tracks in the jet into vertices. These auxiliary training
1259 objectives provide valuable additional information about the contents of the jet and
1260 enhance the performance of the primary flavour prediction task.

1261 GN1 outperforms the existing ATLAS flavour tagging algorithms as shown in Sec-
1262 tions 6.5.1 and 6.5.2. For a b -jet efficiency of 70%, the light (c)-jet rejection is
1263 improved by a factor of ~ 1.8 (~ 2.1) for jets coming from $t\bar{t}$ decays with transverse
1264 momentum $20 < p_T < 250$ GeV. For jets coming from Z' decays with transverse
1265 momentum $250 < p_T < 5000$ GeV, the light (c)-jet rejection improves by a factor ~ 6
1266 (~ 2.8) for a comparative 30% b -jet efficiency.

1267 In Section 6.1, an overview of the approach used for GN1 is provided. An introduction
1268 to the theory of GNNs is provided in Section 6.2. Details of the experimental setup
1269 are provided in Section 6.3, while the architecture of GN1 is specified in Section 6.4.3.
1270 In Section 6.4.4, the training procedure is described, and in Section 6.5 the results
1271 are shown.

1272 6.1 Motivation

1273 GN1 is a monolithic approach to flavour tagging as illustrated in Fig. 6.1. The use
1274 of GNNs offers a natural way to classify jets with variable numbers of unordered
1275 associated tracks (see Section 6.2), while allowing for the inclusion of auxiliary
1276 training objectives [109, 110].

1277 The current ATLAS flavour tagger, DL1r [107], is a deep neural network which takes
1278 the outputs of a number of independently optimised “low-level” algorithms [59] as
1279 its inputs. Each of these low-level algorithms reconstructs a distinct feature of the
1280 experimental signature of heavy flavour jets using the tracks associated to the jet,
1281 and outputs some variables which are discriminating in the jet flavour.

1282 The low-level algorithms are a combination of manually optimised reconstruction
1283 algorithms, for example the SV1 and JetFitter algorithms that reconstruct displaced
1284 decay vertices, and trained taggers such as RNNIP and DIPS that use the IP and
1285 hit information from a variable number of tracks to identify the flavour of the
1286 jet [59, 102, 111, 112]. In contrast GN1 consists of only a single neural network, which
1287 takes the tracks as inputs along with some kinematic information about the jet. As a

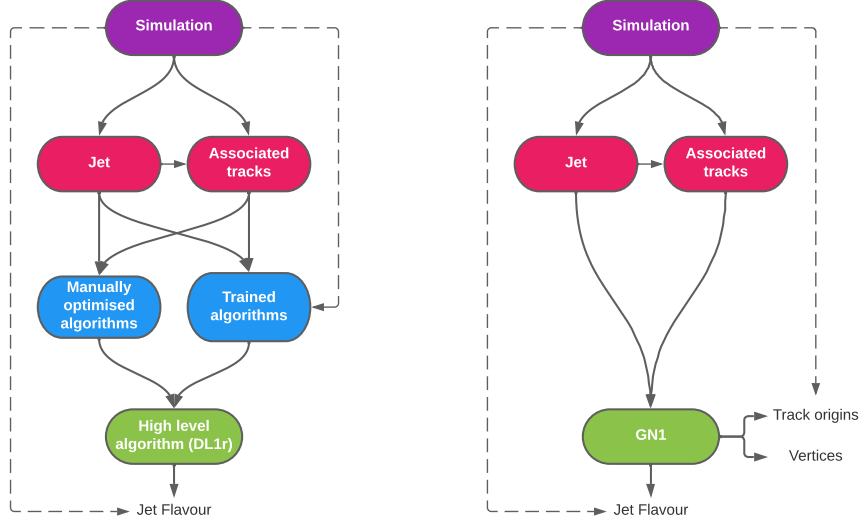


Figure 6.1: Comparison of the existing flavour tagging scheme (left) and GN1 (right). The existing approach utilises low-level algorithms (shown in blue), the outputs of which are fed into a high-level algorithm (DL1r). Instead of being used to guide the design of the manually optimised algorithms, additional truth information from the simulation is now being used as auxiliary training targets for GN1. The solid lines represent reconstructed information, whereas the dashed lines represent truth information.

1288 result, it does not depend on the outputs of any other flavour tagging algorithm. A
1289 simple training of the model fully optimises its parameters, representing a significant
1290 simplification with respect to the optimisation procedure for DL1r. This is particularly
1291 important when optimising the tagger for new regions of phase space (e.g. c -tagging or
1292 high- p_T b -tagging), or when the detector or charged particle reconstruction algorithms
1293 are updated.

1294 GN1 is trained to learn about the internal structure of the jet through the use of two
1295 auxiliary training objectives: the prediction of the underlying physics process from
1296 which each track originated, and the grouping of tracks originating from a common
1297 spatial position (i.e. a common vertex). These auxiliary objectives are meant to
1298 guide the neural network towards a more complete understanding of the underlying
1299 physics inside the jet, thereby removing the need for the low-level algorithms, which
1300 previously contained information about the underlying physics in their design. The
1301 training targets for the primary and auxiliary objectives are extracted from truth
1302 information, i.e. information that is only available in simulation, as opposed to
1303 reconstructed quantities available in both collision data and simulation.

1304 In this chapter, the following advantages of the GN1 approach will be demonstrated:

- 1305 1. GN1 boasts improved performance with respect to the current ATLAS flavour
1306 tagging algorithms, with significantly larger background rejection rates for a
1307 given signal efficiency. Alternatively the rejection rates can be kept fixed for a
1308 substantial increase in signal efficiency, in particular at high- p_T .
- 1309 2. The same network architecture can be easily optimised for a wider variety of
1310 use cases (e.g. c -jet tagging and high- p_T jet tagging) since there are no low-level
1311 algorithms to retune.
- 1312 3. There are fewer algorithms to maintain.
- 1313 4. Alongside the network's prediction of the jet flavour, the auxiliary vertex and
1314 track origin predictions provide more information on why a jet was (mis)tagged
1315 or not. This information can also have uses in other applications, for instance
1316 to explicitly reconstruct displaced decay vertices or to remove fake tracks.¹

¹A fake track is defined as a track with a truth-matching probability less than 0.5, where the truth-matching probability is defined in Ref. [55].

6.2 Graph Neural Network Theory

Graph neural networks are a more sophisticated neural network model (see Section 5.1.1) that are designed to operate on graph structured data. A brief introduction to GNNs is provided this section following the formalism in Ref. [113].

A graph \mathcal{G} consists of a set of N^n nodes $\mathcal{N} = \{h_i\}_{i=1:N^n}$ (also called *vertices*), a set of N^e edges $\mathcal{E} = \{e_i\}_{i=1:N^e}$, and a global representation u . Each node represents a individual object, and edges are directed connections between two nodes, called the *sender* and *receiver* nodes. The connectivity of the graph therefore encodes information about the relationships between objects that exist in the graph.

A single graph network layer consists of three separate update functions, one for each of the nodes, edges, and global graph representation, and three aggregation functions. The update functions are typically each implemented as a dense feedforward neural network (as described in Section 5.1.1). The edges e_i are updated by a edge network ϕ^e as in

$$e'_i = \phi^e(e_i, h_s, h_r, u), \quad (6.1)$$

where h_s and h_r are the sender and receiver nodes respectively. The nodes are updated with a node network ϕ^h as in

$$h'_i = \phi^h(\bar{e}'_i, h_i, u), \quad (6.2)$$

where $\bar{e}'_i = \rho^{e \rightarrow h}(E'_i)$, and E'_i is the set of sender nodes for receiver node h_i . $\rho^{e \rightarrow h}$ is referred to as the edge aggregation function. The global representation is updated using the global network ϕ^u as in

$$u' = \phi^u(\bar{e}', \bar{h}', u), \quad (6.3)$$

where \bar{e}' is the aggregation $\rho^{e \rightarrow u}$ over all updated edges e'_i and \bar{h}' is the aggregation $\rho^{e \rightarrow u}$ over all updated nodes h'_i .

The graph network layer performs a graph convolution, in an analogous way to a convolutional neural network operating on a grid of pixels. The above description is general, and not all concrete implementations of GNNs need implement every aspect.

1341 For example, the global graph representation need not be present, and it is also
 1342 possible that no dedicated edge features are present. In such cases the corresponding
 1343 update and aggregation functions are not needed. Fig. 6.2 shows two possible graph
 1344 network update layers.

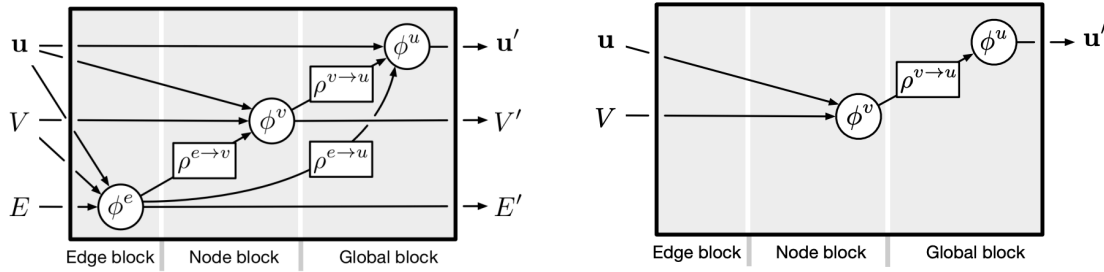


Figure 6.2: The flow of information through a graph neural network layer for (left) a full implementation of the layer and (right) a deep sets model [114]. Reproduced from Ref. [113].

1345 The layer used in the GN1 model is specified in more detail in Section 6.4.3.

1346 6.3 Experimental Setup

1347 6.3.1 Datasets

1348 Datasets used to train the GN1 tagger are the same as described in Section 5.3.1.

1349 The training dataset contains 30 million jets, 60% of which are $t\bar{t}$ jets and 40% of
 1350 which are Z' jets. Although DL1r uses 70% $t\bar{t}$ jets and 30% Z' jets, the composition
 1351 of the training samples was found to have a negligible impact on the final performance
 1352 of GN1

1353 In order to evaluate the performance of the model, a statistically independent set of
 1354 500k testing jets from both the $t\bar{t}$ and Z' were used. Before being fed into the model,
 1355 the track- and jet-level inputs were normalised to have a mean of zero and a variance
 1356 of unity.

1357 Jet flavour labels are assigned according to the presence of a truth hadron within
 1358 $\Delta R(\text{hadron}, \text{jet}) < 0.3$ of the jet axis. If a b -hadron is found the jet is labelled a b -jet.
 1359 In the absence of a b -hadron, if a c -hadron is found the jet is called a c -jet. If no

1360 b - or c -hadrons are found, but a τ is found in the jet, it is labelled as a τ -jet, else
1361 it is labelled as a light-jet. Truth labelled b -, c - and light- jets are kinematically
1362 re-sampled in p_T and η to ensure identical distributions in these variables.

1363

6.4 Model Architecture

1364

6.4.1 Model Inputs

1365 As inputs, GN1 is fed two kinematic jet variables and an unordered set of up to 40
1366 tracks which have been associated to the jet. Each track consists of 21 variables. The
1367 kinematic jet variables are the jet transverse momentum and signed pseudorapidity.
1368 The input variables which are provided for each track are listed in Table 6.1. The
1369 track parameters and associated uncertainties, along with detailed hit information,
1370 are used as these variables carry critical information about the jet flavour. If more
1371 than 40 tracks are associated to a given jet, only the first 40 tracks with the largest
1372 transverse IP significance² $s(d_0)$ are fed into the model as inputs.

1373 In cores of high- p_T jets, tracks density is high due to the increased multiplicity and
1374 collimation fo tracks (see Chapter 4). As a result, the separation between tracks can
1375 be of the same order as the active sensor dimensions, resulting in merged clusters
1376 and tracks which share hits [55]. Due to the relatively long lifetimes of b -hadrons
1377 and c -hadrons, which can traverse several layers of the ID before decaying and have
1378 highly collimated decay products, the presence of shared or missing hits is a critical
1379 signature of heavy flavour jets.

1380 Dependence of the model on the absolute value of the azimuthal jet angle ϕ is
1381 explicitly removed by providing only the azimuthal angle of tracks relative to the jet
1382 axis. The track pseudorapidity is also provided relative to the jet axis. The sign of
1383 the jet pseudorapidity is included, but could be removed in the future to also build
1384 in the forward-backwards symmetry present at ATLAS.

1385 Since heavy flavour hadrons can decay semileptonically, the presence of a recon-
1386 structed lepton in the jet carries discriminating information about the jet flavour. To

²Impact parameter significances are defined as the IP divided by its corresponding uncertainty, $s(d_0) = d_0/\sigma(d_0)$ and $s(z_0) = z_0/\sigma(z_0)$. Track IP significances are lifetime signed according to the track's direction with respect to the jet axis and the primary vertex [37].

1387 exploit this, a variant of GN1 called GN1Lep is trained in addition to the baseline
1388 model. The GN1Lep variant is identical to the baseline model, up to the inclusion
1389 an additional track-level input, leptonID, which indicates if the track was used in
1390 the reconstruction of an electron, a muon or neither. The variable is signed by
1391 the charge of the reconstructed lepton. The leptons used in the definition of the
1392 leptonID variable are required to satisfy basic quality requirements. The muons are
1393 required to be combined [115], and the electrons are required to pass the *VeryLoose*
1394 likelihood-based identification working point [116].

1395 The selections applied to the tracks is the same as that used for the fake track
1396 classification MVA described in Chapter 5. The full set of track selections is listed
1397 in Table 5.3. This selection was found to improve the flavour tagging performance
1398 compared to previous tighter selections, whilst ensuring good resolution of tracks
1399 and a low fake rate [55]. However, Section 6.5.8 demonstrates that further relaxation
1400 of the track selection requirements may be warranted.

1401 6.4.2 Auxiliary Training Objectives

1402 In addition to the jet flavour classification, two auxiliary training objectives are
1403 defined. The first auxiliary objective is the prediction of the origin of each track
1404 within the jet, while the second is the prediction of track-pair vertex compatibility.
1405 Each auxiliary training objective comes with a training target which, similar to
1406 the jet flavour label, is a truth labels derived from the simulation. The presence
1407 of the auxiliary training objectives improves the jet classification performance as
1408 demonstrated in Section 6.5.4.

1409 For the track origin prediction objective, each track is labelled with one of the
1410 exclusive categories defined in Table 5.1 after analysing the particle interaction that
1411 led to its formation. Since the presence of different track origins is strongly related to
1412 the flavour of the jet, training GN1 to recognise the origin of the tracks provides an
1413 additional handle on the classification of the jet flavour. This task may also aid the
1414 jet flavour prediction by acting as a form of supervised attention [117] - in detecting
1415 tracks from heavy flavour decays the model may learn to pay more attention to these
1416 tracks.

Jet Input	Description
p_T	Jet transverse momentum
η	Signed jet pseudorapidity
Track Input	Description
q/p	Track charge divided by momentum (measure of curvature)
$d\eta$	Pseudorapidity of the track, relative to the jet η
$d\phi$	Azimuthal angle of the track, relative to the jet ϕ
d_0	Closest distance from the track to the PV in the longitudinal plane
$z_0 \sin \theta$	Closest distance from the track to the PV in the transverse plane
$\sigma(q/p)$	Uncertainty on q/p
$\sigma(\theta)$	Uncertainty on track polar angle θ
$\sigma(\phi)$	Uncertainty on track azimuthal angle ϕ
$s(d_0)$	Lifetime signed transverse IP significance
$s(z_0)$	Lifetime signed longitudinal IP significance
nPixHits	Number of pixel hits
nSCTHits	Number of SCT hits
nIBLHits	Number of IBL hits
nBLHits	Number of B-layer hits
nIBLShared	Number of shared IBL hits
nIBLSplit	Number of split IBL hits
nPixShared	Number of shared pixel hits
nPixSplit	Number of split pixel hits
nSCTShared	Number of shared SCT hits
nPixHoles	Number of pixel holes
nSCTHoles	Number of SCT holes
leptonID	Indicates if track was used to reconstruct an electron or muon

Table 6.1: Input features to the GN1 model. Basic jet kinematics, along with information about the reconstructed track parameters and constituent hits are used. Shared hits, are hits used on multiple tracks which have not been classified as split by the cluster-splitting neural networks [55], while split hits are hits used on multiple tracks which have been identified as merged. A hole is a missing hit, where one is expected, on a layer between two other hits on a track. The track leptonID is an additional input to the GN1Lep model.

1417 The vertexing auxiliary objective makes use of the fact that displaced decays of b -
 1418 and c -hadrons lead to secondary and tertiary vertices inside the jet, as described
 1419 in Section 4.1.1. The presence of displaced secondary vertices is not a completely
 1420 clean signal of a heavy flavour jet, as displaced secondary vertices can also occur in
 1421 light-jets as a result of material interactions and long-lived particle decays (e.g. K_S^0
 1422 and Λ^0). For the auxiliary object, GN1 predicts a binary label for each pair of tracks
 1423 in the jet. The label has a value of 1 if the truth particles associated with the two
 1424 tracks in the pair originated from the same spatial point, and 0 otherwise. To derive
 1425 the corresponding truth labels for training, truth production vertices within 0.1 mm
 1426 are merged, as these are assumed to be unresolvable given the granularity of the ID.
 1427 Track-pairs where one or both of the tracks in the pair have an origin label of either
 1428 Pileup or Fake are given a label of 0. Using the pairwise predictions from the model,
 1429 groups of tracks that have common compatibility can be formed, resulting in the
 1430 finding of vertices. Two existing low-level tagging algorithms, SV1 and JetFitter, are
 1431 currently used to find and reconstruct vertices inside jets and are used as inputs to
 1432 the existing jet flavour tagger DL1r. The addition of this auxiliary training objective
 1433 removes the need for inputs from a dedicated secondary vertexing algorithm.

1434 Both of the auxiliary training objectives described here can be considered as “stepping
 1435 stones” on the way to classifying the flavour of the jet. By requiring the model to
 1436 predict the truth origin of each track and the vertex compatibility of each track-pair,
 1437 the model is guided to learn representations of the jet which are connected to the
 1438 underlying physics and therefore relevant for classifying the jet flavour.

1439 6.4.3 Architecture

1440 As discussed in the previous sections, GN1 is a graph neural network which makes
 1441 use of auxiliary training objectives in order to determine the jet flavour. A coarse
 1442 optimisation of the network architecture hyperparameters (for example number of
 1443 layers and number of neurons per layer) has been carried out in order to maximise
 1444 the flavour tagging performance, but it is likely that further dedicated optimisation
 1445 studies could lead to further performance improvements.

1446 The model architecture builds on a previous implementation of a GNN-based jet
 1447 tagger [110]. The previous approach was comprised of two separate graph neural
 1448 networks with the auxiliary tasks being performed at an intermediate stage after the

1449 first and before the second. This two stage approach was found to be unnecessary and
1450 as such GN1 simplifies the architecture into a single graph neural network with the
1451 auxiliary tasks being performed at the end, alongside the primary jet classification
1452 task. GN1 makes use of a more sophisticated graph neural network layer [118],
1453 which is described in more detail below. The changes significantly improved tagging
1454 performance and also led to a significant reduction in training time.

1455 As inputs, the model takes information about the jet and a number of associated
1456 tracks, as detailed in Section 6.4.1. The jet variables are concatenated with the
1457 variables for each track as shown in Fig. 6.3. The combined jet-track input vectors
1458 are then fed into a per-track initialisation network with three hidden layers, each
1459 containing 64 neurons, and an output layer with a size of 64, as shown in Fig. 6.4. The
1460 track initialisation network is similar to a deep sets model [114], but does not include
1461 a reduction operation (mean or summation) over the output track representations.
1462 The initialisation network allows for initial per-track input processing without the
1463 associated parameter count cost of the graph convolutional layers described below.

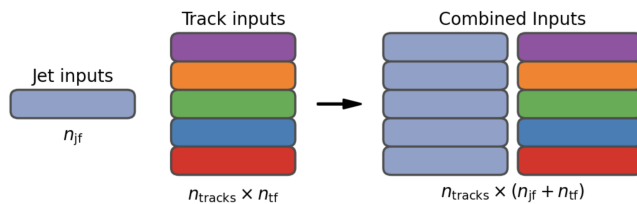


Figure 6.3: The inputs to GN1 are the two jet features ($n_{jf} = 2$), and an array of n_{tracks} , where each track is described by 21 track features ($n_{tf} = 21$). The jet features are copied for each of the tracks, and the combined jet-track vectors of length 23 form the inputs of GN1.

1464 The outputs of the track initialisation network are used to populate the nodes of a
1465 fully connected graph, such that each node in the graph neighbours every other node.
1466 Each node h_i in the graph corresponds to a single track in the jet, and is characterised
1467 by a feature vector, also called a representation. The per-track output representations
1468 from the initialisation networks are used as the initial feature vectors of each node in
1469 the graph. In each layer of the graph network, output node representations h'_i are
1470 computed by aggregating the features of h_i and neighbouring nodes \mathcal{N}_i as described
1471 in Ref. [118]. First, the feature vectors of receiver and sender nodes are fed into two
1472 fully connected linear layers \mathbf{W}_r and \mathbf{W}_s , to produce an updated representation for

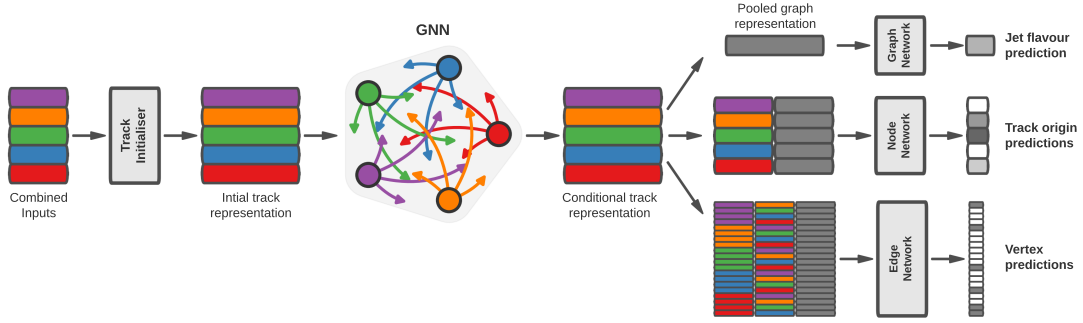


Figure 6.4: The network architecture of GN1. Inputs are fed into a per-track initialisation network, which outputs an initial latent representation of each track. These representations are then used to populate the node features of a fully connected graph network. After the graph network, the resulting node representations are used to predict the jet flavour, the track origins, and the track-pair vertex compatibility.

¹⁴⁷³ each sender and receiver node $\mathbf{W}_r h_i$ and $\mathbf{W}_s h_j$. These updated feature vectors are
¹⁴⁷⁴ used to compute edge scores $e(h_i, h_j)$ for each node pair, as in

$$e(h_i, h_j) = \mathbf{a} \cdot \theta [\mathbf{W}_r h_i + \mathbf{W}_s h_j], \quad (6.4)$$

¹⁴⁷⁵ where, θ is a non-linear activation function, and \mathbf{a} is a learned vector. These edge
¹⁴⁷⁶ scores are then used to calculate attention weights a_{ij} for each pair of nodes using
¹⁴⁷⁷ the softmax function over the edge scores

$$a_{ij} = \text{softmax}_j [e(h_i, h_j)]. \quad (6.5)$$

¹⁴⁷⁸ Finally, the updated representations for the receiver nodes h'_i are computed by taking
¹⁴⁷⁹ the weighted sum over each updated node representation $\mathbf{W}_r h_i$, with weights a_{ij}

$$h'_i = \sigma \left[\sum_{j \in \mathcal{N}_i} a_{ij} \cdot \mathbf{W}_r h_j \right]. \quad (6.6)$$

1480 The set of operations described above constitute a single graph network layer. Three
 1481 such layers are stacked to construct the graph network, representing a balance
 1482 between achieving good performance and avoiding overtraining due to inflation of
 1483 the parameter count of the model. The final output from the graph neural network is
 1484 a set of per-node (i.e. per-track) feature vectors that are conditional representations
 1485 of each track given the other tracks in the jet. In order to perform the jet flavour
 1486 prediction, a flattened global representation of the jet is needed. To produce this, the
 1487 output track representations are combined using a weighted sum, where the weights
 1488 are learned during training and therefore act as a form of single-headed attention
 1489 over the different tracks. The flattened outputs from the sum are then fed into a
 1490 fully connected feedforward neural network with four layers and three outputs, one
 1491 for each jet flavour. Two other separate fully connected feedforward neural networks
 1492 are then used to independently perform the auxiliary classification objectives of GN1.
 1493 Both of the auxiliary classification tasks also take in the global representation of the
 1494 jet as inputs. A summary of the different classification networks used for the various
 1495 training objectives is shown in Table 6.2.

Table 6.2: A summary of GN1’s different classification networks used for the different training objectives. The hidden layers column contains a list specifying the number of neurons in each layer.

Network	Hidden layers	Output size
Node classification network	128, 64, 32	7
Edge classification network	128, 64, 32	1
Graph classification network	128, 64, 32, 16	3

1496 A node classification network predicts the track truth origin as defined in Table 5.1.
 1497 This network takes as inputs the features from a single output node from the graph
 1498 network and the global representation of the jet. The node network has three hidden
 1499 layers containing 128, 64 and 32 neurons respectively, and an output size of seven,
 1500 corresponding to the seven different truth origins defined in Table 5.1.
 1501 An edge classification network is used to predict whether the tracks in the track-
 1502 pair belong to a common vertex. This network takes as inputs the concatenated
 1503 representations from each pair of tracks and the global jet representation. Similar
 1504 to the node network, the edge network has three hidden layers containing 128,

1505 64 and 32 neurons respectively, and a single output, which is used to perform
 1506 binary classification of the track-pair compatibility. The output predictions for the
 1507 two auxiliary networks are used for the auxiliary training objectives discussed in
 1508 Section 6.4.2.

1509 Finally, the graph classification network is used to predict the jet flavour. This
 1510 network takes only the global jet representation as input. The graph classification
 1511 network is comprised of four fully connected hidden layers with 128, 64, 32 and 16
 1512 neurons respectively, and has three outputs corresponding to the b -, c - and light- jet
 1513 classes.

1514 6.4.4 Training

1515 The full GN1 training procedure minimises the total loss function L_{total} , defined
 1516 in Eq. (6.7). This loss is composed of three terms: L_{jet} , the categorical cross
 1517 entropy loss over the different jet flavours; L_{vertex} , the binary track-pair compatibility
 1518 cross entropy loss; and L_{track} , the categorical cross entropy loss for the track origin
 1519 prediction. L_{vertex} is computed by averaging over all intra-jet track-pairs in the batch,
 1520 and L_{track} is computed by averaging over all tracks in the batch.

$$L_{\text{total}} = L_{\text{jet}} + \alpha L_{\text{vertex}} + \beta L_{\text{track}} \quad (6.7)$$

1521 The different losses converge to different values during training, reflecting differences
 1522 in the relative difficulty of the various training objectives. The values of L_{vertex} and
 1523 L_{track} are weighted by $\alpha = 1.5$ and $\beta = 0.5$ respectively to ensure they converge to
 1524 similar values, giving them an equal weighting towards L_{total} . The values of α and β
 1525 are chosen to ensure that L_{jet} converges to a larger value than either L_{vertex} and L_{track} ,
 1526 which reflects the primary importance of the jet classification objective. It was found
 1527 that in practice the overall performance of the model was not sensitive to modest
 1528 changes in the loss weights α and β . Pre-training using L_{total} (i.e. on all tasks) and
 1529 fine tuning on only the jet classification task also did not improve performance versus
 1530 the described standard setup, indicating that the auxiliary tasks are not in direct
 1531 competition with the jet classification task. As there was a large variation in the

relative abundance of tracks of the different origins, the contribution of each origin to L_{track} was weighted by the inverse of the frequency of their occurrence. In vertexing loss L_{vertex} , the class weight for track-pairs where both tracks are from either a b - or c -hadron was increased by a factor of two as compared with other track-pairs, to encourage the network to focus on correctly classifying heavy flavour vertices.

GN1 can be trained with either the node or edge networks (and their corresponding auxiliary tasks), or both, removed, as discussed in Section 6.5.4. In such cases, the corresponding losses L_{vertex} and L_{track} are also removed from the calculation of the overall loss L_{total} . The performance of the resulting models provides a useful indication of the benefit of including the auxiliary tasks to the primary jet classification objective.

GN1 is trained for 100 epochs on 4 NVIDIA V100 GPUs. Each epoch takes approximately 25 mins to complete over the training sample of 30 million jets described in Section 6.3.1. The Adam optimiser [119] with an initial learning rate of 1e–3, and a batch size of 4000 jets (spread across the 4 GPUs) was used. Typically the validation loss, calculated on 500k jets, became stable after around 60 epochs. The epoch that minimized the validation loss was used for evaluation. GN1 has been integrated into the ATLAS software [52] using ONNX [120]. The test sample jet flavour predictions scores are computed using the ATLAS software stack as a verification of this process.

6.5 Results

The GN1 tagger is evaluated both as a b -tagging and c -tagging algorithm in Section 6.5.1 and Section 6.5.2 respectively. Evaluation is performed separately on both jets in the $t\bar{t}$ sample with $20 < p_{\text{T}} < 250 \text{ GeV}$ and jets in the Z' sample with $250 < p_{\text{T}} < 5000 \text{ GeV}$. The performance of the model is compared to the DL1r tagger [107, 108], which has been retrained on 75 million jets from the same samples as GN1. The input RNNIP tagger [112] to DL1r has not been retrained. As discussed, each tagger predicts the probability that a jet belongs to the b -, c - and light- classes. To use the model for b -tagging, these probabilities are combined into a single score D_b , which is defined as

$$D_b = \log \frac{p_b}{(1 - f_c)p_l + f_c p_c}, \quad (6.8)$$

1561 where f_c is a free parameter that determines the relative weight of p_c to p_l in the
 1562 score D_b , controlling the trade-off between c - and light-jet rejection performance.
 1563 The choice of f_c is arbitrary, with the different optimised values reflecting the relative
 1564 c - versus light-jet rejection performance of the various taggers. This parameter is
 1565 set to a value of $f_c = 0.018$ for the DL1r model, obtained through an optimisation
 1566 procedure designed to maximise the c - and light-jet rejection of DL1r described in
 1567 Ref. [107]. Based on a similar optimisation procedure, a value of $f_c = 0.05$ is used
 1568 for the GN1 models. A fixed-cut working point (WP) defines the corresponding
 1569 selection applied to the tagging discriminant D_b in order to achieve a given efficiency
 1570 on the inclusive $t\bar{t}$ sample.

1571 The technical implementation of GN1 in the ATLAS software stack requires any jet
 1572 with zero or one associated tracks to be classified as a light-jet. The impact of this
 1573 on the tagging performance of GN1 was found to be negligible, with 0.12% of b -jets
 1574 in the $t\bar{t}$ sample and 0.02% of b -jets in the Z' sample affected. Of those, 89% of the
 1575 b -jets in the $t\bar{t}$ sample and 98% of the b -jets in the Z' sample are also classified as
 1576 light-jets by DL1r at the 70% $t\bar{t}$ WP.

1577 A comparison of the b -tagging discriminant D_b between DL1r and GN1 is shown in
 1578 Fig. 6.5. The shapes of the D_b distributions are generally similar for b -, c - and light-
 1579 jets between both models, however, GN1 shifts the b -jet distribution to higher values
 1580 of D_b in the regions with the greatest discrimination. The GN1 c -jet distribution is
 1581 also shifted to lower values of D_b when compared with DL1r, enhancing the separation
 1582 and indicating that GN1 is improving c -jet rejection when compared with DL1r.

1583 6.5.1 b -tagging Performance

1584 The performance of b -tagging algorithms is quantified by their ability to reject c -
 1585 and light-jets for a given b -jet selection efficiency, or working point (WP). In order
 1586 to compare the b -tagging performance of the different taggers for the b -jet tagging
 1587 efficiencies in the range typically used by analyses, the corresponding c - and light-jet

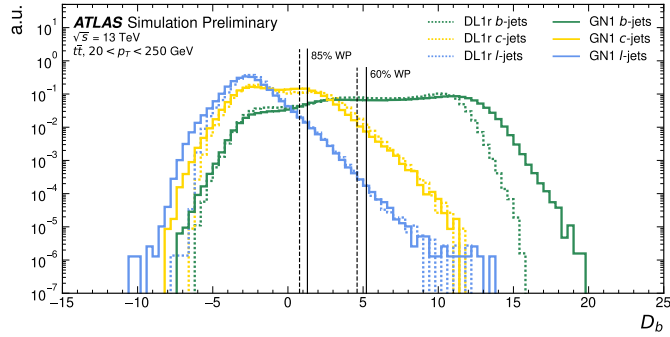


Figure 6.5: Comparison between the DL1r and GN1 b -tagging discriminant D_b for jets in the $t\bar{t}$ sample. The 85% WP and the 60% WP are marked by the solid (dashed) lines for GN1 (DL1r), representing respectively the loosest and tightest WPs used by analyses. A value of $f_c = 0.018$ is used in the calculation of D_b for DL1r and $f_c = 0.05$ is used for GN1. The distributions of the different jet flavours have been normalised to unity area.

rejection rates are displayed in Figs. 6.6 and 6.7 for jets in the $t\bar{t}$ and Z' samples respectively. Four standard WPs are defined with b -jet tagging efficiencies of 60%, 70%, 77% and 85% respectively. These WPs are commonly used by physics analyses depending on their specific signal and background requirements. The WPs are defined based on jets in the $t\bar{t}$ sample only. Due to the much higher jet p_T range in the Z' sample, and the increased difficulty in tagging jets at high- p_T (see Chapter 4), the b -jet tagging efficiencies for jets in the Z' sample are lower than the corresponding WPs calculated in the $t\bar{t}$ sample. For instance the WP cut value compute to provide a 70% b -jet tagging efficiency on the $t\bar{t}$ sample results in a b -jet tagging efficiency of just $\sim 30\%$ on the Z' sample. In order to account for this, the range of b -jet tagging efficiencies displayed for plots showing the performance for jets in the Z' sample (for example Fig. 6.7) is chosen to span the lower efficiencies achieved in the Z' sample at high- p_T .

For jets in the $t\bar{t}$ sample with $20 < p_T < 250$ GeV, GN1 demonstrates considerably better c - and light-jet rejection when compared with DL1r across the full range of b -jet tagging efficiencies studied. The relative improvement is strongly dependent on the b -jet tagging efficiency under study. The largest improvements are found at lower b -jet tagging efficiencies. At a b -jet tagging efficiency of 70%, the c -rejection improves by a factor of ~ 2.1 while the light-jet rejection improves by a factor of ~ 1.8 with respect to DL1r. For high- p_T jets in the Z' sample with $250 < p_T < 5000$ GeV, GN1 also brings a significant performance improvement with respect to DL1r across the

range of b -jet tagging efficiencies studied. Again, the largest relative improvement in performance comes at the lower b -jet tagging efficiencies. At a b -jet efficiency of 30%, GN1 improves the c -rejection with respect to DL1r by a factor of ~ 2.8 and the light-jet rejection by a factor of ~ 6 . The performance comparison at lower b -jet tagging efficiencies is made more difficult due to the increased statistical uncertainties which result from the high rejection of background. It is estimated that for a b -jet tagging efficiency of 70% in the $t\bar{t}$ sample, $\sim 5\%$ ($\sim 30\%$) of the relative improvement in the c -jet (light-jet) rejection comes from loosening the track selection and for a b -jet tagging efficiency of 30% in the Z' the corresponding number is $\sim 10\%$ for both c -jets and light-jets. Given that GN1 exploits the low-level detector information in a more complete and sophisticated way than DL1r, further studies are needed to confirm that the performance gain observed in these simulated samples is also observed in experimental data.

The GN1Lep variant of GN1 demonstrates further improved performance with respect to the baseline model. This demonstrates the additional jet flavour discrimination power provided by the leptonID track input. For jets in the $t\bar{t}$ sample, the relative c -rejection improvement with respect to DL1r at the 70% b -jet WP increases from a factor of ~ 2.1 for GN1 to a factor of ~ 2.8 for GN1Lep. The improvement in light-jet rejection also increases from a factor of ~ 1.8 to ~ 2.5 at the same WP. For jets in the Z' sample, the relative c -rejection (light-jet rejection) improvement with respect to DL1r increases from a factor of ~ 2.8 to ~ 3 (~ 6 to ~ 7.5) at a b -jet tagging efficiency of 30%. As shown in Fig. 6.8, the greatest improvement of GN1Lep over GN1 is seen at lower transverse momenta.

In general, the performance of all the taggers is strongly dependent on the jet p_T . This is due to the increased multiplicity and collimation of tracks, and the displaced decays that result from within the heavy flavour jets. These factors are described in more detail in Chapter 4. Together, they contribute to a reduced reconstruction efficiency for heavy flavour tracks, and a general degradation in quality of tracks inside the core of a jet, which in turn reduces the jet tagging performance.

In order to study how the tagging performance changes as a function of the jet p_T , the b -jet tagging efficiency as a function of p_T for a fixed light-jet rejection of 100 in each bin is shown in Fig. 6.8. For jets in the $t\bar{t}$ sample, at a fixed light-jet rejection of 100, GN1 improves the b -jet tagging efficiency by approximately 4% across all the jet p_T bins. Meanwhile, GN1Lep again demonstrates improved performance with

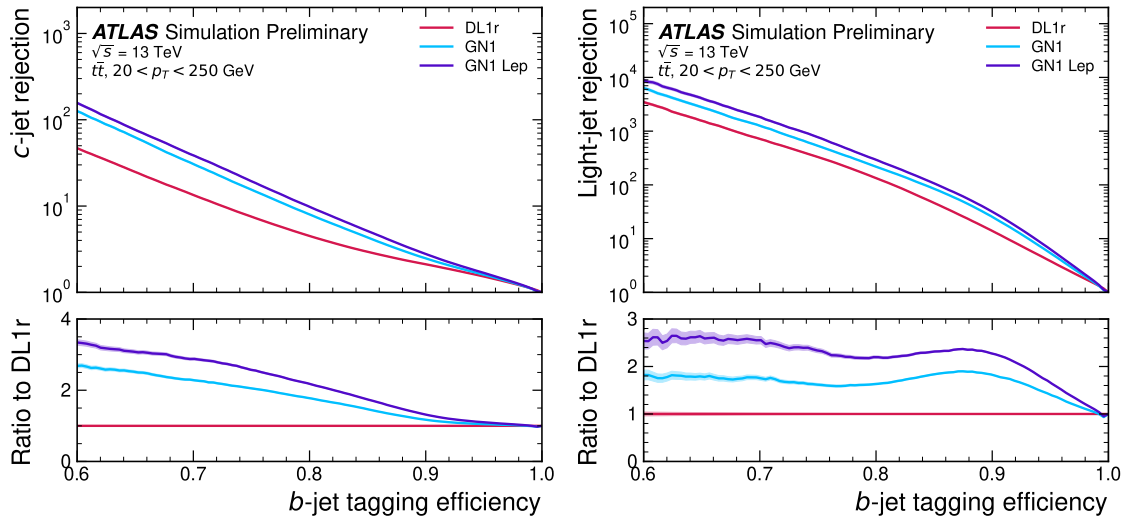


Figure 6.6: The c -jet (left) and light-jet (right) rejections as a function of the b -jet tagging efficiency for jets in the $t\bar{t}$ sample with $20 < p_T < 250 \text{ GeV}$. The ratio with respect to the performance of the DL1r algorithm is shown in the bottom panels. A value of $f_c = 0.018$ is used in the calculation of D_b for DL1r and $f_c = 0.05$ is used for GN1 and GN1Lep. Binomial error bands are denoted by the shaded regions. At b -jet tagging efficiencies less than $\sim 75\%$, the light-jet rejection becomes so large that the effect of the low number of jets is visible. The lower x -axis range is chosen to display the b -jet tagging efficiencies usually probed in these regions of phase space.

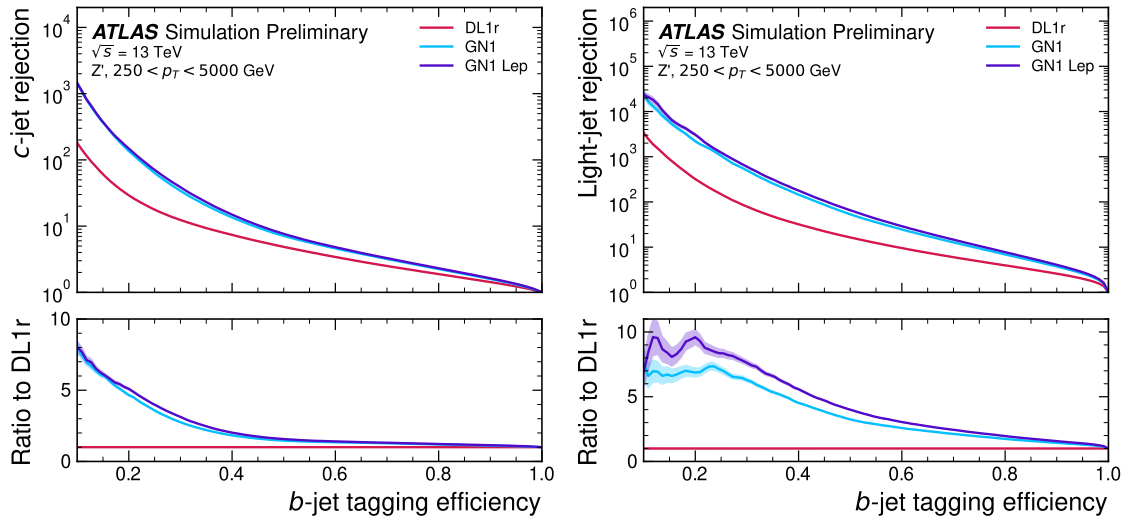


Figure 6.7: The c -jet (left) and light-jet (right) rejections as a function of the b -jet tagging efficiency for jets in the Z' sample with $250 < p_T < 5000 \text{ GeV}$. The ratio with respect to the performance of the DL1r algorithm is shown in the bottom panels. A value of $f_c = 0.018$ is used in the calculation of D_b for DL1r and $f_c = 0.05$ is used for GN1 and GN1Lep. Binomial error bands are denoted by the shaded regions. At b -jet tagging efficiencies less than $\sim 20\%$, the light-jet rejection becomes so large that the effect of the low number of jets is visible. The lower x -axis range is chosen to display the b -jet tagging efficiencies usually probed in these regions of phase space.

respect to GN1, in particular at lower p_T . The relative increase in the b -jet tagging efficiency increases from 4% to 8% with respect to DL1r. For jets in the Z' sample, GN1 again outperforms DL1r across the entire jet p_T range studied. The largest relative improvement in performance is found at the highest transverse momenta of jet $p_T > 2$ TeV, and corresponds to an approximate factor of 2 improvement in efficiency with respect to DL1r.

The performance of the model was also evaluated as a function of the average number of pileup interactions in the event. No significant dependence of the tagging performance was observed.

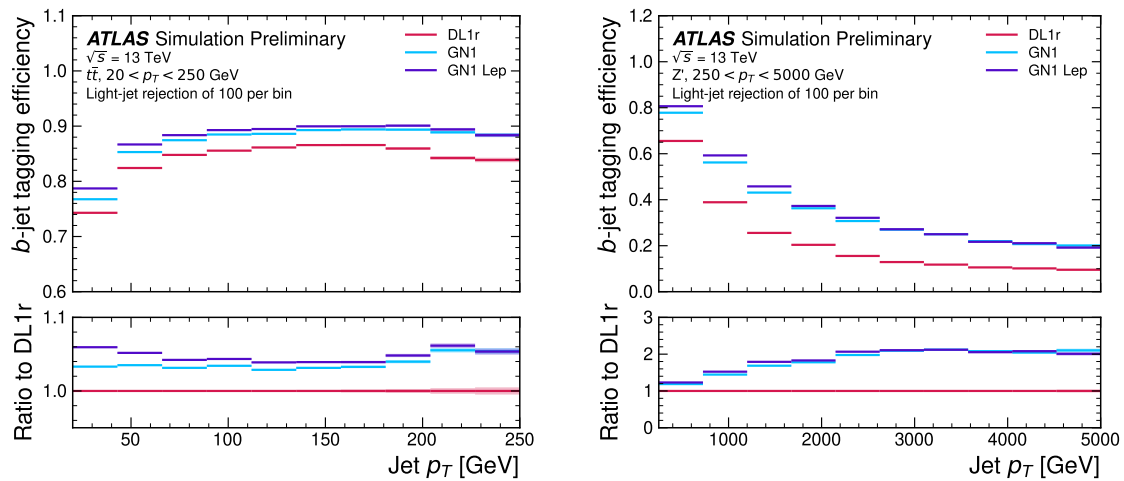


Figure 6.8: The b -jet tagging efficiency for jets in the $t\bar{t}$ sample (left) and jets in the Z' sample (right) as a function of jet p_T with a fixed light-jet rejection of 100 in each bin. A value of $f_c = 0.018$ is used in the calculation of D_b for DL1r and $f_c = 0.05$ is used for GN1 and GN1Lep. GN1 demonstrates improved performance with respect to DL1r accross the p_T range shown. Binomial error bands are denoted by the shaded regions.

6.5.2 c -tagging Performance

As discussed previously, GN1 does not rely on any inputs from manually optimised low-level tagging algorithms. Since these algorithms were originally designed and tuned with the aim of b -tagging, and not c -tagging, the low level tagging algorithms may perform suboptimally for c -tagging purposes. The tagging of c -jets therefore presents a compelling use case for GN1. As each of the the models is trained with three output classes, using it as a c -tagging algorithm is trivially analogous to the

1659 approach used for b -tagging. The model output probabilities are combined into a
1660 single score D_c , which is defined similarly to Eq. (6.8) as

$$D_c = \log \frac{p_c}{(1 - f_b)p_l + f_b p_b}. \quad (6.9)$$

1661 A value of $f_b = 0.2$ is used for all models, based on the same optimisation procedure
1662 that was used for the b -tagging use case. Similar to Section 6.5.1, the different
1663 taggers are compared to one another by scanning through a range of c -jet tagging
1664 efficiencies and plotting the corresponding b - and light-jet rejection rates. As in
1665 Section 6.5.1, the WPs are defined using jets in the $t\bar{t}$ sample. Standard c -jet tagging
1666 efficiency WPs used by physics analyses are significantly lower than the b -tagging
1667 WPs in order to maintain reasonable b - and light-jet rejection rates. This is reflected
1668 in the range of c -jet tagging efficiencies used in c -tagging plots such as Figs. 6.9
1669 and 6.10. Fig. 6.9 displays the c -tagging performance of the models on the jets in
1670 the $t\bar{t}$ sample. GN1 is shown to perform significantly better than DL1r. Similar to
1671 the b -tagging case, the b - and light-jet rejection improve most at lower c -jet tagging
1672 efficiencies, with both background rejections increasing by a factor of 2 with respect
1673 to DL1r at a c -jet tagging efficiency of 25%. GN1Lep again outperforms GN1, though
1674 the improvements with respect to the baseline model are more modest, with the
1675 b -rejection (light-jet rejection) relative improvement increasing from a factor of 2 to
1676 2.1 (2 to 2.3) at the 25% c -jet WP. Fig. 6.10 shows the c -tagging performance on the
1677 jets in the Z' sample with $250 < p_T < 5000$ GeV. Both GN1 and GN1Lep perform
1678 similarly, improving the b -rejection by 60% and the light-jet rejection by a factor of
1679 2 at the 25% c -jet WP.

1680 6.5.3 Jet Display Diagrams

1681 The auxiliary training objectives of GN1 allow for improved model interpretability,
1682 which is especially important for a monolithic approach as the low level taggers,
1683 which provide useful physical insight, are no longer present. Figs. 6.11 and 6.12
1684 show a comparison of the true origin and vertexing information compared with
1685 the predicted values from GN1, SV1 and JetFitter. Such comparisons can be used

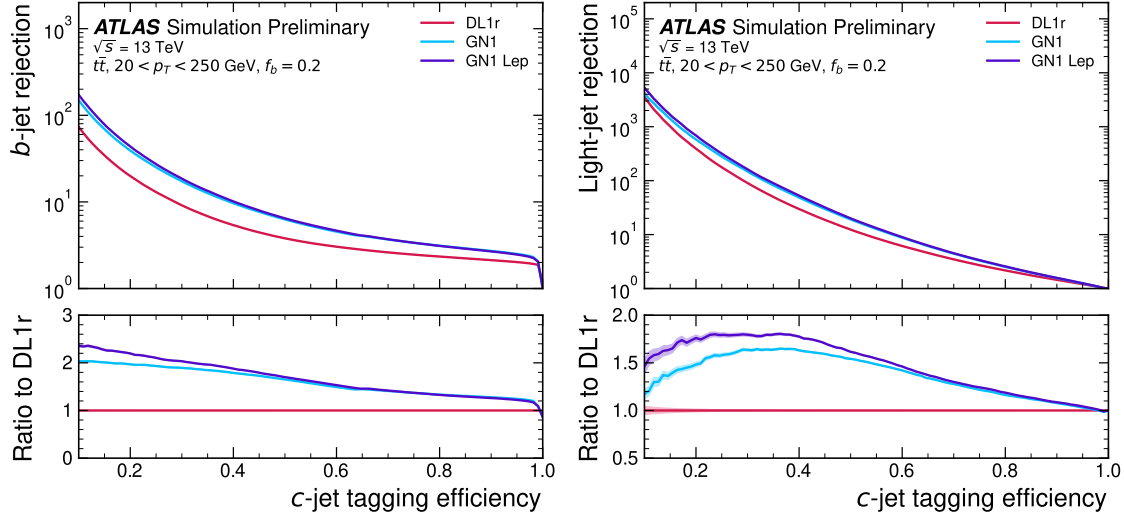


Figure 6.9: The b -jet (left) and light-jet (right) rejections as a function of the c -jet tagging efficiency for $t\bar{t}$ jets with $20 < p_T < 250$ GeV. The ratio to the performance of the DL1r algorithm is shown in the bottom panels. Binomial error bands are denoted by the shaded regions. At c -jet tagging efficiencies than $\sim 25\%$, the light-jet rejection becomes so large that the effect of the low number of jets is visible. The lower x -axis range is chosen to display the c -jet tagging efficiencies usually probed in these regions of phase space.

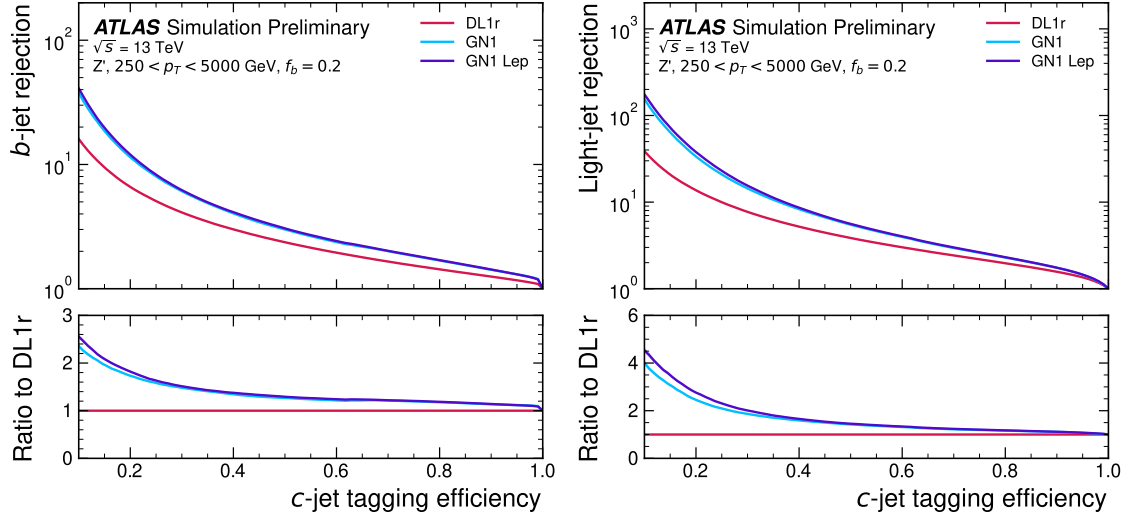


Figure 6.10: The b -jet (left) and light-jet (right) rejections as a function of the c -jet tagging efficiency for Z' jets with $250 < p_T < 5000$ GeV. The ratio to the performance of the DL1r algorithm is shown in the bottom panels. Binomial error bands are denoted by the shaded regions. The lower x -axis range is chosen to display the c -jet tagging efficiencies usually probed in these regions of phase space.

1686 to provide an indication that GN1 recovers the intended representation of the jet
1687 structure, and may also help to identify limitations of the model.

1688 The diagrams show the truth (left) and predicted (right) structure of a b -jet. The
1689 shaded black boxes show the groupings of tracks into different vertices. In Fig. 6.11,
1690 GN1 correctly groups the three primary tracks as having come from the primary
1691 vertex. The b -hadron and $b \rightarrow c$ -hadron decay vertices are also correctly predicted,
1692 and the origin of the tracks in each is correct. There is a single OtherSecondary track
1693 which GN1 incorrectly predicts as having come pileup. Meanwhile SV1 (by design)
1694 merges the two heavy flavour decay vertices, but incorrectly includes a track from
1695 the primary vertex. JetFitter reconstructs two vertices, one which is a combination
1696 of two tracks from the different truth vertices and two other single track vertices in
1697 each of the heavy flavour vertices. GN1 also predicts the flavour of the jet with a
1698 high degree of certainty.

1699 Similarly, Fig. 6.11 shows that, at least in some cases, GN1 is able to accurately
1700 predict the origin and vertex information of tracks inside a jet. The pileup tracks
1701 and primary vertex tracks are correctly identified, and the heavy flavour decay tracks
1702 are also correctly identified with the exception of one of the b -hadron decay tracks.
1703 Again, SV1 is overly aggressive by merging the two heavy flavour decay vertices
1704 along with a track from pileup, while JetFitter shows signs of being underconstrained
1705 by reconstructing two single track vertices, one with a pileup track and one with a
1706 track from a $b \rightarrow c$ -hadron decay.

1707 6.5.4 Ablations

1708 Ablation studies (the removal of certain components of a given model in order to
1709 study the impact of that component) are carried out to determine the
1710 importance of the auxiliary training objectives of GN1 to the overall performance.
1711 The “GN1 No Aux” variant retains the primary jet classification objective, but
1712 removes both track classification and vertexing auxiliary objectives (see Section 6.4.2)
1713 and correspondingly only minimises the jet classification loss. The “GN1 TC” variant
1714 includes track classification objective but not the vertexing objective. Finally, the
1715 “GN1 Vert” includes the vertexing objective, but not the track classification objective.

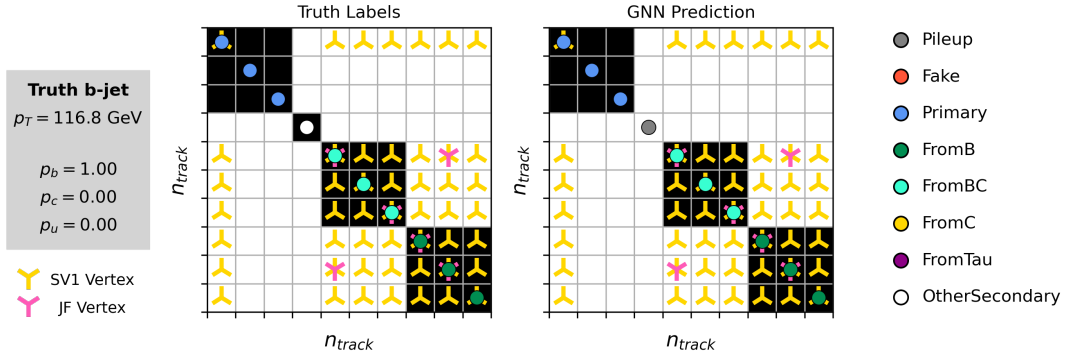


Figure 6.11: A schematic showing the truth track origin and vertex information (left) compared with the predictions from GN1 (right). Vertices reconstructed by SV1 and JetFitter are also marked. Class probabilities p_b , p_c and p_u are rounded to three significant figures. GN1 improves over SV1 and JetFitter by successfully determining the origins and vertex compatibility of all the tracks in the jet with the exception of the truth OtherSecondary track, which is misidentified as pileup.

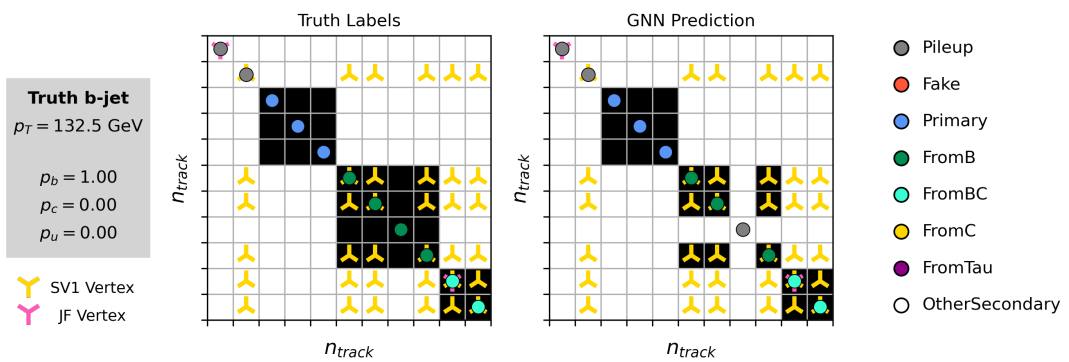


Figure 6.12: A schematic showing the truth track origin and vertex information (left) compared with the predictions from GN1 (right). Vertices reconstructed by SV1 and JetFitter are also marked. Class probabilities p_b , p_c and p_u are rounded to three significant figures.

1716 For jets in both the $t\bar{t}$ and Z' samples, a general trend is observed that the models
1717 trained without one or both of the auxiliary objectives results in significantly reduced
1718 c - and light-jet rejection when compared with the baseline GN1 model. This result
1719 is shown clearly in Figs. 6.13 and 6.14. For jets in the $t\bar{t}$ sample, the performance
1720 of GN1 No Aux is similar to DL1r, while GN1 TC and GN1 Vert perform similarly
1721 to each other with improvements in the c -rejection of 80% and improvements in
1722 the light-jet rejection of 75% at a b -jet tagging efficiency of 60%. For jets in the Z'
1723 sample meanwhile, the GN1 No Aux model already shows a clear improvement in c -
1724 and light-jet rejection when compared with DL1r at lower b -jet tagging efficiencies.
1725 Similar to jets in the $t\bar{t}$ sample, GN1 TC and GN1 Vert perform similarly, and bring
1726 large gains in background rejection when compared with GN1 No Aux, but the
1727 combination of both auxiliary objectives yields the best performance.

1728 It is notable that the GN1 No Aux model matches or exceeds the performance of
1729 DL1r without the need for inputs from the low-level algorithms. This indicates that
1730 the performance improvements enabled by the improved neural network architecture
1731 used in GN1 appear to be able to compensate for the removal of the low-level
1732 algorithm inputs. The GN1 TC and GN1 Vert variants each similarly outperform
1733 DL1r, demonstrating that both contribute to the overall high performance of the
1734 baseline model. The overall best performing model is the full version of GN1 trained
1735 with both auxiliary objective, demonstrating that the both auxiliary objectives are
1736 complementary.

1737 6.5.5 Inclusion of Low-Level Vertexing Algorithms

1738 As already mentioned, GN1 does not include any inputs from the low-level tagging
1739 algorithms, including the vertexing algorithms SV1 and JetFitter [59]. Since these
1740 algorithms are known to play a key role in contributing to the performance of DL1r, it
1741 was necessary to study whether their inclusion in GN1 resulted in further performance
1742 improvements. In a dedicated training of GN1 the SV1 and JetFitter tagger outputs
1743 were added to the GN1 jet classification network as an input, similar to how they
1744 are used in DL1r. These outputs include information on the reconstructed vertices,
1745 including the number of vertices, and the mass, displacement, and other properties of
1746 the highest ranking reconstructed vertex. In addition, the index of the reconstructed
1747 SV1 or JetFitter vertices were included as two track-level inputs to GN1. These

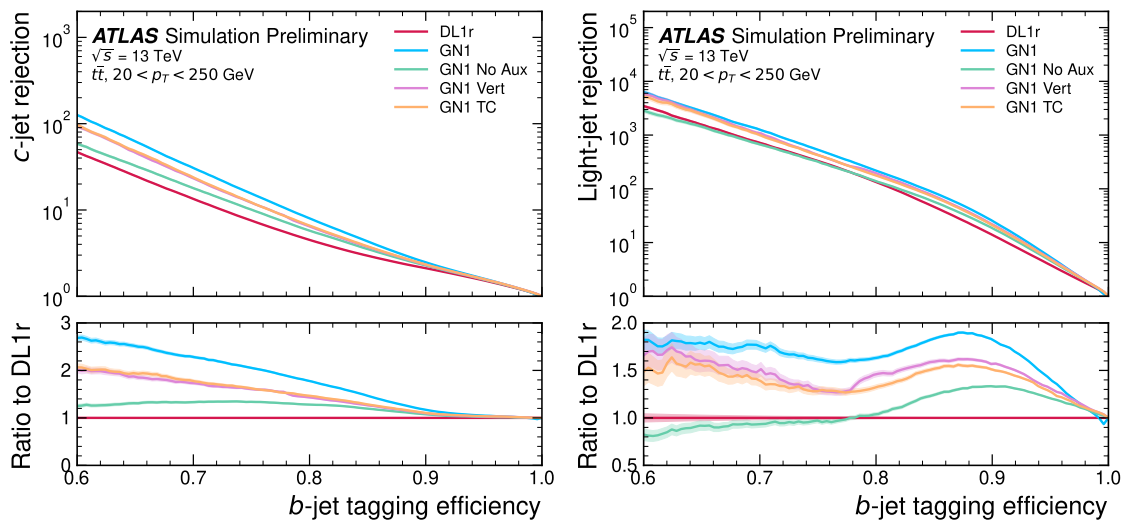


Figure 6.13: The c -jet (left) and light-jet (right) rejections as a function of the b -jet tagging efficiency for $t\bar{t}$ jets with $20 < p_T < 250$ GeV, for the nominal GN1, in addition to configurations where no (GN1 No Aux), only the track classification (GN1 TC) or only the vertexing (GN1 Vert) auxiliary objectives are deployed. The ratio to the performance of the DL1r algorithm is shown in the bottom panels. A value of $f_c = 0.018$ is used in the calculation of D_b for DL1r and $f_c = 0.05$ is used for GN1. Binomial error bands are denoted by the shaded regions. At b -jet tagging efficiencies less than $\sim 65\%$, the light-jet rejection become so large that the effect of the low number of jets are visible. The lower x -axis range is chosen to display the b -jet tagging efficiencies usually probed in these regions.

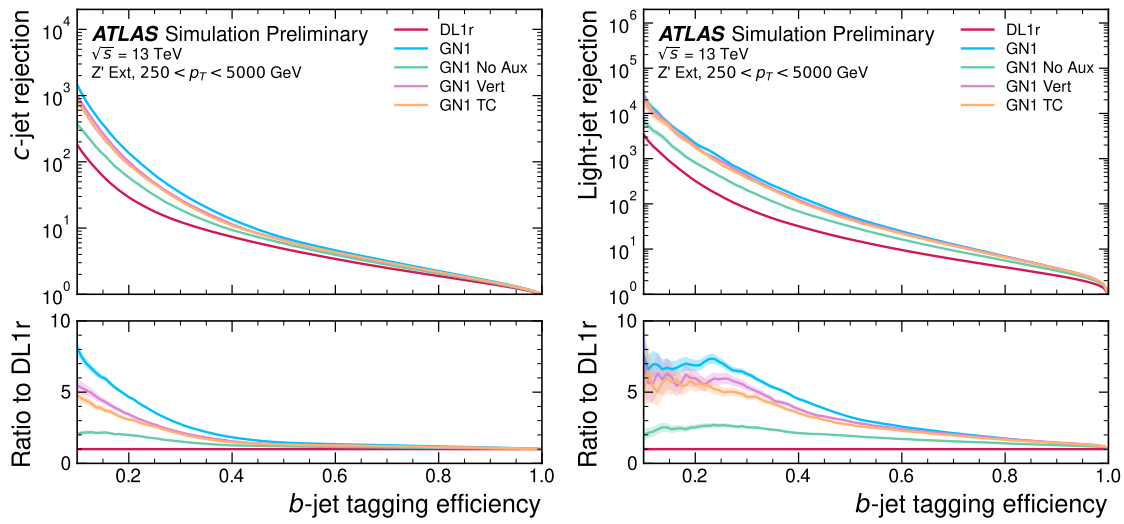


Figure 6.14: The c -jet (left) and light-jet (right) rejections as a function of the b -jet tagging efficiency for Z' jets with $250 < p_T < 5000$ GeV, for the nominal GN1, in addition to configurations where no (GN1 No Aux), only the track classification (GN1 TC) or only the vertexing (GN1 Vert) auxiliary objectives are deployed. The ratio to the performance of the DL1r algorithm is shown in the bottom panels. A value of $f_c = 0.018$ is used in the calculation of D_b for DL1r and $f_c = 0.05$ is used for GN1. Binomial error bands are denoted by the shaded regions. At b -jet tagging efficiencies less than $\sim 25\%$, the light-jet rejection become so large that the effect of the low number of jets are visible. The lower x -axis range is chosen to display the b -jet tagging efficiencies usually probed in these regions.

1748 indices were also used to construct an edge feature for the edge classification network,
1749 which was given a value of one if the track-pair were from a common reconstructed
1750 V1 or JetFitter vertex, and zero otherwise. The jet classification performance of this
1751 GN1 model was not significantly different to the baseline model, and in some cases
1752 the performance was slightly reduced. As GN1 does not benefit from the inclusion
1753 of information from SV1 and JetFitter it can function as a highly performant
1754 standalone tagger that does not require (beyond retraining) any manual optimisation
1755 to achieve good performance in a wide range of phase spaces. A dedicated look at
1756 the vertexing performance of GN1 with some comparisons to SV1 and JetFitter is
1757 found in Section 6.5.6

1758 6.5.6 Vertexing Performance

1759 From the track-pair vertex prediction described in Section 6.4.2, tracks can be
1760 partitioned into compatible groups representing vertices (see [110]). As such, GN1
1761 is able to be used to perform vertex “finding”, but not vertex “fitting”, i.e. the
1762 reconstruction of a vertex’s properties, which currently still requires the use of a
1763 dedicated vertex fitter. In order to study the performance of the different vertexing
1764 tools inside b -jets, the truth vertex label of the tracks, discussed in Section 6.4.2, are
1765 used. To estimate the efficiency with which GN1 manages to find vertices inclusively,
1766 vertices from GN1 containing tracks identified as coming from a b -hadron are merged
1767 together and compared to the inclusive truth decay vertices that result from a
1768 b -hadron decay (where if there are multiple distinct truth vertices from a b -hadron
1769 decay they are also merged together). Vertices are compared with the target truth
1770 vertex and the number of correctly and incorrectly assigned tracks is computed.
1771 Since secondary vertex information is only recovered for reconstructed tracks, an
1772 efficiency of 100% here denotes that all possible secondary vertices are recovered
1773 given the limited track reconstruction efficiency. A vertex is considered matched if
1774 it contains at least 65% of the tracks in the corresponding truth vertex, and has a
1775 purity of at least 50%. GN1 manages to achieve an inclusive reconstruction efficiency
1776 in b -jets of $\sim 80\%$, demonstrating that it effectively manages to identify the displaced
1777 vertices from b -hadron decays.

1778 In order to study the performance of the different vertexing tools inside b -jets, the
1779 truth vertex label of the tracks, discussed in Section 6.4.2, is used. The reconstructed

1780 vertices from GN1, SV1 and JetFitter are compared to the target truth vertices in
1781 order to calculate the efficiencies of the different vertexing tools. Since secondary
1782 vertex information is only recovered for reconstructed tracks, an efficiency of 100%
1783 here denotes that all possible secondary vertices are recovered given the limited track
1784 reconstruction efficiency.

1785 There are several caveats to a comparison of the vertexing tools which are a result
1786 of the different approaches they take to vertexing. SV1 and JetFitter are designed
1787 to only find secondary vertices in the jet, whereas GN1 is also trained to determine
1788 which tracks in the jet belong to the primary vertex (the vertex of the hard scatter
1789 pp interaction). To account for this the GN1 vertex with the largest number of
1790 predicted primary tracks is excluded from the vertex finding efficiency calculation.
1791 While JetFitter and GN1 aim to resolve each displaced vertex inside the jet, such
1792 that secondary vertices from b -hadron decays are found separately to tertiary vertices
1793 from $b \rightarrow c$ decay chains, SV1 by design attempts to find a single inclusive vertex
1794 per jet. This inclusive vertex groups inclusive b -hadron decays. These are tracks
1795 from the b -hadron decay itself (FromB) and tracks from $b \rightarrow c$ decays (FromBC).
1796 In order to fairly compare the performance if the different tools, both the exclusive
1797 and inclusive vertex finding efficiency is studied. For the exclusive vertex finding
1798 case JetFitter and GN1 can be directly compared, while a comparison with SV1 is
1799 not possible due to aforementioned design constraints. The inclusive vertex finding
1800 performance of all three tools can be compared using the procedure outlined below.

1801 The starting point for the secondary vertex finding efficiency in both the exclusive
1802 and inclusive cases is to select truth secondary vertices are those containing only
1803 inclusive b -hadron decays to be considered as initial targets. For exclusive vertex
1804 finding, these truth secondary vertices can be used directly as the denominator for the
1805 efficiency calculation. Meanwhile for the inclusive efficiency all such truth secondary
1806 vertices in the jet are merged into a single inclusive target vertex. Correspondingly,
1807 for the inclusive vertex finding case, the vertices found by JetFitter are merged into
1808 a single vertex, and the vertices found by GN1 with at least one predicted inclusive
1809 b -hadron decay track are also merged similarly. SV1 does not require any vertex
1810 merging.

1811 Next, in both cases for each truth secondary vertex, vertices in the jet found by the
1812 different vertexing tools are compared with the target truth vertex. The number
1813 of correctly and incorrectly assigned tracks is computed. In order to call a vertex

efficient, it is required to contain at least 65% of the tracks in the corresponding truth vertex, and to have a purity of at least 50%. Single track vertices are required to have a purity of 100%. Additionally, for GN1 only, at least one track in the vertex is required to have a predicted heavy flavour origin.

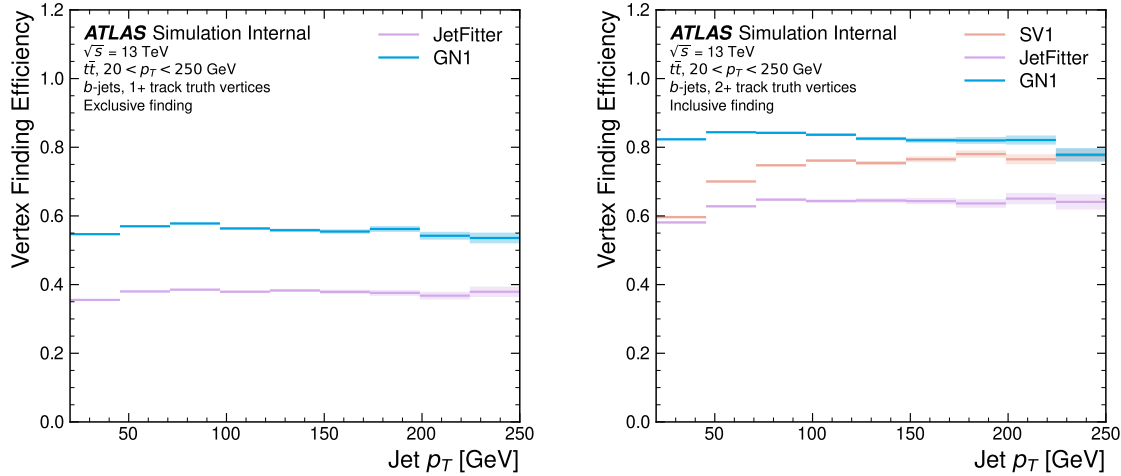


Figure 6.15: Vertex finding efficiency as a function of jet p_T for b -jets in the $t\bar{t}$ sample using the exclusive (left) and inclusive (right) vertex finding approaches. Efficient vertex finding requires the recall of at least 65% of the tracks in the truth vertex, and allows no more than 50% of the tracks to be included incorrectly. Binomial error bands are denoted by the shaded regions.

Vertex finding efficiencies for b -jets in the $t\bar{t}$ sample are displayed as a function of p_T separately for the inclusive and exclusive approaches in Fig. 6.15. For b -jets in the $t\bar{t}$ sample with $20 < p_T < 250$ GeV, the exclusive vertex finding efficiency of JetFitter and GN1 is relatively flat as a function of p_T . Of the truth secondary vertices in this p_T region, JetFitter efficiently finds approximately 40% and GN1 finds approximately 55%. When finding vertices inclusively the vertex finding efficiency is generally higher. An increased dependence on p_T is also visible for JetFitter and SV1. As the jet p_T increases from 20 GeV to 100 GeV, the efficiency of JetFitter increases from 55% to 65%. In the same range, the efficiency of SV1 increases from 55% to 75%. GN1 displays less dependence on p_T than JetFitter and SV1, efficiently finding upwards of 80% of vertices in b -jets in this p_T region. For b -jets with $p_T > 100$ GeV, JetFitter finds approximately 65% of vertices, SV1 finds approximately 75% of vertices, and GN1 finds approximately 80% of vertices.

For b -jets in the Z' sample, the vertex finding efficiency drops steeply with increasing p_T up until $p_T = 3$ TeV. GN1 outperforms SV1 and JetFitter across the p_T spectrum. In the first bin, the efficiency of GN1 is 75%, while the efficiencies of SV1 and JetFitter are around 60%. The efficiency of SV1 drops rapidly to almost zero above 3 TeV, while JetFitter and GN1 retain approximately 30% efficiency. Fig. 6.16 compares the exclusive vertex finding efficiencies of JetFitter and GN1 for multitrack vertices. JetFitter finds 45-50% of vertices in b -jets in the $t\bar{t}$ sample, while GN1 finds 60-65%. For b -jets in the Z' sample, JetFitter finds 35% of vertices in the first bin, dropping to 20% of vertices above 2 TeV. GN1 finds 55% of vertices in the first bin, dropping to 30% above 2 TeV.

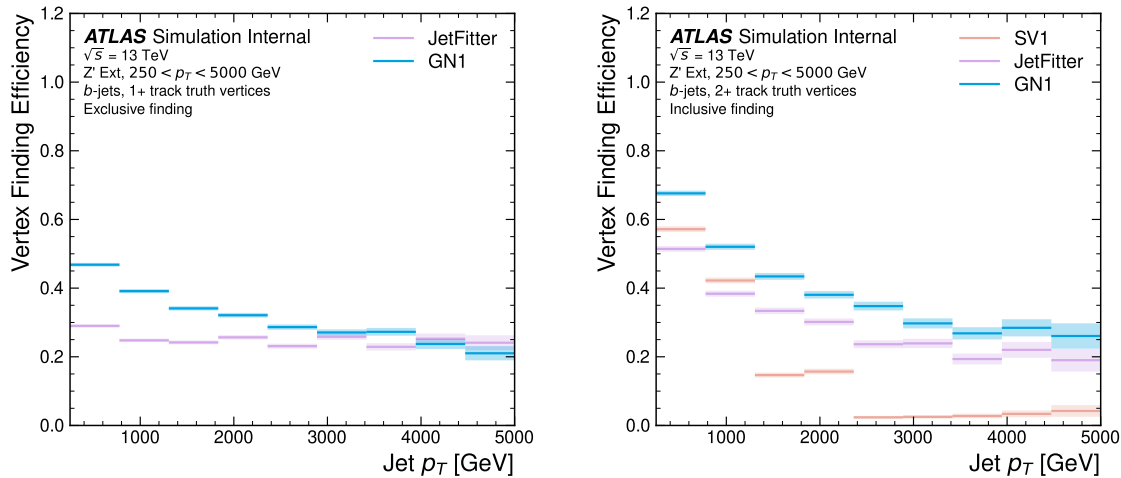


Figure 6.16: Inclusive vertex finding efficiency for multitrack truth vertices in b -jets in the $t\bar{t}$ sample (left) and jets in the Z' sample (right) as a function of jet p_T . Efficient vertex finding requires the recall of at least 65% of the tracks in the truth vertex, and allows no more than 50% of the tracks to be included incorrectly.

6.5.7 Track Classification Performance

One of the two auxiliary training objectives used by GN1 is to predict the truth origin of each track associated to the jet, as discussed in Section 6.4.2. Since the equivalent information is not provided by any of the existing flavour tagging tools, a benchmark model based on a standard multi-class feed-forward classification network is trained on the same tracks used for the baseline GN1 training. The model uses precisely the same concatenated track-and-jet inputs as used by GN1 (see Section 6.4.1),

1848 but processes only a single track at a time, meaning it cannot take into account
1849 the correlations between tracks when determining the track origin. The model is
1850 made up of five densely connected linear layers with 200 neurons in each layer. The
1851 performance of the model was found to be unsensitive to changes in the network
1852 structure.

1853 To measure the track classification performance, the area under the curve (AUC)
1854 of the receiver operating characteristic (ROC) curve is computed for each origin
1855 class, using a one-versus-all classification approach. The AUCs for the different
1856 truth origins are averaged using both an unweighted and a weighted mean. The
1857 unweighted mean treats the performance of each class equally, while the weighted
1858 mean uses as a weight the relative abundance of tracks of each class. Table 6.3
1859 demonstrates clearly that GN1 outperforms the MLP both at $20 < p_T < 250 \text{ GeV}$
1860 for jets in the $t\bar{t}$ sample and at $250 < p_T < 5000 \text{ GeV}$ for jets in the Z' sample. For
1861 example, GN1 can reject 65% of fake tracks in jets in the $t\bar{t}$ sample, while retaining
1862 more than 99% of good tracks (i.e. those tracks which are not fake). The GN1 model
1863 has two advantages over the MLP which can explain the performance improvement.
1864 Firstly, the graph neural network architecture enables the sharing of information
1865 between tracks as discussed in Section 6.4.3. This is likely to be beneficial since the
1866 origins of different tracks within a jet are correlated. Secondly, the jet classification
1867 and vertexing objectives may be complementary to the track classification objective,
1868 and so the track classification performance is improved by the combined training of
1869 complementary objectives.

1870 Fig. 6.17 shows the track origin classification ROC curves for the different track
1871 origins for jets in both the $t\bar{t}$ and Z' samples. In order to improve visual readability
1872 of the plot, the curves for the heavy flavour truth origins (FromB, FromBC and
1873 FromC) have been combined (weighted by their relative abundance), as have the
1874 Primary and OtherSecondary origins. In jets in both the $t\bar{t}$ and Z' samples, the AUC
1875 of all the different origin groups exceeds 0.9, representing strong overall classification
1876 performance. In both samples fake tracks are the easiest to classify, followed by
1877 pileup tracks. The FromC tracks which are c -hadron decay products, are the hardest
1878 to classify, possibly due to their similarity to both fragmentation tracks and b -hadron
1879 decay tracks, depending on the c -hadron species in question.

		AUC		Precision		Recall		F1	
		Mean	Weighted	Mean	Weighted	Mean	Weighted	Mean	Weighted
$t\bar{t}$	MLP	0.87	0.89	0.39	0.71	0.51	0.56	0.36	0.62
	GN1	0.92	0.95	0.51	0.82	0.64	0.70	0.51	0.74
Z'	MLP	0.90	0.94	0.36	0.84	0.47	0.72	0.31	0.76
	GN1	0.94	0.96	0.48	0.88	0.60	0.79	0.48	0.82

Table 6.3: The area under the ROC curves (AUC) for the track classification from GN1, compared to a standard multilayer perceptron (MLP) trained on a per-track basis. The unweighted mean AUC over the origin classes and weighted mean AUC (using as a weight the fraction of tracks from the given origin) is provided. GN1, which uses an architecture that allows track origins to be classified in a conditional manner as discussed in Section 6.4.3, outperforms the MLP model for both $t\bar{t}$ and Z' jets.

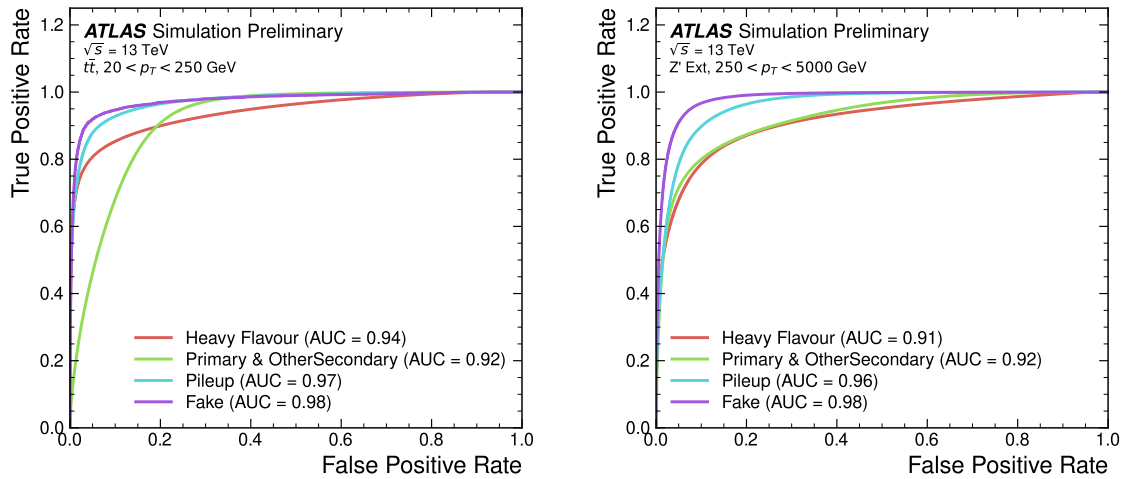


Figure 6.17: ROC curves for the different groups of truth origin labels defined in Table 5.1 for jets in the $t\bar{t}$ sample (left) and jets in the Z' sample (right). The FromB, FromBC and FromC labels have been combined, weighted by their relative abundance, into the Heavy Flavour category, and the Primary and OtherSecondary labels have similarly been combined into a single category. The mean weighted area under the ROC curves (AUC) is similar for both samples.

6.5.8 Looser Track Selection

The track selections used to produce the main results are listed in Table 5.3. This selection includes a cut on the number of shared silicon modules $N_{\text{shared}}^{\text{Si}}$. This value is calculated as

$$N_{\text{shared}}^{\text{Si}} = \frac{N_{\text{shared}}^{\text{Pix}} + N_{\text{shared}}^{\text{SCT}}}{2} \quad (6.10)$$

where $N_{\text{shared}}^{\text{Pix}}$ is the number of shared pixel hits and $N_{\text{shared}}^{\text{SCT}}$ is the number of shared SCT modules on a track. The nominal cut used elsewhere in this thesis is $N_{\text{shared}}^{\text{Si}} < 2$. As the rate of shared hits is significantly higher for b -hadron decay tracks than for other tracks, this cut rejects a significant proportion of these tracks. Figs. 6.18 and 6.19 show the result of training the GN1 tagger with the full relaxation of this cut, i.e. allowing tracks with any number of shared hits. The shared hit requirements applied by the ambiguity solver as part of track reconstruction (see Section 3.4.1) are still applied. In addition, the maximum allowed value of d_0 is increased from 3.5 mm to 5.5 mm.

6.6 Conclusion

In this chapter a novel jet tagger, GN1, is presented. The model has a graph neural network architecture and is trained with auxiliary training objectives, which are shown to improve the performance of the basic model. GN1 significantly improves flavour tagging performance with respect to DL1r, the current default ATLAS flavour tagging algorithm, when compared in simulated collisions. GN1 improves c - and light-jet rejection for jets in the $t\bar{t}$ sample with $20 < p_{\text{T}} < 250$ GeV by factors of ~ 2.1 and ~ 1.8 respectively at a b -jet tagging efficiency of 70% when compared with DL1r. For jets in the Z' sample with $250 < p_{\text{T}} < 5000$ GeV, GN1 improves the c -rejection by a factor of ~ 2.8 and light-jet rejection by a factor of ~ 6 for a comparative b -jet efficiency of 30%.

Previous multivariate flavour tagging algorithms relied on inputs from low-level tagging algorithms, whereas GN1 needs no such inputs, making it more flexible. It can be easily fully optimised via a retraining for specific flavour tagging use cases, as demonstrated with c -tagging and high- p_{T} b -tagging, without the need for

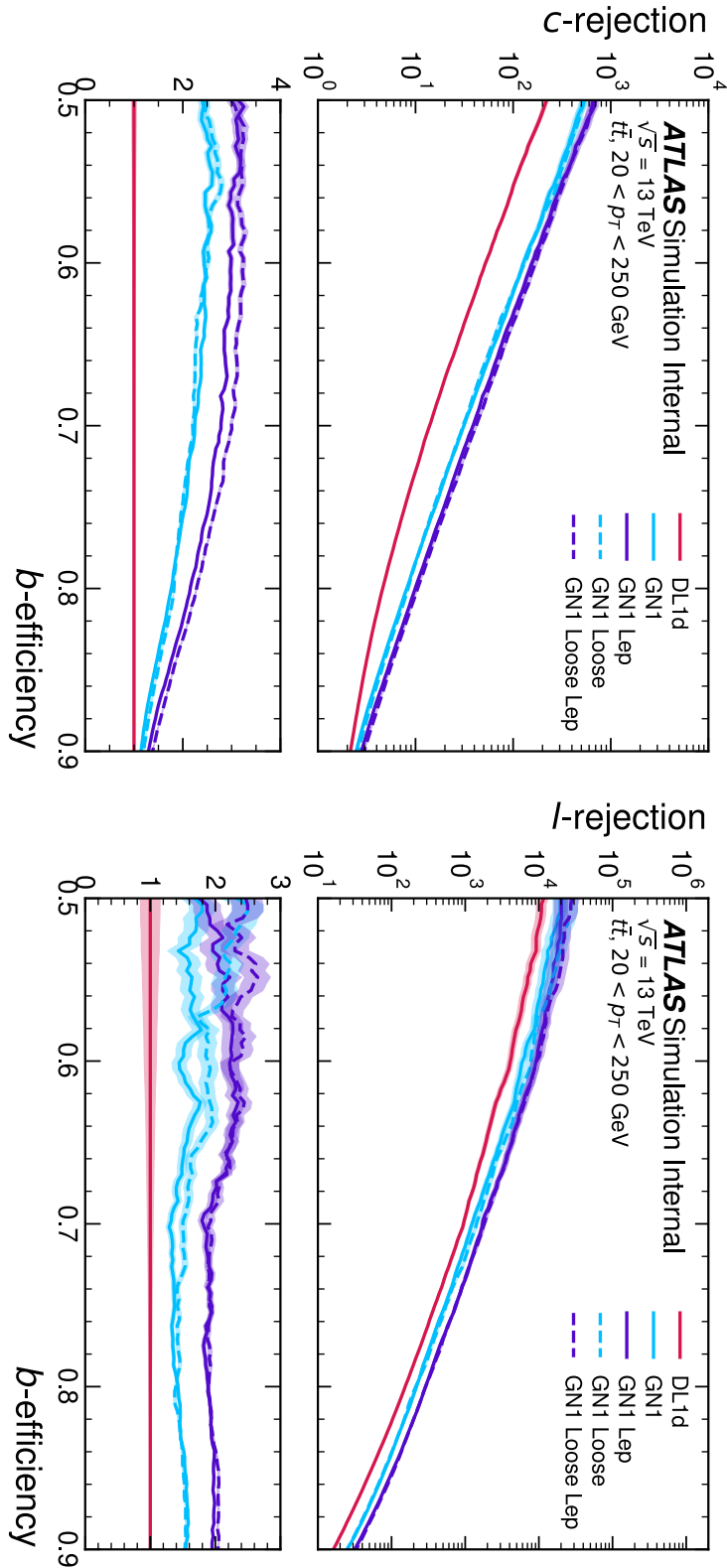


Figure 6.18: The c -jet (left) and light-jet (right) rejections as a function of the b -jet tagging efficiency for $t\bar{t}$ jets with $20 < p_T < 250 \text{ GeV}$, for the looser track selection trainings of GN1. The ratio to the performance of the DL1d algorithm is shown in the bottom panels. A value of $f_c = 0.018$ is used in the calculation of D_b for DL1d and $f_c = 0.05$ is used for GN1. Binomial error bands are denoted by the shaded regions.

1908 time-consuming retuning of the low-level tagging algorithms. The model is also
1909 simpler to maintain and study due to the reduction of constituent components.

1910 GN1 demonstrates improved track classification performance when compared with
1911 a simple per-track MLP and an efficiency of $\sim 80\%$ for inclusive vertex finding in
1912 b -jets. The model is also able to perform vertex finding, and preliminary studies
1913 suggest it outperforms previous manually optimised approaches. The auxiliary track
1914 classification and vertex finding objectives are shown to significantly contribute to
1915 the performance in the jet classification objective, and, along with the more advanced
1916 graph neural network architecture, are directly responsible for the improvement over
1917 DL1r.

1918 Further improvements in the b - and c -tagging performance are likely possible with
1919 a more thorough optimisation of the model architecture, and the integration of
1920 additional information from other parts of the ATLAS detector. The addition of
1921 other auxiliary training objectives, such as the truth b -hadron decay radius and
1922 transverse momentum, may also yield additional performance gains.

1923 Additional future work includes the verification of the performance of GN1 on collision
1924 data, and the full calibration of the model so it can be used by analyses. The flexible
1925 nature of the model means it can also be readily applied to other related problems
1926 outside of standard b - and c -tagging applications, for example $X \rightarrow bb$ and $X \rightarrow cc$
1927 tagging. The model could also be repurposed as a pileup jet tagger, or general
1928 primary and secondary vertexing tool.

1929 The model also demonstrates strong performance for the HLLHC ??.

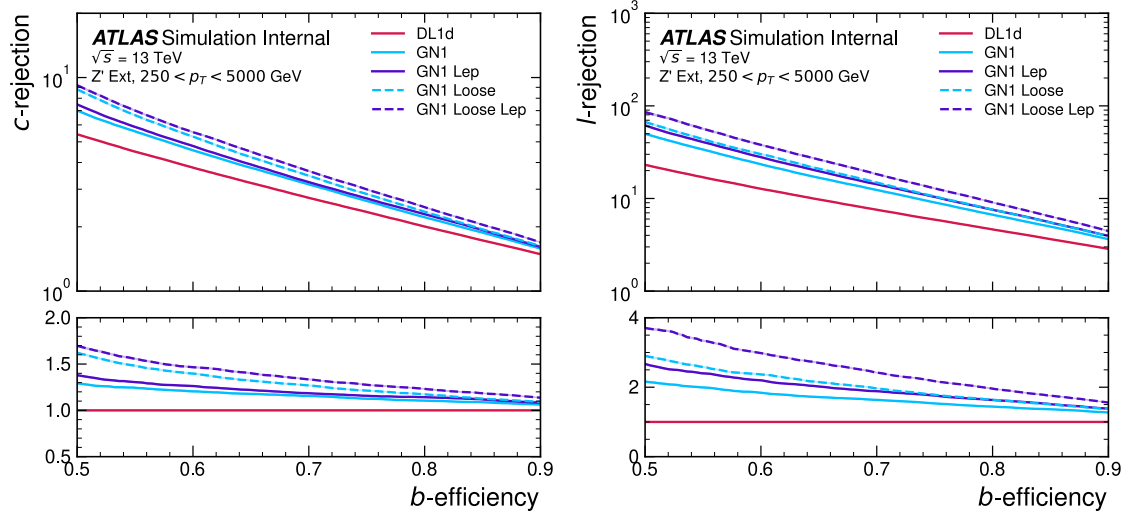


Figure 6.19: The *c*-jet (left) and light-jet (right) rejections as a function of the *b*-jet tagging efficiency for Z' jets with $250 < p_T < 5000$ GeV, for the looser track selection trainings of GN1. The ratio to the performance of the DL1d algorithm is shown in the bottom panels. A value of $f_c = 0.018$ is used in the calculation of D_b for DL1d and $f_c = 0.05$ is used for GN1. Binomial error bands are denoted by the shaded regions.

1930 - paper aux mat - paper internal note - bulk it out

₁₉₃₁

Chapter 7

₁₉₃₂

Boosted VHbb Analysis

₁₉₃₃ The Higgs boson, first observed by ATLAS and CMS at the LHC in 2012 [12, 13],
₁₉₃₄ is predicted by the standard model to decay primarily to a pair of b -quarks, with a
₁₉₃₅ branching factor of 0.582 ± 0.007 for $m_H = 125\text{ GeV}$ [24]. Observation of this decay
₁₉₃₆ mode was reported by ATLAS [104] and CMS [26] in 2018, establishing the first
₁₉₃₇ direct evidence for the Yukawa coupling of the Higgs boson to down-type quarks
₁₉₃₈ (see Section 2.2.2). The $H \rightarrow b\bar{b}$ process is also important for constraining the total
₁₉₃₉ decay width of the Higgs [121].

₁₉₄₀ Whilst the dominant Higgs production mechanism at the LHC is gluon-gluon fusion
₁₉₄₁ as outlined in Section 2.2.3, this mechanism has an overwhelming QCD multijet
₁₉₄₂ background and so overall sensitivity to the Higgs is low. The QCD multijet
₁₉₄₃ background refers to events containing one or more strongly produced jets which are
₁₉₄₄ not the decay product of heavy resonances, for example $g \rightarrow q\bar{q}$. The gluon-gluon
₁₉₄₅ fusion channel contains to leading order only jets in the final state, and therefore
₁₉₄₆ it is extremely difficult to distinguish signal events from the overwhelming multijet
₁₉₄₇ background. The $H \rightarrow b\bar{b}$ observation therefore searched for Higgs bosons produced
₁₉₄₈ in association with a vector boson V (where V can be a W or Z boson) which
₁₉₄₉ subsequently decays leptonically. The leptonic final states from the decay of the
₁₉₅₀ vector boson allow for leptonic triggering whilst at the same time significantly
₁₉₅₁ reducing the multijet background.

₁₉₅₂ A closely related analysis [122] has more recently measured the associated production
₁₉₅₃ of a Higgs boson decaying to b -quarks in events where the vector and Higgs bosons are
₁₉₅₄ highly boosted. The analysis is outlined in Section 7.1. Modelling studies performed
₁₉₅₅ by the author are detailed in Section 7.2, and the results of the analysis are presented

1956 in Section 7.4. The author contributed to various signal and background modelling
1957 studies, fit studies, and to the diboson unblinding effort. This analysis has been
1958 published in Ref. [122]. Figures and tables from Ref. [122] are reproduced here.

1959 7.1 Analysis Overview

1960 The boosted VH , $H \rightarrow b\bar{b}$ analysis is focused on the high transverse momentum
1961 regime, which has the benefit of being more sensitive to physics beyond the Standard
1962 Model [123], but the disadvantage of being more challenging due to the increased dif-
1963 ficulty in the accurate reconstruction of highly energy events (discussed in Chapter 4).
1964 In order to focus on the high- p_T regime, the reconstructed vector boson is required to
1965 have $p_T^V > 250$ GeV (see Section 7.1.2). Events are also split into two p_T^V bins with the
1966 first bin covering $250 \text{ GeV} < p_T^V < 400 \text{ GeV}$ and the second covering $p_T^V > 400 \text{ GeV}$,
1967 which allows the analysis to account for the improved signal-to-background in the
1968 high- p_T regime.

1969 The previous ATLAS analysis in Ref. [104] was primarily sensitive to vector bosons
1970 with a more modest p_T^V boost in the region of 100–300 GeV. In this regime, the Higgs
1971 candidate was reconstructed using a pair of jets with radius parameter of $R = 0.4$,
1972 called small- R jets. However in the high- p_T regime, the decay products of the Higgs
1973 boson become increasingly collimated and the small- R jets may overlap. In order to
1974 avoid the associated problems and to aid in the reconstruction of the Higgs boson
1975 candidate, the present analysis uses instead a large- R jet with radius parameter
1976 $R = 1.0$ to reconstruct the Higgs boson candidate in all channels (see Section 3.4.3).
1977 The Higgs candidate is required to have exactly two ghost-associated and b -tagged
1978 variable-radius track-jets. The candidate large- R jet is reconstructed using jet
1979 substructure techniques, for example it is trimmed by removing soft and wide-angle
1980 components, which helps to remove particles from the underlying event and pileup
1981 collisions [124]. Refer to Section 3.4.3 for more details on jet reconstruction.

1982 On top of the binning in p_T^V , selected events are further categorised into 0-, 1- and
1983 2-lepton channels depending on the number of selected charged leptons (electrons
1984 and muons) are present in the reconstructed final state (also referred to as 0L, 1L,
1985 and 2L respectively). The 0-lepton channel targets the $ZH \rightarrow \nu\nu b\bar{b}$ process, the
1986 1-lepton channel targets $WH \rightarrow \ell\nu b\bar{b}$, and the 2-lepton channel targets $ZH \rightarrow \ell\ell b\bar{b}$,

where ℓ is an electron or muon and ν is a neutrino. Each channel has a dedicated set of selections which are listed in more detail in Section 7.1.3. Events in the 0- and 1-lepton channels are further split depending on the number of additional small- R jets not matched to the Higgs-jet candidate. The high-purity signal region (HP SR) has zero such jets, while the low-purity signal region (LP SR) has one or more. The 0- and 1-lepton channels also make use of a dedicated $t\bar{t}$ control region, described in Section 7.1.4. A complete overview of the different analysis regions is given in Table 7.1.

Channel	Analysis Regions					
	$250 < p_T^V < 400 \text{ GeV}$		$p_T^V \geq 400 \text{ GeV}$			
	0 add. b -track-jets		≥ 1 add. b -track-jets	0 add. b -track-jets		≥ 1 add. b -track-jets
	0 add. small- R jets	≥ 1 add. small- R jets		0 add. small- R jets	≥ 1 add. small- R jets	
0-lepton	HP SR	LP SR	CR	HP SR	LP SR	CR
1-lepton	HP SR	LP SR	CR	HP SR	LP SR	CR
2-lepton	SR			SR		

Table 7.1: Summary of the definition of the analysis regions. Signal enriched regions are marked with the label SR. There are regions with relatively large signal purity (HP SR) and with low purity (LP SR). Background enriched regions are marked with the label CR. The shorthand ‘‘add’’ stands for additional small- R jets, i.e. number of small- R jets not matched to the Higgs-jet candidate.

7.1.1 Data & Simulated Samples

The analysis uses pp collision data recorded between 2015 and 2018 by the ATLAS detector [31] during Run 2 at the LHC. This dataset corresponds to an integrated luminosity of 139 fb^{-1} .

Data from centre-of-mass energy $\sqrt{s} = 13 \text{ TeV}$ proton-proton collisions at the LHC recorded over the course of Run 2 were used for the analysis. The resulting dataset corresponds to a total integrated luminosity of 139 fb^{-1} (see Fig. 3.4).

An overview of the MC simulated samples used in the analysis is given in Table 7.2. These samples are used to model the signal and background processes relevant to the

2004 analysis, with the exception of the multijet background which is modelled using a
2005 data-driven technique. Data and simulated events are reconstructed using the same
2006 algorithms, and a reweighting is applied to the simulated events in order to match
2007 the pile-up distribution observed in the data.

2008 7.1.2 Object Reconstruction

2009 The presence of neutrinos in the $WH \rightarrow \ell\nu b\bar{b}$ and $ZH \rightarrow \ell\ell b\bar{b}$ signatures can be
2010 inferred from a momentum imbalance in the transverse plane Section 3.4.5. The
2011 vector boson transverse momentum p_T^V is reconstructed as the missing transverse
2012 energy E_T^{miss} in the 0-lepton channel, as the magnitude of the summed $\mathbf{E}_T^{\text{miss}}$ and
2013 charged-lepton momentum in the 1-lepton channel, and as the transverse momentum
2014 of the 2-lepton system in the 2-lepton channel (see Section 3.4.5).

2015 Leptons are used for the channel classification and to select relevant events as outlined
2016 in Section 7.1.3. Electrons and muons are reconstructed as outlined in Section 3.4.4.
2017 Electron identification follows the approach outlined in Ref. [104]. In addition to the
2018 likelihood-based method described in Section 3.4.4, *baseline* electrons are required to
2019 satisfy $p_T > 7 \text{ GeV}$, $|\eta| < 2.47$, $s(d_0) < 5$, and $|z_0 \sin(\theta)| < 0.5 \text{ mm}$. *Signal* electron
2020 additionally are required to satisfy a tighter likelihood identification selection. Muons
2021 are required to satisfy $p_T > 7 \text{ GeV}$, $|\eta| < 2.7$, $s(d_0) < 3$, and $|z_0 \sin(\theta)| < 0.5 \text{ mm}$.
2022 *Baseline* muons are required to pass the ‘loose’ identification described in Ref. [73],
2023 while *signal* muons are required to pass the ‘medium’ identification working point.
2024 All signal leptons are required to additionally satisfy a $p_T > 27 \text{ GeV}$ selection criteria,
2025 except for muons in the 1-lepton channel where a cut of 25 GeV is used. The number
2026 of baseline leptons is used to categorise the event into the 0-, 1- or 2-lepton channels.
2027 The 1- and 2-lepton channels additionally require one signal lepton to be present.

2028 The track-jets matched to the Higgs candidate are b -tagged using the MV2c10 b -
2029 tagging algorithm [59, 107, 159]. MV2c10 is a machine learning algorithm using a
2030 Boosted Decision Tree (BDT) which is tuned to achieve an average b -jet efficiency of
2031 70% on simulated $t\bar{t}$ events. At this efficiency working point, rejection factors for
2032 c -jets and light-jets are approximately 9 and 304 respectively. The MV2 algorithm
2033 takes inputs from the outputs of a number of low-level algorithms (IPxD, SV1 and
2034 JetFitter). The outputs of the low-level algorithms are provided as inputs to the
2035 boosted decision tree. The efficiency of the tagging algorithm is calibrated to events

Process	ME generator	ME PDF	PS and Hadronisation	UE model tune	Cross-section order
Signal ($m_H = 125$ GeV and $b\bar{b}$ branching fraction set to 58%)					
$qg \rightarrow W H \rightarrow \ell\nu b\bar{b}$	Powheg-Box v2 [125] + GoSAM [127] + MnLO [128, 129]	NNPDF3.0NLO (*) [93]	Pythia 8.212 [95]	AZNLO	NNLO(QCD) + NLO(EW) [130–136]
$qq \rightarrow ZH \rightarrow \nu\nu b\bar{b}/\ell\ell b\bar{b}$	Powheg-Box v2 + GoSAM + MINLO	NNPDF3.0NLO (*)	Pythia 8.212	AZNLO	NNLO(QCD) (†) + NLO(EW)
$gg \rightarrow ZH \rightarrow \nu\nu b\bar{b}/\ell\ell b\bar{b}$	Powheg-Box v2	NNPDF3.0NLO (*)	Pythia 8.212	AZNLO	NLO + NLL [137–141]
Top quark ($m_t = 172.5$ GeV)					
$t\bar{t}$	Powheg-Box v2 [125, 142]	NNPDF3.0NLO	Pythia 8.230	A14 [96]	NNLO+NNLL [143]
s-channel	Powheg-Box v2 [125, 144]	NNPDF3.0NLO	Pythia 8.230	A14	NLO [145]
t-channel	Powheg-Box v2 [125, 144]	NNPDF3.0NLO	Pythia 8.230	A14	NLO [146]
Wt	Powheg-Box v2 [125, 147]	NNPDF3.0NLO	Pythia 8.230	A14	Approximate NNLO [148]
Vector boson + jets					
$W \rightarrow \ell\nu$	SHERPA 2.2.1 [149–152]	NNPDF3.0NNLO	SHERPA 2.2.1 [153, 154]	Default	NNLO [155]
$Z/\gamma^* \rightarrow \ell\ell$	SHERPA 2.2.1	NNPDF3.0NNLO	SHERPA 2.2.1	Default	NNLO
$Z \rightarrow \nu\nu$	SHERPA 2.2.1	NNPDF3.0NNLO	SHERPA 2.2.1	Default	NNLO
Diboson					
$qq \rightarrow WW$	SHERPA 2.2.1	NNPDF3.0NNLO	SHERPA 2.2.1	Default	NLO
$qq \rightarrow WZ$	SHERPA 2.2.1	NNPDF3.0NNLO	SHERPA 2.2.1	Default	NLO
$qq \rightarrow ZZ$	SHERPA 2.2.1	NNPDF3.0NNLO	SHERPA 2.2.1	Default	NLO
$gg \rightarrow VV$	SHERPA 2.2.2	NNPDF3.0NNLO	SHERPA 2.2.2	Default	NLO

Table 7.2: Signal and background processes with the corresponding generators used for the nominal samples. If not specified, the order of the cross-section calculation refers to the expansion in the strong coupling constant (α_s). (*) The events were generated using the first PDF in the NNPDF3.0NLO set and subsequently reweighted to the PDF4LHC15NLO set [156] using the internal algorithm in POWHEG-BOX v2. (†) The NNLO(QCD)+NLO(EW) cross-section calculation for the $pp \rightarrow ZH$ process already includes the $gg \rightarrow ZH$ contribution. The $gg \rightarrow ZH$ process is normalised using the cross-section for the $pp \rightarrow ZH$ process, after subtracting the $gg \rightarrow ZH$ contribution. An additional scale factor is applied to the $gg \rightarrow VH$ processes as a function of the transverse momentum of the vector boson, to account for electroweak (EW) corrections at NLO. This makes use of the VH differential cross-section computed with HAWK [157, 158].

2036 in data [160–162]. The jet tagging strategy relies on extensive studies into track-jet
2037 b -tagging in boosted topologies [163, 164].

2038 The jet flavour labelling scheme is described in Section 3.4.3.

2039 7.1.3 Selection Criteria

2040 An extensive list of selection cuts are applied to each event in order to reject
2041 background events whilst retaining as many signal events as possible. A full list of
2042 selection cuts applied to the different analysis regions is given in Table 7.3, while
2043 some key selections are listed below.

2044 All channels are require events with at least one large- R jet with $p_T > 250 \text{ GeV}$
2045 and $|\eta| < 2.0$. The vector boson transverse momentum is also required to satisfy
2046 $p_T^V > 250 \text{ GeV}$. The Higgs candidate is chosen as the highest p_T large- R jet satisfying
2047 these requirements. As mentioned, the candidate large- R jet is required to have
2048 two ghost-assciated and b -tagged variable-radius track-jets. These track-jets are
2049 required to have at least two constituent tracks with $p_T > 500 \text{ MeV}$ and $|\eta| < 2.5$.
2050 The track-jets themselves must satisfy $p_T > 10 \text{ GeV}$ and $|\eta| < 2.5$.

2051 In the 0-lepton channel, trigger selections are applied using an E_T^{miss} trigger with a
2052 luminosity-dependent threshold between 70–110 GeV. In the 1-lepton electron sub-
2053 channel a combination of single electron triggers is used with minimum p_T thresholds
2054 between 24–26 GeV. In the muon sub-channel the same E_T^{miss} trigger as the 0-lepton
2055 channel is used. Since muons are not used for the E_T^{miss} trigger calculations, this
2056 is in effect a p_T requirement on the muon-neutrino system, which in the analysis
2057 phase space is more efficient than a single-muon trigger. The 2-lepton channel uses
2058 the same triggering strategy as the 1-lepton channel. In all channels, the trigger
2059 selections applied are fully efficient for events selected using the full requirements in
2060 Table 7.3.

2061 The combined selections in Table 7.3 result in a signal efficiency ranging from 6–16%
2062 for the WH and ZH processes depending on the channel and p_T^V bin.

Selection	0 lepton channel	1 lepton channel	2 leptons channel
Trigger	E_T^{miss}	e sub-channel Single electron	μ sub-channel E_T^{miss}
Leptons	0 <i>baseline</i> leptons	$p_T > 27 \text{ GeV}$ 1 <i>signal</i> lepton no second <i>baseline</i> lepton	2 <i>baseline</i> leptons among which $p_T > 25 \text{ GeV}$ both leptons of the same flavour - opposite sign muons
E_T^{miss}	$> 250 \text{ GeV}$	$> 50 \text{ GeV}$	-
p_T^V			$p_T^V > 250 \text{ GeV}$
Large- R jets		at least one large- R jet, $p_T > 250 \text{ GeV}, \eta < 2.0$	
Track-jets		at least two track-jets, $p_T > 10 \text{ GeV}, \eta < 2.5$, matched to the leading large- R jet	
b -tagged jets		leading two track-jets matched to the leading large- R must be b -tagged (MV2c10, 70%)	
m_1			$> 50 \text{ GeV}$
$\min[\Delta\phi(E_T^{\text{miss}}, \text{small-}R \text{ jets})]$	$> 30^\circ$		-
$\Delta\phi(E_T^{\text{miss}}, H_{\text{cand}})$	$> 120^\circ$		-
$\Delta\phi(E_T^{\text{miss}}, E_{T, \text{trk}}^{\text{miss}})$	$< 90^\circ$		-
$\Delta y(V, H_{\text{cand}})$	-		$ \Delta y(V, H_{\text{cand}}) < 1.4$
$m_{\ell\ell}$	-		$66 \text{ GeV} < m_{\ell\ell} < 116 \text{ GeV}$
Lepton p_T imbalance	-		$(p_T^{\ell_1} - p_T^{\ell_2})/p_T^Z < 0.8$

Table 7.3: Event selection requirements for the boosted VH , $H \rightarrow b\bar{b}$ analysis channels and sub-channels. Various channel dependent selections are used to maximise the signal efficiency and reduce the number of background events in each analysis region.

2063 7.1.4 Control Regions

2064 The $t\bar{t}$ process presents a major background in the 0- and 1-lepton channels. In these
 2065 events, the Higgs candidate is often reconstructed from a correctly tagged b -jet from
 2066 the top decay $t \rightarrow Wb$, and an incorrectly tagged c - or light-jet from the subsequent
 2067 decay of the W , as shown in Fig. 7.1.

not sure
where the
0L ttbar
ETmiss
comes from

2068 The only known decay mode of the top quark is via the weak force to a W and
 2069 a down-type quark. (it is the only quark heavy enough to decay into an on-shell
 2070 W). Overwhelmingly (96% of the time) the down-type quark is a b -quark Hence, the
 2071 second top quark is also likely to result in a second tagged b -tagged track-jet outside
 2072 of the large- R Higgs candidate. To ensure sufficient $t\bar{t}$ rejections, 0- and 1-lepton
 2073 channel signal regions are defined using a veto on events with b -tagged track-jets
 2074 outside the Higgs-jet candidate. These events are used to construct a control region
 2075 (CR) which is enriched in $t\bar{t}$ events. The CR is used to constrain the normalisation
 2076 of the $t\bar{t}$ background in the fit.

2077 7.1.5 Background Composition

2078 After the selections described in Section 7.1.3 the number of background events
 2079 mimicking the VH , $H \rightarrow b\bar{b}$ signal is greatly reduced. However, the number of
 2080 background events still greatly outnumbers that of signal events. The background
 2081 processes are channel dependent. In the 0-lepton channel the dominant sources of
 2082 backgrounds are $Z+jets$ ($Z \rightarrow \nu\nu$) and $t\bar{t}$, with $W+jets$ and diboson events being
 2083 subdominant. In the event of $W \rightarrow \tau\nu$, and subsequent hadronic decay of the τ or
 2084 lack of successful reconstruction/selection of the leptonic decay products, $W+jets$
 2085 can also contribute to the 0-lepton channel. $t\bar{t}$ and $W+jets$ (with a leptonic decay
 2086 of the W as in $W \rightarrow \ell\nu$) are dominant in the 1-lepton channel, while single-top is
 2087 subdominant. In the 2-lepton channel, $Z+jets$ ($Z \rightarrow \ell\ell$) is again dominant followed
 2088 by $Z Z$ diboson events.

2089 The diboson background VV consists primarily of $W Z$ and $Z Z$ events in which the
 2090 Z decays to a pair of b -quarks. This process very closely matches the signal, with
 2091 a resonant peak occurring at $m_Z = 91$ GeV and so is considered as an irreducible
 2092 background ($V+b$ -jets is also irreducible).

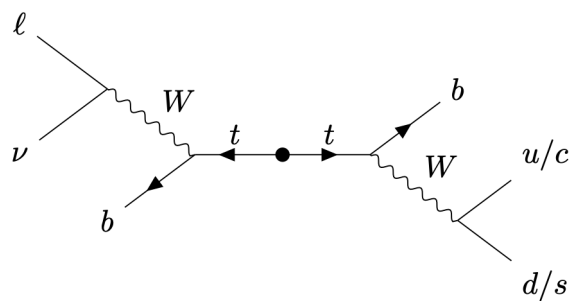
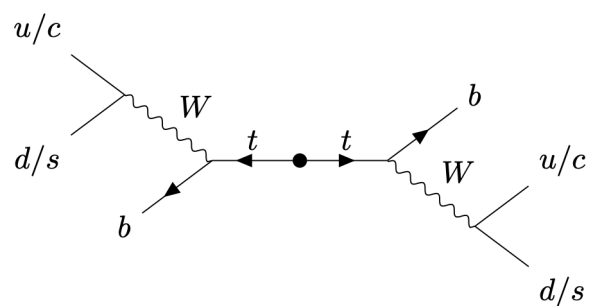
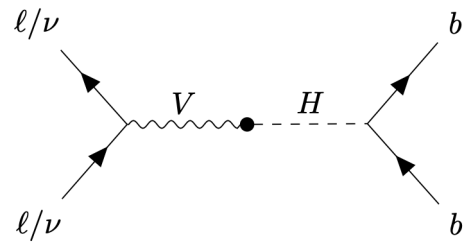


Figure 7.1: Diagrams of the signal process (top) and the 0-lepton and 1-lepton $t\bar{t}$ backgrounds (middle, bottom). Objects to the right of centre are reconstructed within the large- R jet. For the backgrounds, the large- R jet contains a mis-tagged c - or light-jet.

2093 The $t\bar{t}V$, $t\bar{t}H$ and multijet backgrounds are negligible in the analysis phase space
2094 after the selections have been applied, with the exception of the 1-lepton electron
2095 sub-channel, in which multijet background is not ignored. The multijet background
2096 is made up of jets with semileptonic heavy-flavour-hadron decays (e.g. $b \rightarrow c\ell\nu$) and
2097 jets which are mis-tagged by the flavour tagging algorithm MV2c10.

2098 The contributions from the different backgrounds are modelled using Monte Carlo
2099 event generators and the impacts on the analysis are studied in Section 7.2. The
2100 multijet background is not modelled but instead estimated using a data-driven
2101 technique.

2102 7.2 Systematic Uncertainties & Background 2103 Modelling

2104 Systemic uncertainties are extensively employed to give the fit model described in
2105 Section 7.3 enough flexibility to account for inaccuracies in the various inputs to the fit.
2106 Two main types of systematic uncertainty are considered: experimental and modelling.
2107 Experimental uncertainties arise due to the limited due to limited detector precision,
2108 imperfect reconstruction algorithms (in particular the b -tagging algorithms), and
2109 due to the imperfect measurement of pile-up and integrated luminosity. Modelling
2110 is the simulation processes relevant to the analysis using Monte-Carlo (MC) event
2111 generators, and is used to predict the outcome of the analysis. Modelling uncertainties
2112 arise due to the imperfections in the simulation of signal and background events, for
2113 example differences between event generators, or use of different model parameters
2114 when producing simulated events. In order to observe a certain process, for example
2115 VH , $H \rightarrow b\bar{b}$, an increase in the number of observed events with respect to the
2116 background-only hypothesis is looked for. The excess is often relatively small against
2117 the total number of background events, and hence accurate modelling of the expected
2118 number of background and signal events is crucial for successfully performing the
2119 analysis. Particular care is paid to the uncertainties on the modelling predictions as
2120 discussed in this section.

2121 Modelling uncertainties are described in detail in the following sections. Modelling
2122 uncertainties: *Nominal* samples are used as a reference to which different vari-

2123 ations can be compared. The nominal samples are chosen as the best possible
2124 representation of the underlying physical process. *Alternative* samples are used to
2125 understand inaccuracies that may be present in the nominal samples. Some aspect
2126 of the nominal model is varied, and the discrepancy with respect to the nominal
2127 model is quantified. The discrepancy is used to systematic uncertainty associated
2128 with the model parameter which was changed.

2129 Modelling studies involving c - and light-jets is hampered by the low available statistics
2130 of jets pass the analysis selections, due to the high rejection rates of the b -tagging
2131 algorithm MV2c10. For modelling studies therefore, truth tagging (TT) is employed
2132 to ensure sufficient numbers of jets are available to calculate uncertainties. TT works
2133 by computing a 2-dimensional efficiency map using the jet p_T and jet η . The two
2134 leading track-jets associated to the large- R jet automatically passes the b -tagging
2135 requirement, and are weighted based on their p_T and η using the pre-calculated
2136 efficiency map.

2137 7.2.1 Sources of Systematic Uncertainties

2138 This section briefly describes the different sources of uncertainty in the predictive
2139 model used in the analysis, and how each source of uncertainty is implemented within
2140 the analysis framework. Considered sources of systematic uncertainty are listed in
2141 Table 7.4. For each source of uncertainty, acceptance and shape uncertainties are
2142 derived.

2143 QCD Scales

2144 The $V+jets$ matrix element calculations contains infrared and ultraviolet divergences.
2145 These are handled by introducing spurious parameters corresponding to the renormalisation scale (μ_R) and factorisation scale (μ_F). Physical observables are not
2146 dependent on these parameters when using the infinite perturbation series expansion,
2147 however at some fixed order in QCD a limited dependence is present. To assess the
2148 impact of this, both μ_R and μ_F are independently varied from their nominal values
2149 by factors of 0.5 and 2 to account for higher order corrections to the calculation of
2150 the matrix element used to simulate the process.

2152 PDF Sets

2153 Parton distribution functions (PDFs) specify the probability of finding a parton
2154 with a given momentum inside a hadron (in this case, inside colliding protons).
2155 PDFs have to be derived from data and are a significant source of uncertainty in
2156 analyses of hadronic collision data. There are three sources of PDF uncertainties:
2157 the statistical and systematic errors on the underlying data used to derive the PDFs,
2158 the theory which is used to describe them (which is based on some fixed order
2159 perturbative QCD expansion), and finally the procedure which is used to extract the
2160 PDFs from the data. PDF-related uncertainties were derived following Ref. [156].
2161 This involves considering 100 PDF replicas which, when combined, form a central
2162 value and associated uncertainty, and also in parallel direct changes to the central
2163 values of PDFs using the MMHT2014 [165] and CT14NLO [166] PDF sets.

2164 Event Generator

2165 The choice of parton shower (PS) and underlying event (UE) generators can affect
2166 the analysis outcome. Changing these models modifies several aspects of the event
2167 generation at the same time, such as the accuracy of matrix element predictions and
2168 different approaches to parton showering. This change tends to lead to the largest
2169 discrepancy with respect to the nominal samples.

2170 Resummation and Merging Scales

2171 Resummation is a technique used in QCD to help cope with calculations involving
2172 disparate energy scales, and involves the introduction of an associated resummation
2173 scale, the choice of which introduces some systematic uncertainty into the model.
2174 Parton showering models are accurate when simulating low- p_T radiation, however
2175 inaccuracies start to arrive when simulating hard emissions. To combat this, par-
2176 ton showering models utilise more precise matrix element calculations above some
2177 momentum threshold. The choice of threshold, or *merging scale* introduces some
2178 uncertainty into the final result. Resummation (QSF) and merging (CKKW) scale
2179 variations are available for a subset of the SHERPA samples. The number of available
2180 events is significantly lower than the number of events in the nominal sample, and no

2181 statistically significant discrepancy with respect to the nominal samples is observed.
2182 The corresponding uncertainties and therefore neglected.

2183 7.2.2 Implementation of Variations

2184 Modelling variations are implemented in different ways, depending on the associated
2185 uncertainty. Table 7.4 lists the different sources of uncertainty described in Section 7.2.1
and for each lists the implementation. As production of high-stastic MC samples

Source of Uncertainty	Implementation
Renormalisation scale (μ_R)	Internal weights
Factorisation scale (μ_F)	Internal weights
PDF set	Internal weights
Parton Shower (PS) models	Alternative samples
Underlying Event (UE) models	Alternative samples
Resummation scale (QSF)	Parameterisation
Merging scale (CKKW)	Parameterisation

Table 7.4: Different sources of uncertainty (i.e. variations in the model) considered for the $V+jets$ background, and the corresponding implementation. For each uncertainty, acceptance and shape uncertainties are derived.

2186

2187 is computationally expensive, a technique in state of the art simulation packages
2188 is to store some sources of variation as internal weights, which can be generated
2189 alongside the nominal samples, saving computation time. The nominal sample then
2190 effectively contains information about an ensemble of different samples, corresponding
2191 to different model parameters, which are accessible via reweightings. When filling
2192 histograms for the variations, bins are incremented by the internal weight of the
2193 event associated with the variation in question.

2194 While the inclusion of internal weight variation in MC event generators has decreased
2195 simulation times and increased available statistics, there are in SHERPA 2.2.1 currently
2196 some sources of systematic uncertainty that are unable to be stored as internal weight
2197 variations due to technical limitations. Two examples are the choice of resummation
2198 and merging scales. A method to parameterise the systematic variation using
2199 one sample, and to then apply this parameterisation to another sample, has been

2200 developed by ATLAS [167]. This method was used to derive resummation and
2201 merging uncertainties for the nominal SHERPA 2.2.1 sample, using a previous (lower
2202 statistic) SHERPA 2.1 alternative sample. The resulting uncertainties were studied
2203 and found to be negligible in comparison with systematics from other sources.

2204 **7.2.3 Vector Boson + Jets Modelling**

2205 After event selection, the $V+jets$ background is a dominant background in all three
2206 analysis channels as described in Section 7.1.5. The $V+jets$ samples are split into
2207 categories depending on the truth flavour of the track-jets which are ghost-associated
2208 to the large- R jet Higgs candidate. The categories are $V+bb$, $V+bc$, $V+bl$, $V+cc$,
2209 $V+cl$, $V+ll$, and $V+hf$ refers collectively to the categories containing at least one
2210 b - or c -jet. $V+bb$ is dominant generally accounting for 80% of the jets, while $V+hf$
2211 accounts for around 90% of jets. The full flavour composition breakdown for each
2212 channel and analysis region are given in Tables 7.5, 7.7 and 7.8.

2213 In order to access uncertainties associated with the use of MC generators, varia-
2214 tions of the data are produced using alternative generators or variation of nominal
2215 generator parameters as described in Section 7.2.2. As described in Section 7.1.1,
2216 the nominal MC event generator used for $V+jets$ events is SHERPA 2.2.1, while
2217 MADGRAPH5_AMC@NLO+PYTHIA8 (which uses a different parton showering
2218 model) is used as an alternative generator.

2219 Modelling systematics can have several impacts, including affecting the overall
2220 normalisation for different processes, and the relative acceptances between different
2221 analysis regions (i.e. migrations between HP and LP SRs, between the SR and CR,
2222 and between p_T^V bins), and the shapes of the m_J distributions. Since the fit model
2223 fits only the large- R jet mass m_J to data, all shape uncertainties are estimated with
2224 respect to this observable. Several sources of uncertainty, summarised in Section 7.2.1,
2225 have been assessed.

Sample	Mp_T^V HP SR	Hp_T^V HP SR	Mp_T^V LP SR	Hp_T^V LP SR	Mp_T^V CR	Hp_T^V CR
Wbb	$79.3\% \pm 4.4\%$	$75.0\% \pm 8.6\%$	$77.4\% \pm 2.5\%$	$71.7\% \pm 4.5\%$	$68.0\% \pm 7.6\%$	$63.5\% \pm 14.0\%$
Wbc	$6.6\% \pm 0.9\%$	$3.4\% \pm 1.7\%$	$6.2\% \pm 0.5\%$	$5.3\% \pm 0.9\%$	$14.5\% \pm 3.2\%$	$3.4\% \pm 3.2\%$
Wbl	$3.9\% \pm 0.9\%$	$11.4\% \pm 3.5\%$	$4.5\% \pm 0.5\%$	$8.7\% \pm 1.4\%$	$9.8\% \pm 2.2\%$	$9.1\% \pm 3.8\%$
Wcc	$5.1\% \pm 1.7\%$	$6.8\% \pm 2.4\%$	$7.1\% \pm 1.0\%$	$6.3\% \pm 1.4\%$	$4.2\% \pm 2.4\%$	$12.3\% \pm 7.0\%$
Wcl	$2.3\% \pm 1.4\%$	$2.4\% \pm 2.1\%$	$3.4\% \pm 0.7\%$	$5.2\% \pm 1.5\%$	$2.6\% \pm 1.5\%$	$3.4\% \pm 2.1\%$
Wl	$2.9\% \pm 1.0\%$	$0.9\% \pm 1.6\%$	$1.3\% \pm 0.7\%$	$2.8\% \pm 0.7\%$	$0.9\% \pm 0.6\%$	$8.4\% \pm 5.1\%$
Events	187.5 ± 7.7	38.2 ± 3.1	429.5 ± 10.0	97.8 ± 4.2	33.8 ± 2.5	8.3 ± 1.2

Table 7.5: 0-lepton $W+jets$ nominal sample flavour composition and total event yield.

Sample	Mp_T^V HP SR	Hp_T^V HP SR	Mp_T^V LP SR	Hp_T^V LP SR	Mp_T^V CR	Hp_T^V CR
Wbb	$77.2\% \pm 2.6\%$	$72.4\% \pm 4.3\%$	$77.8\% \pm 1.8\%$	$69.3\% \pm 2.5\%$	$64.6\% \pm 4.9\%$	$53.5\% \pm 6.3\%$
Wbc	$7.4\% \pm 0.7\%$	$7.3\% \pm 1.1\%$	$6.6\% \pm 0.4\%$	$6.3\% \pm 0.6\%$	$13.7\% \pm 1.9\%$	$16.4\% \pm 3.7\%$
Wbl	$4.0\% \pm 0.5\%$	$6.7\% \pm 1.1\%$	$5.1\% \pm 0.3\%$	$8.7\% \pm 0.8\%$	$10.3\% \pm 1.7\%$	$14.6\% \pm 3.0\%$
Wcc	$6.2\% \pm 1.1\%$	$5.5\% \pm 1.7\%$	$6.6\% \pm 0.6\%$	$6.4\% \pm 0.7\%$	$4.5\% \pm 1.7\%$	$9.5\% \pm 3.0\%$
Wcl	$3.6\% \pm 0.8\%$	$4.2\% \pm 1.8\%$	$2.8\% \pm 0.5\%$	$6.2\% \pm 0.8\%$	$4.6\% \pm 1.2\%$	$4.4\% \pm 1.5\%$
Wl	$1.5\% \pm 0.5\%$	$3.9\% \pm 1.3\%$	$1.1\% \pm 0.2\%$	$3.1\% \pm 0.5\%$	$2.3\% \pm 1.2\%$	$1.6\% \pm 0.6\%$
Events	477.1 ± 11.7	147.5 ± 6.4	784.7 ± 12.3	301.8 ± 7.2	68.7 ± 3.5	26.9 ± 2.0

Table 7.6: 1-lepton $W+jets$ nominal sample flavour composition and total event yield.

Channel	Mp_T^V HP SR	Hp_T^V HP SR	Mp_T^V LP SR	Hp_T^V LP SR	Mp_T^V CR	Hp_T^V CR
Zbb	84.56%	81.84%	82.37%	76.06%	66.12%	63.18%
Zbc	6.03%	6.98%	5.80%	7.46%	15.04%	14.30%
Zbl	4.06%	6.55%	3.83%	6.59%	12.66%	12.81%
Zcc	3.68%	3.40%	5.82%	3.75%	3.36%	3.38%
Zcl	1.23%	0.44%	1.47%	3.97%	1.82%	4.95%
Zl	0.44%	0.78%	0.70%	2.16%	1.00%	1.38%
Events	259.91 ± 4.86	66.12 ± 2.04	420.45 ± 5.73	141.97 ± 2.50	43.49 ± 1.73	16.07 ± 0.83

Table 7.7: 0-lepton $Z+jets$ nominal sample flavour composition and total event yield.

Channel	Mp_T^V	Hp_T^V	p_T^V inclusive
Zbb	80.80%	76.95%	79.76%
Zbc	8.10%	6.26%	7.60%
Zbl	4.95%	7.06%	5.52%
Zcc	3.97%	4.46%	4.10%
Zcl	1.61%	3.60%	2.14%
Zll	0.57%	1.68%	0.87%
Events	115.49 ± 2.42	42.42 ± 1.27	157.92 ± 2.73

Table 7.8: 2-lepton $Z+jets$ nominal sample flavour composition and total event yield.

2226 Acceptance Uncertainties

2227 Several different types of acceptance uncertainties have been calculated and imple-
2228 mented as nuisance parameters in the fit. These account for uncertainty in the overall
2229 number of events in each channel, and for the migration of events between different
2230 analysis regions. The acceptance uncertainties relevant to the $V+jets$ processes are
2231 summarised below.

- 2232 • Overall normalisation:** only relevant where normalisation cannot be left
2233 floating (determined as part of the fit). The $V+hf$ component is left floating in
2234 the fit. For other components, independent normalisations used for $W+hf$ and
2235 $Z+hf$. The contributions are mainly determined by the 1-lepton (for $W+hf$)
2236 and 2-lepton (for $Z+hf$) SRs respectively and then extrapolated to 0-lepton
2237 channel.
- 2238 • SR-to-CR relative acceptance:** the uncertainty on the normalisation of the
2239 signal region due to events migrating between the signal and control regions.
- 2240 • HP-to-LP relative acceptance:** the uncertainty on the normalisation of the
2241 high-purity (HP) signal region due to events migrating between the high- and
2242 low-purity signal regions.
- 2243 • Medium-to-high p_T^V relative acceptance:** describes any shape effect in p_T^V
2244 distribution, given that the analysis only uses two p_T^V bins (medium and high).
- 2245 • Flavour relative acceptance:** for each flavour $V+xx$, where $xx \in \{bc, bl, cc\}$
2246 the ratio of $V+xx/V+bb$ events is calculated. This corresponds to the uncer-
2247 tainty of Vbb events due to the miss-tagging of other flavours Vxx .
- 2248 • Channel relative acceptance:** corresponding to the uncertainty in the nor-
2249 malisation of $V+jets$ events events due to the migration of events between
2250 channels.

2251 The uncertainties arising from the different sources described in Section 7.2.1 are
2252 summed in quadrature to give a total uncertainty on each region. A summary of the
2253 different acceptance uncertainties that were derived in this way and subsequently
2254 applied in the fit are given in Table 7.9. An effort has been made, wherever possible,
2255 to harmonise similar uncertainties across different analysis regions and channels.

V+jets Acceptance Uncertainties				
Boson	W		Z	
Channel	0L	1L	0L	2L
Vbb Norm.	30%	-	-	-
SR/CR	90% [†]	40% [†]	40%	-
HP/LP	18%		18%	-
High/Medium p_T^V	30%	10%*	10%	
Channel Extrap.	20%	-	16%	-
Vbc/Vbb	30%			
Vbl/Vbb	30%			
Vcc/Vbb	20%			
Vcl Norm.	30%			
VL Norm.	30%			

Table 7.9: V+jets acceptance uncertainties. W+jets SR and CR uncertainties marked with a superscript † are correlated. The 1L W+jets H/M uncertainty marked by * is applied as independent and uncorrelated NPs in both HP and LP signal regions. The 0L W+jets Wbb Norm uncertainty is only applied when a floating normalisation for Wbb cannot be obtained from the 1L channel. A 30% uncertainty for $Z \rightarrow b\bar{b}$ norm is applied in the 1L channel when a floating normalisation for $Z \rightarrow b\bar{b}$ cannot be obtained from the 0L or 2L channels.

2256 Shape Uncertainties

2257 In order to derive shape uncertainties (which as the name suggests affect shapes but
 2258 not overall normalisations of distributions), the following procedure is carried out.
 2259 Normalised distributions of the reconstructed large- R Higgs candidate jet mass m_J
 2260 are compared for the nominal sample and variations. For each variation, the ratio of
 2261 the variation to nominal is calculated, the up and down variations are symmetrised,
 2262 and an analytic function is fit to the symmetrised ratio. If different analysis regions
 2263 or channels show the same pattern of variation, a common uncertainty is assigned.
 2264 An example of a significant source of uncertainty, arising from choice of factorisation
 2265 scale μ_R is shown in Fig. 7.2. HP SRs split into medium and high p_T^V bins are shown
 2266 for the 0-lepton channel for $W+\text{hf}$ and $Z+\text{hf}$ jets. The 0- and 1-lepton channels for
 2267 the $W+\text{hf}$ contribution and the 0- and 2-lepton channels for the $Z+\text{jets}$ contribution
 2268 are merged, since the shapes in m_J are consistent across channels. An exponential
 2269 function $e^{p_0 + p_1 x} + p_2$ has been fitted to the ratio of the normalised distributions.
 2270 The magnitude of the variation does show p_T^V dependence, and so two separate
 2271 uncertainties are added in the fit, and applied individually in each p_T^V region.
 2272 The shape uncertainties for μ_R were derived on the SRs but are also applied to the
 2273 CRs, as the low statistics in the CRs make it difficult to derive dedicated shape
 2274 uncertainties. All the shape uncertainties are fully correlated across regions.
 2275 A comparison of the m_J shapes between SHERPA and MADGRAPH is shown in
 2276 Fig. 7.3. The plots are split by process and channel, but merged in SR purity and p_T^V
 2277 bins reflecting similarities between the m_J shapes across these regions. Due to the low
 2278 statistics available for the alternate MADGRAPH sample, and the lack of statistically
 2279 significant variation between the samples, no associated shape uncertainty is added
 2280 to the fit in this case.
 2281 The impacts of variations in the factorisation scale μ_F and the choice of PDF set on
 2282 m_J shape were also found to be negligible in comparison with μ_R and are hence not
 2283 associated uncertainty was added to the fit.

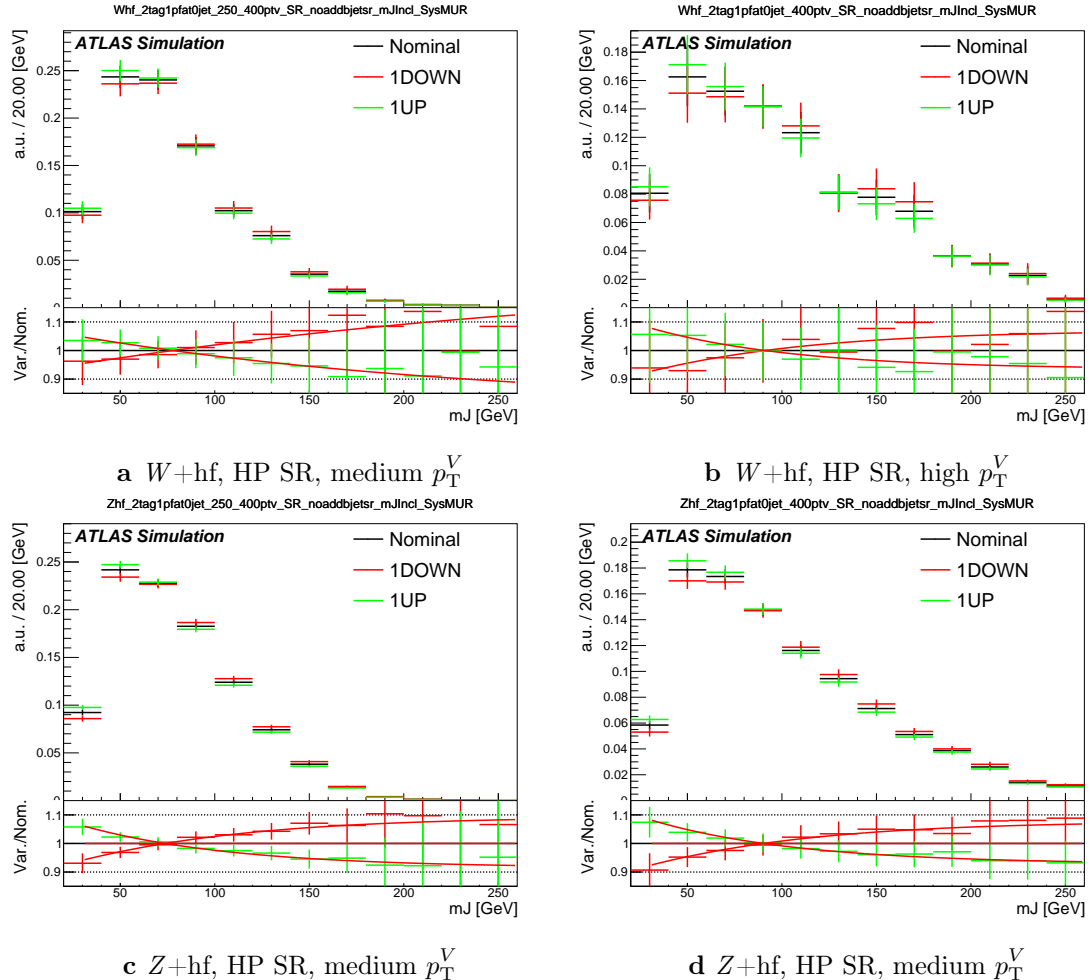


Figure 7.2: Normalised leading large- R jet mass distribution from Z and $W + hf$ processes in the HP SR of the 0-lepton channel. The renormalisation scale μ_r has been varied by a factor of 2 (1up) and 0.5 (1down). An exponential function is fitted to the ratio between the nominal and variation samples.

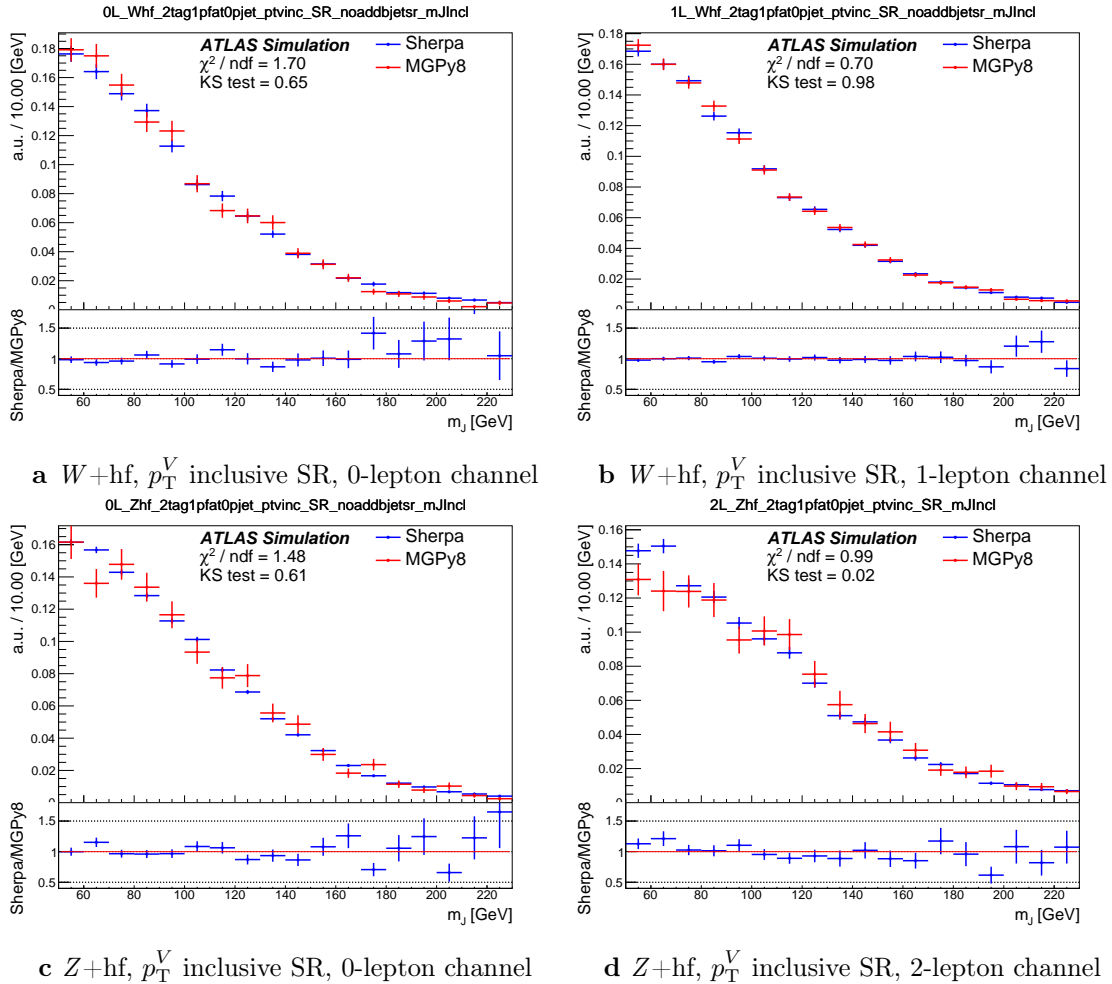


Figure 7.3: The comparison on m_J shapes between SHERPA and MADGRAPH samples from $V+hf$ process in p_T^V inclusive signal regions. The Kolmogorov-Smirnov test and χ^2/ndf are shown on the plots.

7.2.4 Diboson Modelling

The uncertainties for the diboson background generally follows that of $V+jets$. However an alternative sample was generated using POWHEG interfaced with PYTHIA8, using the AZNLO shower tune with the CTEQ6L1 PDFs [168]. Unlike SHERPA, POWHEG models the off-shell Z contribution at NLO.

Acceptance and shape uncertainties are derived in an analogous fashion to $V+jets$.

Acceptance Uncertainties

Diboson acceptance uncertainties are summarised in Table 7.10. Variations from μ_R , μ_F , PDF choice and alternative generator are considered and are combined through a sum in quadrature as described in Section 7.2.3. The largest modification to the nominal acceptance results from the POWHEG+PYTHIA8 alternate sample, which modifies several parts of the generative model at the same time. Since the diboson contribution to the $t\bar{t}$ control region is small, no SR-to-CR relative acceptance uncertainty is required.

For the WZ contribution, uncertainties are derived using the 1-lepton channel and applied to all three channels. An additional 8% channel migration uncertainty is applied on the 0-lepton channel. For the ZZ contribution, the normalisation uncertainty is calculated using the 2-lepton channel and applied to all three channels. The 0- and 1-lepton channels have a similar HP-to-LP relative acceptance uncertainty of 18%. The 1-lepton medium-to-high p_T^V relative acceptance is based off the value obtained from the 2-lepton channel. 30% and 18% channel migration uncertainties are applied in the 0- and 1-lepton channels respectively.

Since the contribution from WW is small, dedicated studies are not performed, but a 25% normalisation uncertainty is applied in all the three channels which is based on the modelling studies performed for the previous analysis [104].

Shape Uncertainties

Diboson shape uncertainties are derived in a similar fashion to $V+jets$. Only the uncertainties associated with systematic variation of μ_R and the event generator

Diboson Acceptance Uncertainties						
Bosons	WZ			ZZ		
Channel	0L	1L	2L	0L	1L	2L
Normalisation	16%			10%		
HP/LP	18%			18%		
High/Medium	10%			6%	18%	
Channel Extrap.	8%	-	-	30%	18%	-

Table 7.10: Diboson acceptance uncertainties. All uncertainties except channel extrapolation uncertainties are fully correlated between ZZ and WZ processes and channels.

have a non-negligible impact on the m_J shape. Variation of μ_R produces consistent m_J shape impacts across all regions and channels, and hence only a single associated uncertainty is derived, shown in Fig. 7.4. A hyperbolic tangent is fitted to the symmetrised ratio.

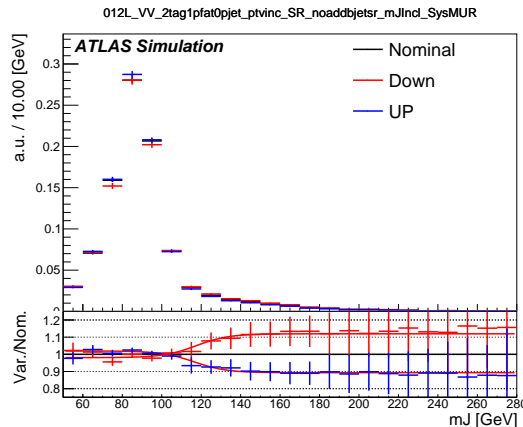


Figure 7.4: Normalised leading large- R jet mass distribution from WZ and ZZ process, merged among all the signal regions and lepton channels. The renormalisation scale μ_R has been varied by a factor of 2 (1up) and 0.5 (1down). The red line shape shows the fitting results of the hyperbolic tangent function.

The comparison between the nominal SHERPA and alternative POWHEG+PYTHIA samples is shown in Fig. 7.5 for the 0- and 1-lepton channels for both WZ and ZZ processes. For these channels, the shape of m_J varies in opposite directions in the LP and HP signal regions. Shapes are similar between p_T^V bins, the 0- and 1-lepton channels and for WZ and ZZ . A third order polynomial is fitted to the ratio, and this function transitions to a constant piecewise function in the high

mass region to accurately represent the shape taking into account large statistical uncertainties. Dependence on event generator was found to be negligible within statistical uncertainty in the 2-lepton channel. All diboson shape uncertainties are fully correlated in the fit.

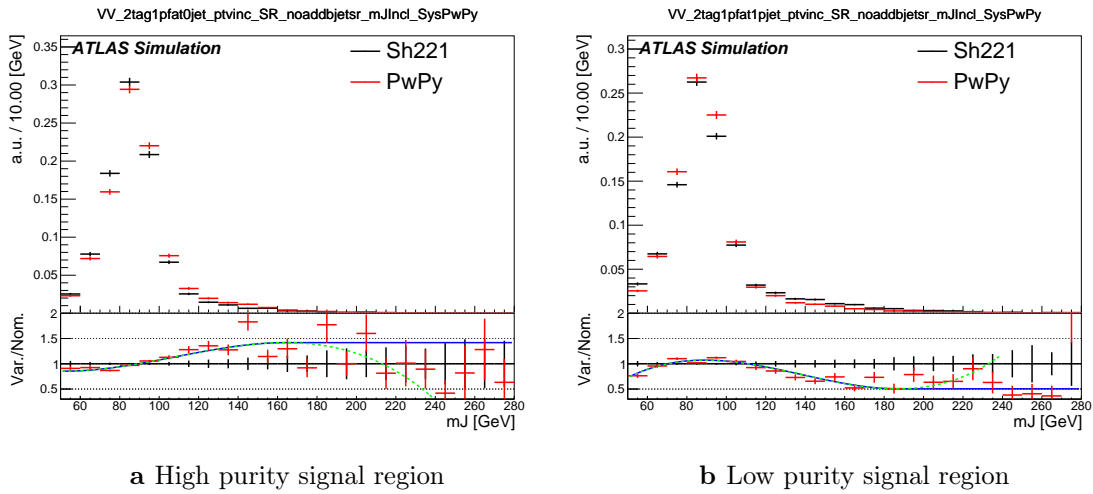


Figure 7.5: The comparison on m_J shapes between SHERPA and POWHEG+PYTHIA 8 samples from WZ and ZZ process in high and low purity signal regions. p_T^V regions and 0- and 1-lepton channels are merged. The dashed green line shows the fitted third order polynomial function and the blue lines show the function after a protection is added in the high mass region.

7.3 Statistical Treatment

Selected events are used to perform a statistical test of the background-only hypothesis, i.e. a model which does not include the VH , $H \rightarrow b\bar{b}$ process. The test involves a binned global maximum-profile-likelihood fit from the model to the data using the m_J distribution, and combines all the analysis regions defined in Table 7.1. The test is based on the profile likelihood ratio test statistic. The signal strength $\mu = \sigma/\sigma_{SM}$ is defined as the ratio between the observed and predicted cross-sections, where $\mu = 0$ corresponds to the background-only hypothesis and $\mu = 1$ corresponds to the SM prediction. It is a parameter of interest (POI) which acts to scale the total number of signal events.

The present analysis makes use of two POIs. The first, μ_{VH}^{bb} , is the signal strength for the VH , $H \rightarrow b\bar{b}$ process, the primary process under investigation. The diboson

2338 production strength μ_{VZ}^{bb} for the VZ , $Z \rightarrow b\bar{b}$ process is measured simultaneously
 2339 and provides a validation of the analysis apparatus used for the primary $H \rightarrow b\bar{b}$
 2340 measurement. Alongside the two POIs, the predictive model depends on several
 2341 uninteresting parameters which are not the primary target of measurement. These
 2342 parameters are called nuisance parameters (NPs), collectively referred to as θ . Freely
 2343 floating background normalisations are implemented as NPs and are also extracted
 2344 during the fitting processes.

2345 7.3.1 Likelihood Function

2346 The statistical setup treats each bin as a Poisson counting experiment and is based on
 2347 the ROOSTATS framework [169]. The combined likelihood over N bins is constructed
 2348 as the product of Poisson probabilities in each bin. Considering the simplified case
 2349 of a single signal strength parameter μ , and neglecting sources of systematic or
 2350 statistical uncertainty, this is given by

$$\mathcal{L}(\mu) = \prod_{i=1}^N \frac{(\mu s_i + b_i)^{n_i}}{n_i!} \exp [-(\mu s_i + b_i)], \quad (7.1)$$

2351 where s_i (b_i) is the expected number of signal (background) events in bin i , and n_i is
 2352 the number of observed data events in bin i .

2353 Treatment of Uncertainties

2354 Systematic uncertainties can modify the predicted signal and background yields s_i
 2355 and b_i . Each source of systematic uncertainty is taken into account by adding an
 2356 additional NP θ_j to the likelihood in the form of a Gaussian cost function. The
 2357 combined effect of the NPs is then

$$\mathcal{L}(\theta) = \prod_{j=1}^{N_\theta} \frac{1}{\sqrt{2\pi}\sigma_j} \exp \left[\frac{-(\bar{\theta}_j - \theta_j)^2}{2\sigma_j^2} \right], \quad (7.2)$$

2358 where N_θ is the number of NPs, $\bar{\theta}_j$ is the nominal value of the j th NP, θ_j is the fitted
 2359 value, and σ_j is the corresponding associated prior uncertainty on θ_j . As the fitted
 2360 value of the θ_j deviates from its nominal value, a cost is introduced. The presence

2361 of NPs modifies the likelihood as

$$\mathcal{L}(\mu) \rightarrow \mathcal{L}(\mu, \theta) = \mathcal{L}(\mu)\mathcal{L}(\theta). \quad (7.3)$$

2362 The predicted signal and background yields are also modified by the presence of the
2363 NPs with

$$s_i \rightarrow s_i(\theta), \quad b_i \rightarrow b_i(\theta). \quad (7.4)$$

2364 For NPs which are left freely floating in the fit, no corresponding Gaussian constraint
2365 is added to the likelihood.

2366 Statistical uncertainty is also present, and implemented using a dedicated NP for
2367 each bin which can scale the background yield in that bin. Statistical NPs are also
2368 implemented using a Gaussian constraint.

2369 Smoothing and Pruning

2370 Systematic uncertainties are smoothed and pruned in the fit. Smoothing accounts
2371 for the large statistical uncertainty present in some bins that are subject to large
2372 fluctuations. The smoothing procedure relies on the assumption that the impact of
2373 systematics should be approximately monotonic and correlated between neighbouring
2374 bins.

2375 In addition to smoothing, pruning is the process of removing from the fit those
2376 systematics which only have a very small effect. This improves the stability of the
2377 fit by reducing the number of degrees of freedom. Acceptance uncertainties are
2378 pruned in a given region if they have a variation of less than 0.5%, or if the up and
2379 down variations have the same sign in that region. Shape uncertainties are pruned
2380 in a given region if the deviation in each bin is less than 0.5% in that region. In
2381 addition, acceptance and shape uncertainties are neglected in a given region for any
2382 background which makes up less than 2% of the total background in a given region.

2383 **Fit Procedure and Statistical Tests**

2384 The best-fit value of μ , denoted $\hat{\mu}$, is obtained via an unconditional maximisation
2385 of the likelihood. The likelihood is also used to construct a statistical test which can
2386 confirm or reject the background-only hypothesis. The test statistic q_μ is constructed
2387 from the profile likelihood ratio, as in

$$q_\mu = -2 \ln \frac{\mathcal{L}(\mu, \hat{\theta}_\mu)}{\mathcal{L}(\hat{\mu}, \hat{\theta})} \quad (7.5)$$

2388 where $\hat{\mu}$ and $\hat{\theta}$ are chosen to maximise the likelihood \mathcal{L} , and the profile value $\hat{\theta}_\mu$ is
2389 obtained from a conditional maximisation fo the likelihood for a specific choice of
2390 $\mu = 0$ corresponding to the background-only hypothesis.

2391 The test statistic is used to construct a p -value which is used to confirm or accept
2392 the background-only hypothesis. The p -value is typically reported in terms of the
2393 significance Z , defined as the number of standard deviations for a Gaussian Normal
2394 distribution which will produce a one-sided tail integral equal to the p -value, as in

$$p = \int_Z^\infty \frac{1}{\sqrt{2\pi}} e^{-x^2/2} dx = 1 - \Phi(Z). \quad (7.6)$$

2395 Typically a value of $Z = 3$ constitutes *evidence* of a processes, while $Z = 5$ is required
2396 for a *discovery*. Alongside the p -value, the best-fit value of the signal strength $\hat{\mu}$ and
2397 its corresponding uncertainty are typically quoted, and compared to their expected
2398 values (see Section 7.3.3).

2399 **7.3.2 Background Normalisations**

2400 The normalisation of the largest backgrounds are left floating and are determined in
2401 the fit. The corresponding postfit background normalisations are listed in Table 7.11.
2402 A single normalisation factor is used for $W+\text{hf}$ and $Z+\text{hf}$, which constitue more
2403 than 90% of the total $V+\text{jets}$ background, since the use of independent factors in
2404 different channels were found to be compatible.

Process	Normalisation factor
$t\bar{t}$ 0-lepton	0.88 ± 0.10
$t\bar{t}$ 1-lepton	0.83 ± 0.09
$W+\text{hf}$	1.12 ± 0.14
$Z+\text{hf}$	1.32 ± 0.16

Table 7.11: Factors applied to the nominal normalisations of the $t\bar{t}$, $W+\text{hf}$, and $Z+\text{hf}$ backgrounds, as obtained from the likelihood fit. The errors represent the combined statistical and systematic uncertainties.

2405 The normalisations and shapes of all other backgrounds, with the exception of the
 2406 multijet background which is estimated using a data driven technique, are initialised
 2407 using the simulated samples.

2408 7.3.3 Asimov Dataset & Expected Results

2409 The Asimov dataset is constructed by replacing the data with the sum of the signal
 2410 and background predictions $n_i = s_i + b_i$. A fit to this dataset using the nominal
 2411 values of the NPs from the simulation will recover the input values and is useful for
 2412 studying constraints on and correlations between the NPs.

2413 Alternatively, a conditional fit to the Asimov dataset can be performed using values
 2414 of the background NPs which are determined from an unconditional fit to data. The
 2415 signal NPs and POIs are fixed at their nominal values from the SM simulation. The
 2416 result of this fit can be used to calculate expected (median) significances, which can
 2417 be compared to their observed values.

2418 7.4 Results

2419 In the present analysis, the two signal strength parameters μ_{VH}^{bb} and μ_{VZ}^{bb} are extracted
 2420 from a simultaneous maximisation of the likelihood described in Section 7.3. The
 2421 results of the analysis are summarised in this section. Post-fit m_J distributions are
 2422 shown in Section 7.4.1. The observed signal strengths are given in Section 7.4.2,
 2423 along with observed and expected significances. Finally in Section 7.4.3 the impact
 2424 of systematic uncertainties on the results is examined.

2425 7.4.1 Post-fit Distributions

2426 In addition to the observed significance and signal strength, it is also useful to study
 2427 the post-fit m_J distributions to compare the simulation and data using the best-fit
 2428 values $\hat{\mu}$ and $\hat{\theta}$. Post-fit m_J distributions are given for the signal regions in the 0-,
 2429 1- and 2-lepton channels in Fig. 7.6. The LP and HP regions are merged for the
 2430 0- and 1-lepton channels. The plots show large falling backgrounds, predominantly
 2431 made up of W -jets and Z -jets events, and a signal distribution corresponding to
 2432 the Standard Model Higgs boson peaking around $m_H = 125$ GeV. In general there is
 2433 a good level of agreement between the simulation and data, indicating the fit model
 2434 is performing as expected. Fig. 7.7 shows the post-fit plots for the $t\bar{t}$ control regions.
 2435 Again, a good level of agreement is observed given the statistical uncertainties on
 2436 the distributions.

2437 7.4.2 Observed Signal Strength & Significance

2438 The measured signal strength is computed as the ratio between the measured signal
 2439 yield to the prediction from the SM. The combined result for all three lepton channels
 2440 and all analysis regions is given for μ_{VH}^{bb} in Eq. (7.7), and for μ_{VZ}^{bb} is given in Eq. (7.8).
 2441 Both results include a full breakdown of the systematic and statistical uncertainties.

$$\mu_{VH}^{bb} = 0.72^{+0.39}_{-0.36} = 0.72^{+0.29}_{-0.28}(\text{stat.})^{+0.26}_{-0.22}(\text{syst.}) \quad (7.7)$$

2442

$$\mu_{VZ}^{bb} = 0.91^{+0.29}_{-0.23} = 0.91 \pm 0.15(\text{stat.})^{+0.24}_{-0.17}(\text{syst.}) \quad (7.8)$$

2443 The results for μ_{VH}^{bb} and μ_{VZ}^{bb} agree with the expectation from the SM within their
 2444 combined uncertainty. The μ_{VH}^{bb} measurement is dominated by statistical uncertainty,
 2445 while the μ_{VZ}^{bb} measurement is dominated by systematic sources of uncertainty. These
 2446 measured signal strength for μ_{VZ}^{bb} corresponds to an observed significance of 2.1
 2447 standard deviations, with an expected (median) significance given the SM prediction
 2448 of 2.7 standard deviations obtained using the method described in Section 7.3.3. The
 2449 diboson observed (expected) signal strength significance is 5.4 (5.7). These results
 2450 are summarised in Fig. 7.8, which shows the background-subtracted m_J distribution.
 2451 A clear signal excess is visible around the Higgs mass of $m_H = 125$ GeV.

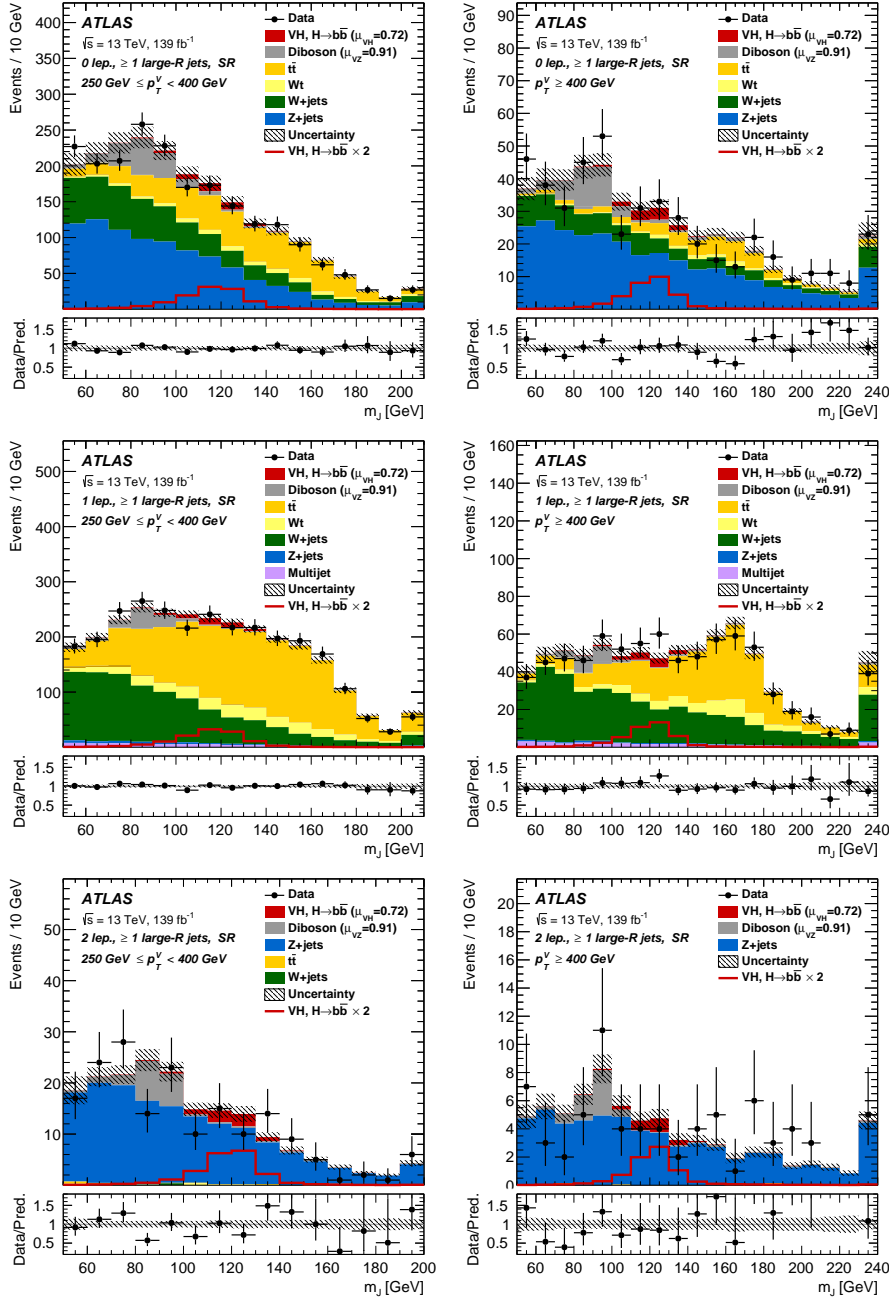


Figure 7.6: The m_J post-fit distributions in (top) the 0-, (middle) 1- and (bottom) 2-lepton SRs for (left) $250 \text{ GeV} < p_T^V < 400 \text{ GeV}$ and (right) $p_T^V \geq 400 \text{ GeV}$. The LP and HP regions are merged for the 0-lepton and 1-lepton channels. The fitted background contributions are shown as filled histograms. The Higgs boson signal ($m_H = 125 \text{ GeV}$) is shown as a filled histogram and is normalised to the signal yield extracted from data ($\mu_{VH}^{bb} = 0.72$), and as an unstacked unfilled histogram, scaled by the SM prediction times a factor of two. The size of the combined on the sum of the fitted signal and background is shown in the hatched band. The highest bin contains the overflow.

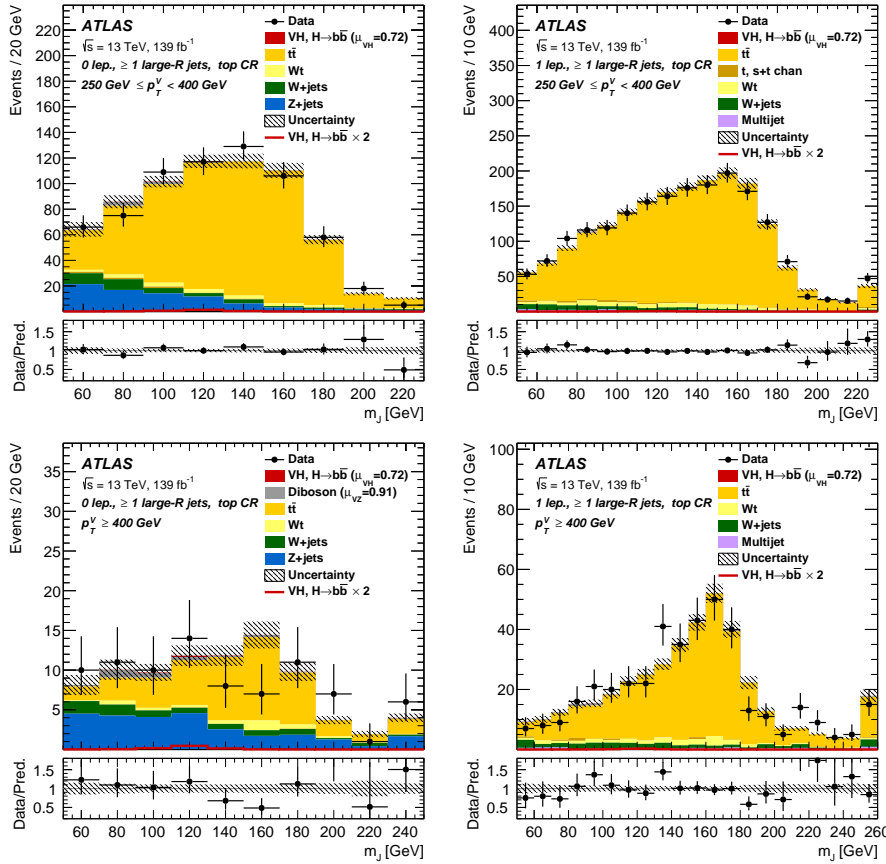


Figure 7.7: The m_J post-fit distributions in the $t\bar{t}$ control region for (top) the 0-lepton channel and the 1-lepton channel for $250 \text{ GeV} < p_T^V < 400 \text{ GeV}$ and (bottom) the 0-lepton channel and the 1-lepton channel for $p_T^V > 400 \text{ GeV}$. The background contributions after the likelihood fit are shown as filled histograms. The Higgs boson signal ($m_h = 125 \text{ GeV}$) is shown as a filled histogram on top of the fitted backgrounds normalised to the signal yield extracted from data ($\mu_{VH}^{bb} = 0.72$), and unstacked as an unfilled histogram, scaled by the SM prediction times a factor of 2. The size of the combined statistical and systematic uncertainty for the sum of the fitted signal and background is indicated by the hatched band. The highest bin in the distributions contains the overflow.

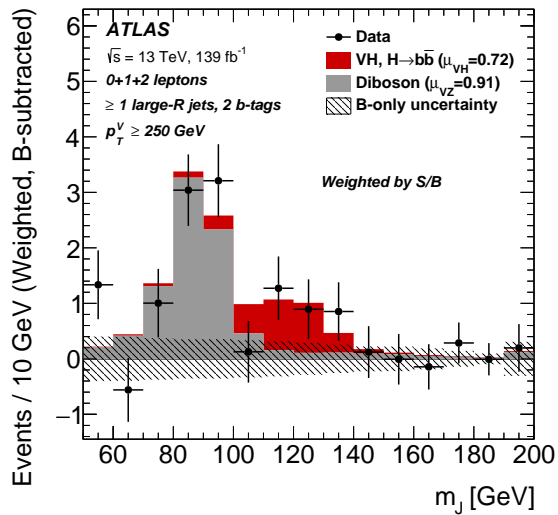


Figure 7.8: m_J distribution in data after subtraction of all backgrounds except for the WZ and ZZ diboson processes. The contributions from all lepton channels and signal regions are summed and weighted by their respective values of the ratio of fitted Higgs boson signal and background yields. The expected contribution of the associated WH and ZH production of a SM Higgs boson with $m_H = 125 \text{ GeV}$ is shown scaled by the measured combined signal strength ($\mu_{VH}^{bb} = 0.72$). The diboson contribution is normalised to its best-fit value of $\mu_{VZ}^{bb} = 0.91$. The size of the combined statistical and systematic uncertainty is indicated by the hatched band. This error band is computed from a full signal-plus-background fit including all the systematic uncertainties defined in Section 7.2, except for the VH/VZ experimental and theory uncertainties.

2452 **Compatability Studies**

2453 Alongside the standard 2-POI fit, a (3+1)-POI fit can be performed by splitting μ_{VH}^{bb}
2454 into three separate POIs, one for each channel. A simultaneous fit to the channel
2455 specific signal strengths can then be performned, which allows a comparison of the
2456 contributions from each channel. Fig. 7.9 compares the best-fit signal strengths.
2457 The 0- and 1-lepton channels show a signal strength which is consistent with the
2458 SM prediction, while the 2-lepton channel shows a small deviation within the 1σ
2459 uncertainty. Overall, good compatibility is observed via a χ^2 test with a corresponding
2460 p -value of 49%.

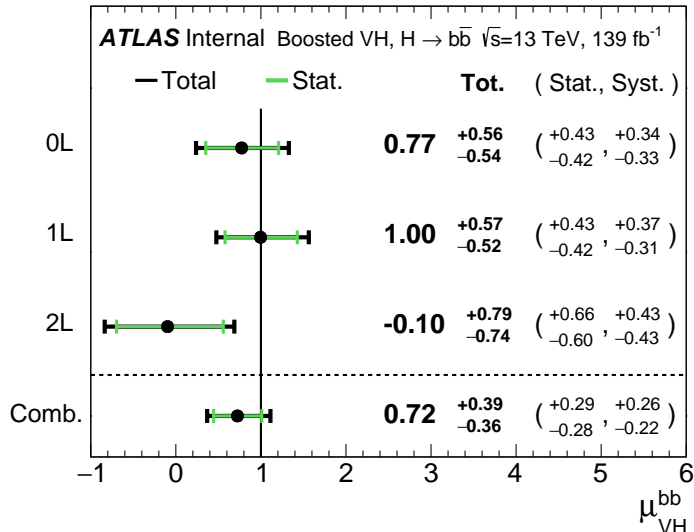


Figure 7.9: Signal strength compatibility test between the (3+1)-POI fit (with the three lepton channels splitted) and the default (1+1)-POI fit. The compatibility of the three channels is evaluated via a χ^2 difference test and results in a p -value of 49%.

2461 **7.4.3 Impact of Systematics**

2462 The impact of systematic uncertainties on the final fitted value $\hat{\mu}_{VH}^{bb}$ is studied looking
2463 at the NP rankings, and the uncertainty breakdown.

2464 Fig. 7.10 shows the NP ranking, which is used to visualise which out of the many
2465 NPs involved in the fit have the largest impact on the sensitivity to the fitted POI.
2466 To obtain the ranking, a likelihood scan is performed for each NP θ_j . First, an

2467 unconditional fit is used to determine $\hat{\theta}_j$. From this best-fit point, the NP is varied
2468 in steps and the likelihood is recomputed until the $\pm 1\sigma_{\hat{\theta}_j}$ values are reached. For
2469 each corresponding value of θ_j , the change in the best-fit value of the POI, $\Delta\hat{\mu}_{VH}^{bb}$
2470 is calculated and used to rank the NPs. Also shown in Fig. 7.10 are the pulls and
2471 constraints for the highest ranked NPs.

2472 The experimental uncertainty on the signal large- R jet mass resolution (JMR) has
2473 the largest impact of any NP. It is a significant contributor to the overall uncertainty
2474 on μ_{VH}^{bb} in Eq. (7.7). JMR and jet energy scale (JES) uncertainties also have impacts
2475 for the $V+jets$ background and for the diboson background. The freely-floating
2476 $Z+hf$ normalisation is the second highest ranked NP, and is heavily constrained by
2477 the fit. The VZ POI μ_{VZ}^{bb} is also a significant NP when considering the primary μ_{VH}^{bb}
2478 measurement.

2479 The NP ranking highlights individual NPs which have a large impact on the POI
2480 measurement sensitivity. Complementary information is provided at a higher level
2481 by considering the overall impact of different groups of systematics. The groups
2482 are constructed from NPs which have similar physical origin. The impact on each
2483 group is calculated by running a fit with all the NPs in the given group fixed to their
2484 nominal values. The uncertainty on the POI extracted from this fit is subtracted
2485 in quadrature from the the uncertainty on the POI from the nominal fit, and the
2486 resulting values are provided as the impact for each group. The full breakdown
2487 for the observed impact of uncertainties on the μ_{VH}^{bb} signal strength is provided in
2488 Table 7.12. The total systematic impact is the difference in quadrature between the
2489 nominal uncertainty on μ_{VH}^{bb} and the combined statistical impact. The “data stat
2490 only” group fixes all NPs at their nominal value, while the total statistical impact
2491 fixes all NPs except floating normalisations. The floating normalisations group fixes
2492 only the NPs associated with normalisation which are left floating in the fit. The
2493 uncertainty on μ_{VH}^{bb} is dominated by combined statistcal effects (0.28), although the
2494 combined impact of systematics (0.24) is of a comparable size. The signal largest
2495 group is the data stat uncertainty (0.25), demonstrating that the analysis would
2496 benefit from an increased integrated luminosity or improved efficiency to select signal
2497 relevant events (recall from Section 7.1.3 the signal efficiency is in the range of
2498 10%). Of the experimental systematic sources of uncertainty, the dominant impact
2499 is the experimental uncertainties associated with the reconstruction of large- R jets
2500 (0.13). Other experimental sources of uncertainty are small in comparison. Modelling

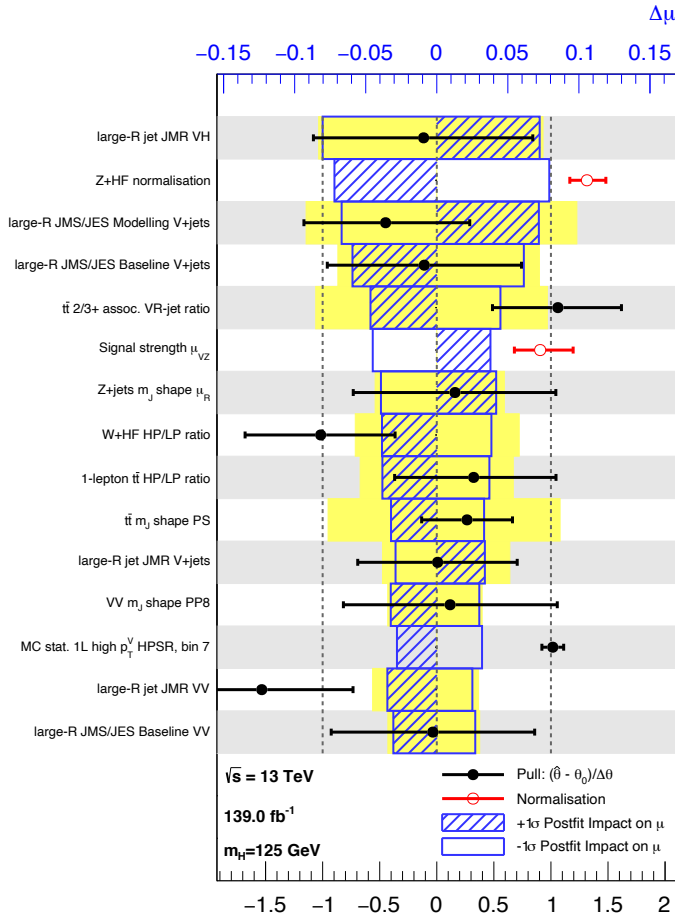


Figure 7.10: Impact of systematic uncertainties on the fitted VH signal-strength parameter $\hat{\mu}_{VH}^{bb}$ sorted in decreasing order. The boxes show the variations of $\hat{\mu}$, referring to the top x -axis, when fixing the corresponding individual nuisance parameter to its post-fit value modified upwards or downwards by its post-fit uncertainty, i.e. $\hat{\theta} \pm \sigma_{\hat{\theta}}$, and repeating the fit. The impact of up- and down-variations can be distinguished via the dashed and plane box fillings. The yellow boxes show the pre-fit impact (top x -axis) by varying each nuisance parameter by ± 1 . The filled circles show the deviation of the fitted value for each nuisance parameter, $\hat{\theta}$, from their nominal input value θ_0 expressed in standard deviations with respect to their nominal uncertainties $\Delta\theta$ (bottom x -axis). The error bars show the post-fit uncertainties on $\hat{\theta}$ with respect to their nominal uncertainties. The open circles show the fitted values and uncertainties of the normalization parameters that are freely floating in the fit. Pre-fit, these parameters have a value of one.

2501 uncertainties also have a large contribution to the overall systematic uncertainty. The
2502 biggest contribution to the overall uncertainty is the combined statistical uncertainty
2503 on the simulated samples (0.09), which contain only a finite number of events. Out of
2504 the backgrounds, the $W+jets$ and $Z+jets$ have the highest (0.06) and second-highest
2505 (0.05) impact respectively.

2506 **7.5 Improved b -tagging using GNNs**

2507 **7.6 Conclusion**

2508 Work has been carried out as part of the boosted VHbb analysis group to understand,
2509 and implement in the global profile likelihood fit, systematic uncertainties on $V+jets$
2510 samples. This background modelling work is an essential part of the success of
2511 the analysis. So far the fit has proved stable with the inclusion of the $V+jets$
2512 uncertainties, and detailed studies are now underway to determine the causes behind
2513 any observed pulls of the added NPs. Additional work is ongoing to help with the
2514 derivation of uncertainties on diboson samples, another important background. The
2515 analysis is already advanced, and is now progressing into its final stages. Publication
2516 is expected in the new year.

2517 This analysis would benefit greatly from the improved high p_T b -tagging enabled by
2518 GN1.

Source of uncertainty	Signed impact	Avg. impact
Total	+0.388 / -0.356	0.372
Statistical	+0.286 / -0.280	0.283
↔ Data stat only	+0.251 / -0.245	0.248
↔ Floating normalisations	+0.096 / -0.092	0.094
Systematic	+0.261 / -0.219	0.240
<hr/>		
Experimental uncertainties		
small-R jets	+0.041 / -0.034	0.038
large-R jets	+0.161 / -0.105	0.133
E_T^{miss}	+0.008 / -0.007	0.007
Leptons	+0.013 / -0.007	0.010
<i>b</i> -tagging	<i>b</i> -jets	+0.028 / -0.004
	<i>c</i> -jets	+0.012 / -0.011
	light-flavour jets	+0.009 / -0.007
	extrapolation	+0.004 / -0.005
Pile-up	+0.001 / -0.002	0.001
Luminosity	+0.019 / -0.007	0.013
<hr/>		
Theoretical and modelling uncertainties		
Signal	+0.073 / -0.026	0.050
Backgrounds	+0.106 / -0.095	0.100
↔ $Z + \text{jets}$	+0.049 / -0.047	0.048
↔ $W + \text{jets}$	+0.059 / -0.056	0.058
↔ $t\bar{t}$	+0.037 / -0.032	0.035
↔ Single top quark	+0.031 / -0.023	0.027
↔ Diboson	+0.034 / -0.029	0.032
↔ Multijet	+0.009 / -0.009	0.009
↔ MC statistical	+0.091 / -0.092	0.092

Table 7.12: Breakdown of the observed absolute contributions to the uncertainty on the signal strength μ_{VH}^{bb} obtained from the (1+1)-POI fit. The average impact represents the average between the positive and negative uncertainties on μ_{VH}^{bb} . The sum in quadrature of the systematic uncertainties attached to the categories differs from the total systematic uncertainty due to correlations.

₂₅₁₉ Chapter 8

₂₅₂₀ Conclusion

₂₅₂₁ flavour tagging at high pT is important because

₂₅₂₂ tracking suffers from several problems which might be improved by

₂₅₂₃ algorithmic gains in flavour tagging can improve things

₂₅₂₄ ultimately analyses will benefit greatly

₂₅₂₅ future work:

₂₅₂₆ • improve tracking

₂₅₂₇ • use more info for flavour tagging

₂₅₂₈ • improve jet labelling

₂₅₂₉ • boosted xbb tagging

₂₅₃₀ • lead to dihiggs

2531 Bibliography

- 2532 [1] A. Buckley, *A class for typesetting academic theses*, (2010). <http://ctan.tug.org/tex-archive/macros/latex/contrib/heptesis/heptesis.pdf>.
- 2533
- 2534 [2] L. Morel, Z. Yao, P. Cladé and S. Guellati-Khélifa, *Determination of the fine-structure constant with an accuracy of 81 parts per trillion*, *Nature* **588** (2020) pp. 61–65.
- 2535
- 2536
- 2537 [3] T. Sailer, V. Debierre, Z. Harman, F. Heiße, C. König, J. Morgner et al., *Measurement of the bound-electron g-factor difference in coupled ions*, *Nature* **606** (2022) pp. 479–483.
- 2538
- 2539
- 2540 [4] CDF collaboration, *Observation of top quark production in $\bar{p}p$ collisions*, *Phys. Rev. Lett.* **74** (1995) pp. 2626–2631 [[hep-ex/9503002](#)].
- 2541
- 2542 [5] D0 collaboration, *Observation of the top quark*, *Phys. Rev. Lett.* **74** (1995) pp. 2632–2637 [[hep-ex/9503003](#)].
- 2543
- 2544 [6] S. W. Herb et al., *Observation of a Dimuon Resonance at 9.5-GeV in 400-GeV Proton-Nucleus Collisions*, *Phys. Rev. Lett.* **39** (1977) pp. 252–255.
- 2545
- 2546 [7] UA1 collaboration, *Experimental Observation of Isolated Large Transverse Energy Electrons with Associated Missing Energy at $\sqrt{s} = 540$ GeV*, *Phys. Lett. B* **122** (1983) pp. 103–116.
- 2547
- 2548
- 2549 [8] DONUT collaboration, *Observation of tau neutrino interactions*, *Phys. Lett. B* **504** (2001) pp. 218–224 [[hep-ex/0012035](#)].
- 2550
- 2551 [9] F. Englert and R. Brout, *Broken Symmetry and the Mass of Gauge Vector Mesons*, *Phys. Rev. Lett.* **13** (1964) pp. 321–323.
- 2552
- 2553 [10] P. W. Higgs, *Broken Symmetries and the Masses of Gauge Bosons*, *Phys. Rev. Lett.* **13** (1964) pp. 508–509.
- 2554
- 2555 [11] G. S. Guralnik, C. R. Hagen and T. W. B. Kibble, *Global Conservation Laws and*

- 2556 *Massless Particles*, *Phys. Rev. Lett.* **13** (1964) pp. 585–587.
- 2557 [12] ATLAS Collaboration, *Observation of a new particle in the search for the Standard
2558 Model Higgs boson with the ATLAS detector at the LHC*, *Phys. Lett. B* **716** (2012)
2559 p. 1 [[1207.7214](#)].
- 2560 [13] CMS Collaboration, *Observation of a new boson at a mass of 125 GeV with the CMS
2561 experiment at the LHC*, *Phys. Lett. B* **716** (2012) p. 30 [[1207.7235](#)].
- 2562 [14] Particle Data Group collaboration, *Review of Particle Physics*, *PTEP* **2022** (2022)
2563 p. 083C01.
- 2564 [15] C. N. Yang and R. L. Mills, *Conservation of isotopic spin and isotopic gauge
2565 invariance*, *Phys. Rev.* **96** (1954) pp. 191–195.
- 2566 [16] S. L. Glashow, *Partial Symmetries of Weak Interactions*, *Nucl. Phys.* **22** (1961)
2567 pp. 579–588.
- 2568 [17] S. Weinberg, *A Model of Leptons*, *Phys. Rev. Lett.* **19** (1967) pp. 1264–1266.
- 2569 [18] A. Salam, *Weak and Electromagnetic Interactions*, *Proceedings of the 8th Nobel
2570 symposium*, Ed. N. Svartholm, Almqvist & Wiksell, 1968, **Conf. Proc. C680519**
2571 (1968) pp. 367–377.
- 2572 [19] T. D. Lee and C. N. Yang, *Question of parity conservation in weak interactions*,
2573 *Phys. Rev.* **104** (1956) pp. 254–258.
- 2574 [20] C. S. Wu, E. Ambler, R. W. Hayward, D. D. Hoppes and R. P. Hudson, *Experimental
2575 test of parity conservation in beta decay*, *Phys. Rev.* **105** (1957) pp. 1413–1415.
- 2576 [21] R. L. Garwin, L. M. Lederman and M. Weinrich, *Observations of the failure of
2577 conservation of parity and charge conjugation in meson decays: the magnetic moment
2578 of the free muon*, *Phys. Rev.* **105** (1957) pp. 1415–1417.
- 2579 [22] Y. Nambu, *Quasi-particles and gauge invariance in the theory of superconductivity*,
2580 *Phys. Rev.* **117** (1960) pp. 648–663.
- 2581 [23] J. Goldstone, *Field theories with «superconductor» solutions*, *Il Nuovo Cimento
2582 (1955-1965)* **19** (1961) pp. 154–164.
- 2583 [24] LHC Higgs Cross Section Working Group collaboration, *Handbook of LHC Higgs
2584 Cross Sections: 4. Deciphering the Nature of the Higgs Sector*, [1610.07922](#).
- 2585 [25] ATLAS Collaboration, *Observation of $H \rightarrow b\bar{b}$ decays and VH production with the*

- 2586 *ATLAS detector*, ATLAS-CONF-2018-036 (2018).
- 2587 [26] CMS Collaboration, *Observation of Higgs Boson Decay to Bottom Quarks*, *Phys.*
2588 *Rev. Lett.* **121** (2018) p. 121801 [[1808.08242](https://arxiv.org/abs/1808.08242)].
- 2589 [27] L. Evans and P. Bryant, *LHC Machine*, *JINST* **3** (2008) p. S08001.
- 2590 [28] The ALICE Collaboration, *The ALICE experiment at the CERN LHC*, *Journal of*
2591 *Instrumentation* **3** (2008) pp. S08002–S08002.
- 2592 [29] CMS Collaboration, *The CMS experiment at the CERN LHC*, *JINST* **3** (2008)
2593 p. S08004.
- 2594 [30] The LHCb Collaboration, *The LHCb detector at the LHC*, *Journal of*
2595 *Instrumentation* **3** (2008) pp. S08005–S08005.
- 2596 [31] ATLAS Collaboration, *The ATLAS Experiment at the CERN Large Hadron Collider*,
2597 *JINST* **3** (2008) p. S08003.
- 2598 [32] ATLAS Collaboration, *Integrated luminosity summary plots for 2011-2012 data*
2599 *taking*, (2022). <https://twiki.cern.ch/twiki/bin/view/AtlasPublic/LuminosityPublicResults>.
- 2600 [33] ATLAS Collaboration, *Public ATLAS Luminosity Results for Run-2 of the LHC*,
2601 (2022). <https://twiki.cern.ch/twiki/bin/view/AtlasPublic/LuminosityPublicResultsRun2>.
- 2602 [34] CERN, “The accelerator complex.” (2012).
- 2603 [35] G. C. Strong, *On the impact of selected modern deep-learning techniques to the*
2604 *performance and celerity of classification models in an experimental high-energy*
2605 *physics use case*, [2002.01427](https://arxiv.org/abs/2002.01427).
- 2606 [36] ATLAS Collaboration, *Atlas track reconstruction – general overview*, (2022).
2607 <https://atlassoftwaredocs.web.cern.ch/trackingTutorial/idoverview/>.
- 2608 [37] ATLAS Collaboration, *Performance of b-jet identification in the ATLAS experiment*,
2609 *JINST* **11** (2016) p. P04008 [[1512.01094](https://arxiv.org/abs/1512.01094)].
- 2610 [38] ATLAS Collaboration, *Luminosity determination in pp collisions at $\sqrt{s} = 13$ TeV*
2611 *using the ATLAS detector at the LHC*, ATLAS-CONF-2019-021 (2019).
- 2612 [39] ATLAS Collaboration, *ATLAS Detector and Physics Performance: Technical Design*
2613 *Report, Volume 1*, .

- 2616 [40] for the ATLAS Collaboration collaboration, *Status of the ATLAS Experiment*, Tech.
2617 Rep., Geneva (2010). 10.3204/DESY-PROC-2010-04/1.
- 2618 [41] ATLAS Collaboration, *ATLAS Inner Tracker Pixel Detector: Technical Design
2619 Report*, ATLAS-TDR-030; CERN-LHCC-2017-021 (2017).
- 2620 [42] ATLAS Collaboration, *ATLAS Inner Tracker Strip Detector: Technical Design
2621 Report*, ATLAS-TDR-025; CERN-LHCC-2017-005 (2017).
- 2622 [43] ATLAS Collaboration, *The inner detector*, (2022).
<https://atlas.cern/Discover/Detector/Inner-Detector>.
- 2624 [44] ATLAS Collaboration, *ATLAS Insertable B-Layer: Technical Design Report*,
2625 ATLAS-TDR-19; CERN-LHCC-2010-013 (2010).
- 2626 [45] B. Abbott et al., *Production and integration of the ATLAS Insertable B-Layer*,
2627 *JINST* **13** (2018) p. T05008 [[1803.00844](#)].
- 2628 [46] ATLAS Collaboration, *Operation and performance of the ATLAS semiconductor
2629 tracker*, *JINST* **9** (2014) p. P08009 [[1404.7473](#)].
- 2630 [47] ATLAS Collaboration, *Calorimeter*, (2022).
<https://atlas.cern/Discover/Detector/Calorimeter>.
- 2632 [48] ATLAS Collaboration, *ATLAS Tile Calorimeter: Technical Design Report*, .
- 2633 [49] G. Artoni, *Muon momentum scale and resolution in pp collisions at $\sqrt{s} = 8 \text{ TeV}$ in
2634 ATLAS*, Tech. Rep., Geneva (2016). 10.1016/j.nuclphysbps.2015.09.453.
- 2635 [50] ATLAS Collaboration, *Muon spectrometer*, (2022).
<https://atlas.cern/Discover/Detector/Muon-Spectrometer>.
- 2637 [51] ATLAS Collaboration, *Performance of the ATLAS trigger system in 2015*, *Eur.
2638 Phys. J. C* **77** (2017) p. 317 [[1611.09661](#)].
- 2639 [52] ATLAS Collaboration, *The ATLAS Collaboration Software and Firmware*, (2021).
- 2640 [53] T. Cornelissen, M. Elsing, S. Fleischmann, W. Liebig and E. Moyse, *Concepts,
2641 Design and Implementation of the ATLAS New Tracking (NEWT)*, .
- 2642 [54] ATLAS Collaboration, *The Optimization of ATLAS Track Reconstruction in Dense
2643 Environments*, ATL-PHYS-PUB-2015-006 (2015).
- 2644 [55] ATLAS Collaboration, *Performance of the ATLAS track reconstruction algorithms in
2645 dense environments in LHC Run 2*, *Eur. Phys. J. C* **77** (2017) p. 673 [[1704.07983](#)].

- 2646 [56] ATLAS Collaboration, *A neural network clustering algorithm for the ATLAS silicon*
2647 *pixel detector*, *JINST* **9** (2014) p. P09009 [[1406.7690](#)].
- 2648 [57] ATLAS Collaboration, *Reconstruction of primary vertices at the ATLAS experiment*
2649 *in Run 1 proton–proton collisions at the LHC*, *Eur. Phys. J. C* **77** (2017) p. 332
2650 [[1611.10235](#)].
- 2651 [58] ATLAS Collaboration, *Development of ATLAS Primary Vertex Reconstruction for*
2652 *LHC Run 3*, ATL-PHYS-PUB-2019-015 (2019).
- 2653 [59] ATLAS Collaboration, *ATLAS b-jet identification performance and efficiency*
2654 *measurement with $t\bar{t}$ events in pp collisions at $\sqrt{s} = 13$ TeV*, *Eur. Phys. J. C* **79**
2655 (2019) p. 970 [[1907.05120](#)].
- 2656 [60] M. Cacciari, G. P. Salam and G. Soyez, *The anti- k_t jet clustering algorithm*, *JHEP*
2657 **04** (2008) p. 063 [[0802.1189](#)].
- 2658 [61] M. Cacciari, G. P. Salam and G. Soyez, *Fastjet user manual*, *Eur. Phys. J. C* **72** (2012)
2659 p. 1896 [[1111.6097](#)].
- 2660 [62] ATLAS Collaboration, *Topological cell clustering in the ATLAS calorimeters and its*
2661 *performance in LHC Run 1*, *Eur. Phys. J. C* **77** (2017) p. 490 [[1603.02934](#)].
- 2662 [63] ATLAS Collaboration, *Jet reconstruction and performance using particle flow with*
2663 *the ATLAS Detector*, *Eur. Phys. J. C* **77** (2017) p. 466 [[1703.10485](#)].
- 2664 [64] ATLAS Collaboration, *Jet energy scale measurements and their systematic*
2665 *uncertainties in proton–proton collisions at $\sqrt{s} = 13$ TeV with the ATLAS detector*,
2666 *Phys. Rev. D* **96** (2017) p. 072002 [[1703.09665](#)].
- 2667 [65] J. M. Butterworth, A. R. Davison, M. Rubin and G. P. Salam, *Jet Substructure as a*
2668 *New Higgs Search Channel at the Large Hadron Collider*, *Phys. Rev. Lett.* **100** (2008)
2669 p. 242001 [[0802.2470](#)].
- 2670 [66] ATLAS collaboration, *Measurement of the associated production of a Higgs boson*
2671 *decaying into b-quarks with a vector boson at high transverse momentum in pp*
2672 *collisions at $\sqrt{s} = 13$ TeV with the ATLAS detector*, *Phys. Lett. B* **816** (2021)
2673 p. 136204 [[2008.02508](#)].
- 2674 [67] ATLAS collaboration, *Performance of jet substructure techniques for large-R jets in*
2675 *proton-proton collisions at $\sqrt{s} = 7$ TeV using the ATLAS detector*, *JHEP* **09** (2013)
2676 p. 076 [[1306.4945](#)].

- 2677 [68] ATLAS Collaboration, *In situ calibration of large-radius jet energy and mass in*
2678 *13 TeV proton–proton collisions with the ATLAS detector*, *Eur. Phys. J. C* **79** (2019)
2679 p. 135 [[1807.09477](#)].
- 2680 [69] D. Krohn, J. Thaler and L.-T. Wang, *Jets with Variable R*, *JHEP* **06** (2009) p. 059
2681 [[0903.0392](#)].
- 2682 [70] ATLAS Collaboration, *Variable Radius, Exclusive- k_T , and Center-of-Mass Subjet*
2683 *Reconstruction for Higgs($\rightarrow b\bar{b}$) Tagging in ATLAS*, ATL-PHYS-PUB-2017-010
2684 (2017).
- 2685 [71] ATLAS Collaboration, *Improved electron reconstruction in ATLAS using the*
2686 *Gaussian Sum Filter-based model for bremsstrahlung*, ATLAS-CONF-2012-047 (2012).
- 2687 [72] ATLAS Collaboration, *Electron efficiency measurements with the ATLAS detector*
2688 *using the 2015 LHC proton–proton collision data*, ATLAS-CONF-2016-024 (2016).
- 2689 [73] ATLAS Collaboration, *Muon reconstruction performance of the ATLAS detector in*
2690 *proton–proton collision data at $\sqrt{s} = 13$ TeV*, *Eur. Phys. J. C* **76** (2016) p. 292
2691 [[1603.05598](#)].
- 2692 [74] ATLAS Collaboration, *Performance of missing transverse momentum reconstruction*
2693 *with the ATLAS detector using proton–proton collisions at $\sqrt{s} = 13$ TeV*, *Eur. Phys.*
2694 *J. C* **78** (2018) p. 903 [[1802.08168](#)].
- 2695 [75] Nazar Bartosik, *Diagram showing the common principle of identification of jets*
2696 *initiated by b-hadron decays*, (2022).
2697 https://en.m.wikipedia.org/wiki/File:B-tagging_diagram.png.
- 2698 [76] B. R. Webber, *Fragmentation and hadronization*, *Int. J. Mod. Phys. A* **15S1** (2000)
2699 pp. 577–606 [[hep-ph/9912292](#)].
- 2700 [77] Particle Data Group collaboration, *Review of particle physics*, *Phys. Rev. D* **98**
2701 (2018) p. 030001.
- 2702 [78] A. Chen, M. Goldberg, N. Horwitz, A. Jawahery, P. Lipari, G. C. Moneti et al.,
2703 *Limit on the $b \rightarrow u$ coupling from semileptonic b decay*, *Phys. Rev. Lett.* **52** (1984)
2704 pp. 1084–1088.
- 2705 [79] ATLAS Collaboration, *Tracking efficiency studies in dense environments*, (2022).
2706 <https://atlas.web.cern.ch/Atlas/GROUPS/PHYSICS/PLLOTS/IDTR-2022-03/>.
- 2707 [80] R. Jansky, *Truth Seeded Reconstruction for Fast Simulation in the ATLAS*

- 2708 *Experiment*, .
- 2709 [81] E. Boos, M. Dobbs, W. Giele, I. Hinchliffe, J. Huston, V. Ilyin et al., *Generic User*
2710 *Process Interface for Event Generators*, ArXiv High Energy Physics - Phenomenology
2711 e-prints (2001) .
- 2712 [82] J. Alwall, A. Ballestrero, P. Bartalini, S. Belov, E. Boos, A. Buckley et al., *A*
2713 *standard format for Les Houches Event Files*, Computer Physics Communications
2714 **176** (2007) pp. 300–304.
- 2715 [83] K. Hornik, M. Stinchcombe and H. White, *Multilayer feedforward networks are*
2716 *universal approximators*, Neural Networks **2** (1989) pp. 359–366.
- 2717 [84] D. E. Rumelhart, G. E. Hinton and R. J. Williams, *Learning representations by*
2718 *back-propagating errors*, nature **323** (1986) pp. 533–536.
- 2719 [85] W. McCulloch and W. Pitts, *A logical calculus of the ideas immanent in nervous*
2720 *activity*, The bulletin of mathematical biophysics **5** (1943) pp. 115–133.
- 2721 [86] J. Hopfield, *Neural networks and physical systems with emergent collective*
2722 *computational abilities*, in *Spin Glass Theory and Beyond: An Introduction to the*
2723 *Replica Method and Its Applications*, pp. 411–415, World Scientific, (1987).
- 2724 [87] Y. A. LeCun, L. Bottou, G. B. Orr and K.-R. Müller, *Efficient backprop*, in *Neural*
2725 *networks: Tricks of the trade*, pp. 9–48, Springer, (2012).
- 2726 [88] D. P. Kingma and J. Ba, *Adam: A Method for Stochastic Optimization*, arXiv
2727 e-prints (2014) p. arXiv:1412.6980 [[1412.6980](#)].
- 2728 [89] P. Nason, *A new method for combining nlo qcd with shower monte carlo algorithms*,
2729 Journal of High Energy Physics **2004** (2004) p. 040–040.
- 2730 [90] S. Frixione, G. Ridolfi and P. Nason, *A positive-weight next-to-leading-order monte*
2731 *carlo for heavy flavour hadroproduction*, Journal of High Energy Physics **2007** (2007)
2732 p. 126–126.
- 2733 [91] S. Frixione, P. Nason and C. Oleari, *Matching nlo qcd computations with parton*
2734 *shower simulations: the powheg method*, Journal of High Energy Physics **2007** (2007)
2735 p. 070–070.
- 2736 [92] S. Alioli, P. Nason, C. Oleari and E. Re, *A general framework for implementing nlo*
2737 *calculations in shower monte carlo programs: the powheg box*, Journal of High Energy
2738 Physics **2010** (2010) .

- 2739 [93] NNPDF collaboration, *Parton distributions for the LHC run II*, *JHEP* **04** (2015)
2740 p. 040 [[1410.8849](#)].
- 2741 [94] ATLAS Collaboration, *Studies on top-quark Monte Carlo modelling for Top2016*,
2742 ATL-PHYS-PUB-2016-020 (2016).
- 2743 [95] T. Sjöstrand, S. Ask, J. R. Christiansen, R. Corke, N. Desai, P. Ilten et al., *An*
2744 *introduction to PYTHIA 8.2*, *Comput. Phys. Commun.* **191** (2015) p. 159
2745 [[1410.3012](#)].
- 2746 [96] ATLAS Collaboration, *ATLAS Pythia 8 tunes to 7 TeV data*,
2747 ATL-PHYS-PUB-2014-021 (2014).
- 2748 [97] R. D. Ball et al., *Parton distributions with LHC data*, *Nucl. Phys. B* **867** (2013)
2749 p. 244 [[1207.1303](#)].
- 2750 [98] D. J. Lange, *The EvtGen particle decay simulation package*, *Nucl. Instrum. Meth. A*
2751 **462** (2001) p. 152.
- 2752 [99] ATLAS Collaboration, *The ATLAS Simulation Infrastructure*, *Eur. Phys. J. C* **70**
2753 (2010) p. 823 [[1005.4568](#)].
- 2754 [100] GEANT4 Collaboration, S. Agostinelli et al., *GEANT4 – a simulation toolkit*, *Nucl.*
2755 *Instrum. Meth. A* **506** (2003) p. 250.
- 2756 [101] ATLAS Collaboration, *Tagging and suppression of pileup jets with the ATLAS*
2757 *detector*, ATL-CONF-2014-018 (2014).
- 2758 [102] ATLAS Collaboration, *Deep Sets based Neural Networks for Impact Parameter*
2759 *Flavour Tagging in ATLAS*, ATL-PHYS-PUB-2020-014 (2020).
- 2760 [103] ATLAS Collaboration, *Graph Neural Network Jet Flavour Tagging with the ATLAS*
2761 *Detector*, ATL-PHYS-PUB-2022-027 (2022).
- 2762 [104] ATLAS Collaboration, *Observation of $H \rightarrow b\bar{b}$ decays and VH production with the*
2763 *ATLAS detector*, *Phys. Lett. B* **786** (2018) p. 59 [[1808.08238](#)].
- 2764 [105] ATLAS Collaboration, *Observation of Higgs boson production in association with a*
2765 *top quark pair at the LHC with the ATLAS detector*, *Phys. Lett. B* **784** (2018) p. 173
2766 [[1806.00425](#)].
- 2767 [106] ATLAS Collaboration, *Search for new resonances in mass distributions of jet pairs*
2768 *using 139 fb^{-1} of pp collisions at $\sqrt{s} = 13\text{ TeV}$ with the ATLAS detector*, *JHEP* **03**
2769 (2020) p. 145 [[1910.08447](#)].

- 2770 [107] ATLAS Collaboration, *Optimisation and performance studies of the ATLAS*
2771 *b*-tagging algorithms for the 2017-18 LHC run, ATL-PHYS-PUB-2017-013 (2017).
- 2772 [108] ATLAS collaboration, *ATLAS flavour-tagging algorithms for the LHC Run 2 pp*
2773 *collision dataset*, [2211.16345](#).
- 2774 [109] J. Shlomi, S. Ganguly, E. Gross, K. Cranmer, Y. Lipman, H. Serviansky et al.,
2775 *Secondary vertex finding in jets with neural networks*, *The European Physical Journal*
2776 *C* **81** (2021) .
- 2777 [110] H. Serviansky, N. Segol, J. Shlomi, K. Cranmer, E. Gross, H. Maron et al.,
2778 *Set2Graph: Learning Graphs From Sets*, *arXiv e-prints* (2020) p. arXiv:2002.08772
2779 [[2002.08772](#)].
- 2780 [111] ATLAS Collaboration, *Secondary vertex finding for jet flavour identification with the*
2781 *ATLAS detector*, ATL-PHYS-PUB-2017-011 (2017).
- 2782 [112] ATLAS Collaboration, *Identification of Jets Containing b-Hadrons with Recurrent*
2783 *Neural Networks at the ATLAS Experiment*, ATL-PHYS-PUB-2017-003 (2017).
- 2784 [113] P. W. Battaglia, J. B. Hamrick, V. Bapst, A. Sanchez-Gonzalez, V. Zambaldi,
2785 M. Malinowski et al., *Relational inductive biases, deep learning, and graph networks*,
2786 *arXiv e-prints* (2018) p. arXiv:1806.01261 [[1806.01261](#)].
- 2787 [114] M. Zaheer, S. Kottur, S. Ravanbakhsh, B. Poczos, R. Salakhutdinov and A. Smola,
2788 *Deep Sets*, *arXiv e-prints* (2017) p. arXiv:1703.06114 [[1703.06114](#)].
- 2789 [115] ATLAS Collaboration, *Muon reconstruction performance in early $\sqrt{s} = 13$ TeV data*,
2790 ATL-PHYS-PUB-2015-037 (2015).
- 2791 [116] ATLAS Collaboration, *Electron reconstruction and identification in the ATLAS*
2792 *experiment using the 2015 and 2016 LHC proton–proton collision data at*
2793 *$\sqrt{s} = 13$ TeV*, *Eur. Phys. J. C* **79** (2019) p. 639 [[1902.04655](#)].
- 2794 [117] D. Hwang, J. Park, S. Kwon, K.-M. Kim, J.-W. Ha and H. J. Kim, *Self-supervised*
2795 *Auxiliary Learning with Meta-paths for Heterogeneous Graphs*, *arXiv e-prints* (2020)
2796 p. arXiv:2007.08294 [[2007.08294](#)].
- 2797 [118] S. Brody, U. Alon and E. Yahav, *How Attentive are Graph Attention Networks?*,
2798 *arXiv e-prints* (2021) p. arXiv:2105.14491 [[2105.14491](#)].
- 2799 [119] D. P. Kingma and J. Ba, *Adam: A Method for Stochastic Optimization*, *arXiv*
2800 *e-prints* (2014) p. arXiv:1412.6980 [[1412.6980](#)].

- 2801 [120] J. Bai, F. Lu, K. Zhang et al., *ONNX: Open neural network exchange*, (2019).
2802 <https://github.com/onnx/onnx>.
- 2803 [121] R. Lafaye, T. Plehn, M. Rauch, D. Zerwas and M. Duhrssen, *Measuring the Higgs*
2804 *Sector*, *JHEP* **08** (2009) p. 009 [[0904.3866](#)].
- 2805 [122] ATLAS Collaboration, *Measurement of the associated production of a Higgs boson*
2806 *decaying into b-quarks with a vector boson at high transverse momentum in pp*
2807 *collisions at $\sqrt{s} = 13$ TeV with the ATLAS detector*, *Phys. Lett. B* **816** (2021)
2808 p. 136204 [[2008.02508](#)].
- 2809 [123] K. Mimasu, V. Sanz and C. Williams, *Higher order QCD predictions for associated*
2810 *Higgs production with anomalous couplings to gauge bosons*, *JHEP* **08** (2016) p. 039
2811 [[1512.02572](#)].
- 2812 [124] ATLAS Collaboration, *Performance of jet substructure techniques for large-R jets in*
2813 *proton–proton collisions at $\sqrt{s} = 7$ TeV using the ATLAS detector*, *JHEP* **09** (2013)
2814 p. 076 [[1306.4945](#)].
- 2815 [125] S. Alioli, P. Nason, C. Oleari and E. Re, *A general framework for implementing NLO*
2816 *calculations in shower Monte Carlo programs: the POWHEG BOX*, *JHEP* **06** (2010)
2817 p. 043 [[1002.2581](#)].
- 2818 [126] ATLAS collaboration, *Measurement of the Z/γ^* boson transverse momentum*
2819 *distribution in pp collisions at $\sqrt{s} = 7$ TeV with the ATLAS detector*, *JHEP* **09**
2820 (2014) p. 145 [[1406.3660](#)].
- 2821 [127] G. Cullen, N. Greiner, G. Heinrich, G. Luisoni, P. Mastrolia, G. Ossola et al.,
2822 *Automated one-loop calculations with GoSam*, *Eur. Phys. J. C* **72** (2012) p. 1889
2823 [[1111.2034](#)].
- 2824 [128] K. Hamilton, P. Nason and G. Zanderighi, *MINLO: multi-scale improved NLO*,
2825 *JHEP* **10** (2012) p. 155 [[1206.3572](#)].
- 2826 [129] G. Luisoni, P. Nason, C. Oleari and F. Tramontano, *$HW^\pm/HZ + 0$ and 1 jet at*
2827 *NLO with the POWHEG BOX interfaced to GoSam and their merging within*
2828 *MinLO*, *JHEP* **10** (2013) p. 083 [[1306.2542](#)].
- 2829 [130] M. L. Ciccolini, S. Dittmaier and M. Krämer, *Electroweak radiative corrections to*
2830 *associated WH and ZH production at hadron colliders*, *Phys. Rev. D* **68** (2003)
2831 p. 073003 [[hep-ph/0306234](#)].
- 2832 [131] O. Brein, A. Djouadi and R. Harlander, *NNLO QCD corrections to the*

- 2833 *Higgs-strahlung processes at hadron colliders*, *Phys. Lett. B* **579** (2004) pp. 149–156
2834 [[hep-ph/0307206](#)].
- 2835 [132] G. Ferrera, M. Grazzini and F. Tramontano, *Associated Higgs-W-Boson Production*
2836 *at Hadron Colliders: a Fully Exclusive QCD Calculation at NNLO*, *Phys. Rev. Lett.*
2837 **107** (2011) p. 152003 [[1107.1164](#)].
- 2838 [133] O. Brein, R. V. Harlander, M. Wiesemann and T. Zirke, *Top-quark mediated effects*
2839 *in hadronic Higgs-Strahlung*, *Eur. Phys. J. C* **72** (2012) p. 1868 [[1111.0761](#)].
- 2840 [134] G. Ferrera, M. Grazzini and F. Tramontano, *Higher-order QCD effects for associated*
2841 *WH production and decay at the LHC*, *JHEP* **04** (2014) p. 039 [[1312.1669](#)].
- 2842 [135] G. Ferrera, M. Grazzini and F. Tramontano, *Associated ZH production at hadron*
2843 *colliders: The fully differential NNLO QCD calculation*, *Phys. Lett. B* **740** (2015)
2844 pp. 51–55 [[1407.4747](#)].
- 2845 [136] J. M. Campbell, R. K. Ellis and C. Williams, *Associated production of a Higgs boson*
2846 *at NNLO*, *JHEP* **06** (2016) p. 179 [[1601.00658](#)].
- 2847 [137] L. Altenkamp, S. Dittmaier, R. V. Harlander, H. Rzehak and T. J. E. Zirke,
2848 *Gluon-induced Higgs-strahlung at next-to-leading order QCD*, *JHEP* **02** (2013) p. 078
2849 [[1211.5015](#)].
- 2850 [138] B. Hespel, F. Maltoni and E. Vryonidou, *Higgs and Z boson associated production via*
2851 *gluon fusion in the SM and the 2HDM*, *JHEP* **06** (2015) p. 065 [[1503.01656](#)].
- 2852 [139] R. V. Harlander, A. Kulesza, V. Theeuwes and T. Zirke, *Soft gluon resummation for*
2853 *gluon-induced Higgs Strahlung*, *JHEP* **11** (2014) p. 082 [[1410.0217](#)].
- 2854 [140] R. V. Harlander, S. Liebler and T. Zirke, *Higgs Strahlung at the Large Hadron*
2855 *Collider in the 2-Higgs-doublet model*, *JHEP* **02** (2014) p. 023 [[1307.8122](#)].
- 2856 [141] O. Brein, R. V. Harlander and T. J. E. Zirke, *vh@nnlo – Higgs Strahlung at hadron*
2857 *colliders*, *Comput. Phys. Commun.* **184** (2013) pp. 998–1003 [[1210.5347](#)].
- 2858 [142] S. Frixione, G. Ridolfi and P. Nason, *A positive-weight next-to-leading-order Monte*
2859 *Carlo for heavy flavour hadroproduction*, *JHEP* **09** (2007) p. 126 [[0707.3088](#)].
- 2860 [143] M. Czakon and A. Mitov, *Top++: A program for the calculation of the top-pair*
2861 *cross-section at hadron colliders*, *Comput. Phys. Commun.* **185** (2014) p. 2930
2862 [[1112.5675](#)].
- 2863 [144] S. Alioli, P. Nason, C. Oleari and E. Re, *NLO single-top production matched with*

- 2864 *shower in POWHEG: s- and t-channel contributions*, *JHEP* **09** (2009) p. 111
2865 [[0907.4076](#)].
- 2866 [145] N. Kidonakis, *Next-to-next-to-leading logarithm resummation for s-channel single top*
2867 *quark production*, *Phys. Rev. D* **81** (2010) p. 054028 [[1001.5034](#)].
- 2868 [146] N. Kidonakis, *Next-to-next-to-leading-order collinear and soft gluon corrections for*
2869 *t-channel single top quark production*, *Phys. Rev. D* **83** (2011) p. 091503 [[1103.2792](#)].
- 2870 [147] E. Re, *Single-top Wt-channel production matched with parton showers using the*
2871 *POWHEG method*, *Eur. Phys. J. C* **71** (2011) p. 1547 [[1009.2450](#)].
- 2872 [148] N. Kidonakis, *Two-loop soft anomalous dimensions for single top quark associated*
2873 *production with a W^- or H^-* , *Phys. Rev. D* **82** (2010) p. 054018 [[1005.4451](#)].
- 2874 [149] T. Gleisberg, S. Höche, F. Krauss, M. Schönherr, S. Schumann, F. Siegert et al.,
2875 *Event generation with SHERPA 1.1*, *JHEP* **02** (2009) p. 007 [[0811.4622](#)].
- 2876 [150] E. Bothmann et al., *Event generation with Sherpa 2.2*, *SciPost Phys.* **7** (2019) p. 034
2877 [[1905.09127](#)].
- 2878 [151] F. Cascioli, P. Maierhöfer and S. Pozzorini, *Scattering Amplitudes with Open Loops*,
2879 *Phys. Rev. Lett.* **108** (2012) p. 111601 [[1111.5206](#)].
- 2880 [152] T. Gleisberg and S. Höche, *Comix, a new matrix element generator*, *JHEP* **12** (2008)
2881 p. 039 [[0808.3674](#)].
- 2882 [153] S. Schumann and F. Krauss, *A parton shower algorithm based on Catani–Seymour*
2883 *dipole factorisation*, *JHEP* **03** (2008) p. 038 [[0709.1027](#)].
- 2884 [154] S. Höche, F. Krauss, M. Schönherr and F. Siegert, *QCD matrix elements + parton*
2885 *showers. The NLO case*, *JHEP* **04** (2013) p. 027 [[1207.5030](#)].
- 2886 [155] S. Catani, L. Cieri, G. Ferrera, D. de Florian and M. Grazzini, *Vector Boson*
2887 *Production at Hadron Colliders: a Fully Exclusive QCD Calculation at NNLO*, *Phys.*
2888 *Rev. Lett.* **103** (2009) p. 082001 [[0903.2120](#)].
- 2889 [156] J. Butterworth et al., *PDF4LHC recommendations for LHC Run II*, *J. Phys. G* **43**
2890 (2016) p. 023001 [[1510.03865](#)].
- 2891 [157] A. Denner, S. Dittmaier, S. Kallweit and A. Mück, *Electroweak corrections to*
2892 *Higgs-strahlung off W/Z bosons at the Tevatron and the LHC with Hawk*, *JHEP* **03**
2893 (2012) p. 075 [[1112.5142](#)].

- 2894 [158] A. Denner, S. Dittmaier, S. Kallweit and A. Mück, *HAWK 2.0: A Monte Carlo*
2895 *program for Higgs production in vector-boson fusion and Higgs strahlung at hadron*
2896 *colliders*, *Comput. Phys. Commun.* **195** (2015) pp. 161–171 [[1412.5390](#)].
- 2897 [159] ATLAS Collaboration, *Expected performance of the ATLAS b-tagging algorithms in*
2898 *Run-2*, ATL-PHYS-PUB-2015-022 (2015).
- 2899 [160] ATLAS Collaboration, *Measurements of b-jet tagging efficiency with the ATLAS*
2900 *detector using $t\bar{t}$ events at $\sqrt{s} = 13$ TeV*, *JHEP* **08** (2018) p. 089 [[1805.01845](#)].
- 2901 [161] ATLAS Collaboration, *Calibration of light-flavour b-jet mistagging rates using*
2902 *ATLAS proton–proton collision data at $\sqrt{s} = 13$ TeV*, ATLAS-CONF-2018-006
2903 (2018).
- 2904 [162] ATLAS Collaboration, *Measurement of b-tagging efficiency of c-jets in $t\bar{t}$ events using*
2905 *a likelihood approach with the ATLAS detector*, ATLAS-CONF-2018-001 (2018).
- 2906 [163] ATLAS Collaboration, *Flavor Tagging with Track-Jets in Boosted Topologies with the*
2907 *ATLAS Detector*, ATL-PHYS-PUB-2014-013 (2014).
- 2908 [164] ATLAS Collaboration, *Identification of boosted Higgs bosons decaying into b-quark*
2909 *pairs with the ATLAS detector at 13 TeV*, *Eur. Phys. J. C* **79** (2019) p. 836
2910 [[1906.11005](#)].
- 2911 [165] L. A. Harland-Lang, A. D. Martin, P. Motylinski and R. S. Thorne, *Parton*
2912 *distributions in the LHC era: MMHT 2014 PDFs*, *Eur. Phys. J. C* **75** (2015) p. 204
2913 [[1412.3989](#)].
- 2914 [166] S. Dulat, T.-J. Hou, J. Gao, M. Guzzi, J. Huston, P. Nadolsky et al., *New parton*
2915 *distribution functions from a global analysis of quantum chromodynamics*, *Phys. Rev.*
2916 **D93** (2016) p. 033006 [[1506.07443](#)].
- 2917 [167] J. K. Anders and M. D’Onofrio, *V+Jets theoretical uncertainties estimation via a*
2918 *parameterisation method*, Tech. Rep. ATL-COM-PHYS-2016-044, Geneva (2016).
- 2919 [168] J. Pumplin et al., *New generation of parton distributions with uncertainties from*
2920 *global qcd analysis*, *JHEP* **07** (2002) p. 012 [[0201195](#)].
- 2921 [169] L. Moneta, K. Belasco, K. Cranmer, S. Kreiss, A. Lazzaro, D. Piparo et al., *The*
2922 *roostats project*, arXiv preprint arXiv:1009.1003 (2010) .

2923 List of figures

<small>2924</small>	2.1 The Higgs potential $V(\phi)$ of the complex scalar field singlet $\phi = \phi_1 + i\phi_2$, with a choice of $\mu^2 < 0$ leading to a continuous degeneracy in the true vacuum states. A false vacuum is present at the origin. The SM Higgs mechanism relies on a complex scalar doublet with a corresponding 5-dimensional potential.	19
<small>2925</small>		
<small>2926</small>		
<small>2927</small>		
<small>2928</small>		
<small>2929</small>	2.2 Diagrams for the four main Higgs boson production modes at the LHC for a Higgs mass $m_H = 125$ GeV at a centre of mass energy $\sqrt{s} = 13$ TeV.	25
<small>2930</small>		
<small>2931</small>	2.3 Higgs boson production cross sections as a function of Higgs mass (m_H) at $\sqrt{s} = 13$ TeV [24]. Uncertainties are shown in the shaded bands. At $m_H = 125$ GeV, Higgs boson production is dominated by gluon-gluon fusion, vector boson fusion, associated production with vector bosons, and top quark fusion.	25
<small>2932</small>		
<small>2933</small>		
<small>2934</small>		
<small>2935</small>		
<small>2936</small>	2.4 Higgs boson branching ratios as a function of Higgs mass (m_H) at $\sqrt{s} = 13$ TeV [24]. Uncertainties are shown in the shaded bands. At $m_H = 125$ GeV, the Higgs predominantly decays to a pair of b -quarks, around 58% of the time. The leading subdominant decay mode is to a pair of W bosons.	26
<small>2937</small>		
<small>2938</small>		
<small>2939</small>		
<small>2940</small>	3.1 An overview of the CERN accelerator complex [34]. The LHC is fed by a series of accelerators starting with Linac4. Next are the Proton Synchrotron Booster, the Proton Synchrotron, and finally the Super Proton Synchrotron which injects protons into the LHC.	29
<small>2941</small>		
<small>2942</small>		
<small>2943</small>		
<small>2944</small>	3.2 The coordinate system used at the ATLAS detector, showing the locations of the four main experiments located at various points around the LHC. The 3-vector momentum $\mathbf{p} = (p_x, p_y, p_z)$ is shown by the red arrow. Reproduced from Ref. [35].	30
<small>2945</small>		
<small>2946</small>		
<small>2947</small>		

2948	3.3 The track parameterisation used at the ATLAS detector. Five coordinates ($d_0, z_0, \phi, \theta, q/p$) are specified, defined at the track's point of closest approach to the nominal interaction point at the origin of the coordinate system. The figure shows the three-momentum \mathbf{p} and the transverse momentum p_T (defined in Eq. (3.2)). The basis vectors e_x , e_y and e_z are also shown. Reproduced from Ref. [36].	32
2954	3.4 Delivered, recorded, and usable integrated luminosity as a function of time over the course of Run 2 [33]. A total of 139 fb^{-1} of collision data is labelled as good for physics, meaning all sub-detector systems were operating nominally.	34
2958	3.5 Average pile-up profiles measured by ATLAS during Run 2 [33]. Higher levels of pile-up are planned for Run 3.	34
2960	3.6 A 3D model of the entire ATLAS detector [40]. The detector is 46 m long and 25 m in diameter. Cutouts to the centre of the detector reveal the different subdetectors which are arranged in concentric layers around the nominal interaction point.	35
2964	3.7 A 3D model of the ATLAS ID, made up of the pixel and SCT subdetectors, showing the barrel layers and end-cap disks [43].	36
2966	3.8 A cross-sectional view of the ATLAS ID, with the radii of the different barrel layers shown [36].	37
2968	3.9 A schematic cross-sectional view of the ATLAS IBL [44].	38
2969	3.10 The ATLAS calorimeters [47]. The ECal uses LAr-based detectors, while the HCal uses mainly scintillating tile detectors. In the forward region the HCal also includes the LAr hadronic endcaps.	40
2972	3.11 The ATLAS muon spectrometer [50].	42
2973	3.12 Particles (left) which have enough separation will leave charge depositions which are resolved into separate clusters. Sufficiently close particles (right) can lead to merged clusters. Their combined energy deposits are recon- structed as a single merged cluster [55].	46
2977	3.13 A sketch of electron reconstruction using the ATLAS detector [72]. Electron reconstruction makes use of the entire ID and the calorimeters. In particular, discriminating information comes from the TRT and ECal.	49

2980	4.1	Diagram of a typical b -jet (blue) which has been produced in an event alongside two light jets (grey) [75]. The b -hadron has travelled a significant distance (pink dashed line) from the primary interaction point (pink dot) before its decay. The large transverse impact parameter d_0 is a characteristic property of the trajectories of b -hadron decay products.	53
2985	4.2	The truth b -hadron decay radius L_{xy} as a function of truth transverse momentum p_T for reconstructed b -jets in Z' events. Error bars show the standard deviation. The pixel layers are shown in dashed horizontal lines.	54
2988	4.3	At lower p_T (left) the decay length of the b -hadron is reduced, and the resulting decay tracks are less collimated. At higher p_T (right) the b -hadron decay length increases and the resulting decay tracks are more collimated and have less distance over which to diverge before reaching detector elements. As a result, the ID may be unable to resolve charged depositions from different particles, instead reconstructing merged clusters.	55
2994	4.4	Hit multiplicities on the IBL (left) and the pixel layers (right) as a function of the p_T of the reconstructed track. Tracks from the weak decay of the b -hadron are shown in red, while fragmentation tracks (which are prompt) are in blue. For each of these, standard tracks and pseudo-tracks are plotted. Hit multiplicities on the pseudo-tracks at high p_T due to the increased flight of the b -hadron. The baseline tracks have more hits than the pseudo-tracks, indicating that they are being incorrectly assigned additional hits.	57
3001	4.5	b -hadron decay track reconstruction efficiency as a function of truth b -hadron p_T [79]. Nominal track reconstruction is shown in black, while the track reconstruction efficiency for track candidates (i.e. the pre-ambiguity solver efficiency) is shown in green. For high- p_T b -hadrons, the ambiguity solver is overly aggressive in its removal of b -hadron decay tracks. Suggestions for the improvement of the track reconstruction efficiency in this regime by the loosening of cuts in the ambiguity solver are shown in blue and red.	57
3008	4.6	The rate of shared hits on b -hadron decay tracks on the IBL (left), and the B-layer (right), as a function of the production radius of the b -hadron decay product. Pseudo-tracks represent ideal performance given the ATLAS detector, and given also the efficiency of the NN cluster splitting algorithms.	60

3012	4.7 Profiles, as a function of parent b -hadron p_T , of good (left) and wrong (right) hit assignment rates on the IBL for tracks using baseline tracking (black), the modified version of the outlier removal procedure (red).	62
3015	4.8 (left) B hadron decay track d_0 pulls for baseline and modified GX2F tracks. (right) The magnitude of the decay track d_0 pull as a function of B hadron transverse momentum.	63
3018	5.1 A diagram displaying the logical flow of a single neuron with three inputs x_i^j . Each input is multiplied by a weight θ_j , and the resulting values are summed. A bias term θ_0 is added, and the result is passed to an activation function. Each neuron can be thought of as a logistic regression model.	66
3022	5.2 Several common choices for the activation function g of an artificial neuron.	67
3023	5.3 Rate of fake tracks as a function of jet transverse momentum (left) and $\Delta R(\text{track}, \text{jet})$ (right). The rate of fake tracks increases significantly as a function of p_T , and also increases as the distance to the jet axis decreases, and the number of tracks in the jet increases (not shown).	70
3027	5.4 The light-jet efficiency of the low level tagger SV1 as a function of b -jet efficiency for the nominal tracking setup (black) and for the case where fake tracks which are not from the decay of a b -hadron are removed. The light-jet efficiency is decreased, demonstrating that the presence of fake tracks is detrimental to algorithm performance.	71
3032	5.5 (left) Normalised histogram of the model output separated for good and fake tracks, and further separated by those tracks which are from the decay of a b -hadron. (right) The ROC curve for all tracks (solid line) and tracks from the decay of a b -hadron (dashed line).	74
3036	5.6 The effect of applying the fake track identification algorithm alongside the b -hadron decay track identification on the jet tagging performance of SV1 for jets with $250 \text{ GeV} < p_T < 400 \text{ GeV}$ (left) and for jets with $400 \text{ GeV} < p_T < 1 \text{ TeV}$ (right). The nominal SV1 light-jet rejection (black) is compared to two working points, labelled “A” (red) and “B” (orange) of fake track removal, which represent two different 2D working points of the track classification tools. Removal of fake tracks based on truth information is shown by the green curves.	76

3044	5.7 The effect of applying the fake track identification algorithm alongside 3045 the b -hadron decay track identification on the jet tagging performance 3046 of SV1 for jets with $250 \text{ GeV} < p_T < 400 \text{ GeV}$ (left) and for jets with 3047 $400 \text{ GeV} < p_T < 1 \text{ TeV}$ (right). The nominal SV1 light-jet rejection (black) 3048 is compared to two working points of fake track removal (orange and red). 3049 Removal of fake tracks based on truth information is shown by the green 3050 curves.	77
3051	6.1 Comparison of the existing flavour tagging scheme (left) and GN1 (right). 3052 The existing approach utilises low-level algorithms (shown in blue), the 3053 outputs of which are fed into a high-level algorithm (DL1r). Instead 3054 of being used to guide the design of the manually optimised algorithms, 3055 additional truth information from the simulation is now being used as 3056 auxiliary training targets for GN1. The solid lines represent reconstructed 3057 information, whereas the dashed lines represent truth information.	81
3058	6.2 The flow of information through a graph neural network layer for (left) a full 3059 implementation of the layer and (right) a deep sets model [114]. Reproduced 3060 from Ref. [113].	84
3061	6.3 The inputs to GN1 are the two jet features ($n_{\text{jf}} = 2$), and an array of 3062 n_{tracks} , where each track is described by 21 track features ($n_{\text{tf}} = 21$). The 3063 jet features are copied for each of the tracks, and the combined jet-track 3064 vectors of length 23 form the inputs of GN1.	89
3065	6.4 The network architecture of GN1. Inputs are fed into a per-track initialisa- 3066 tion network, which outputs an initial latent representation of each track. 3067 These representations are then used to populate the node features of a 3068 fully connected graph network. After the graph network, the resulting node 3069 representations are used to predict the jet flavour, the track origins, and 3070 the track-pair vertex compatibility.	90
3071	6.5 Comparison between the DL1r and GN1 b -tagging discriminant D_b for 3072 jets in the $t\bar{t}$ sample. The 85% WP and the 60% WP are marked by the 3073 solid (dashed) lines for GN1 (DL1r), representing respectively the loosest 3074 and tightest WPs used by analyses. A value of $f_c = 0.018$ is used in the 3075 calculation of D_b for DL1r and $f_c = 0.05$ is used for GN1. The distributions 3076 of the different jet flavours have been normalised to unity area.	95

3077	6.6 The c -jet (left) and light-jet (right) rejections as a function of the b -jet tagging efficiency for jets in the $t\bar{t}$ sample with $20 < p_T < 250$ GeV. The ratio with respect to the performance of the DL1r algorithm is shown in the bottom panels. A value of $f_c = 0.018$ is used in the calculation of D_b for DL1r and $f_c = 0.05$ is used for GN1 and GN1Lep. Binomial error bands are denoted by the shaded regions. At b -jet tagging efficiencies less than $\sim 75\%$, the light-jet rejection becomes so large that the effect of the low number of jets is visible. The lower x -axis range is chosen to display the b -jet tagging efficiencies usually probed in these regions of phase space.	97
3086	6.7 The c -jet (left) and light-jet (right) rejections as a function of the b -jet tagging efficiency for jets in the Z' sample with $250 < p_T < 5000$ GeV. The ratio with respect to the performance of the DL1r algorithm is shown in the bottom panels. A value of $f_c = 0.018$ is used in the calculation of D_b for DL1r and $f_c = 0.05$ is used for GN1 and GN1Lep. Binomial error bands are denoted by the shaded regions. At b -jet tagging efficiencies less than $\sim 20\%$, the light-jet rejection becomes so large that the effect of the low number of jets is visible. The lower x -axis range is chosen to display the b -jet tagging efficiencies usually probed in these regions of phase space.	98
3095	6.8 The b -jet tagging efficiency for jets in the $t\bar{t}$ sample (left) and jets in the Z' sample (right) as a function of jet p_T with a fixed light-jet rejection of 100 in each bin. A value of $f_c = 0.018$ is used in the calculation of D_b for DL1r and $f_c = 0.05$ is used for GN1 and GN1Lep. GN1 demonstrates improved performance with respect to DL1r across the p_T range shown. Binomial error bands are denoted by the shaded regions.	99
3101	6.9 The b -jet (left) and light-jet (right) rejections as a function of the c -jet tagging efficiency for $t\bar{t}$ jets with $20 < p_T < 250$ GeV. The ratio to the performance of the DL1r algorithm is shown in the bottom panels. Binomial error bands are denoted by the shaded regions. At c -jet tagging efficiencies less than $\sim 25\%$, the light-jet rejection becomes so large that the effect of the low number of jets is visible. The lower x -axis range is chosen to display the c -jet tagging efficiencies usually probed in these regions of phase space.	101

3108	6.10 The b -jet (left) and light-jet (right) rejections as a function of the c -jet tagging efficiency for Z' jets with $250 < p_T < 5000$ GeV. The ratio to the performance of the DL1r algorithm is shown in the bottom panels. Binomial error bands are denoted by the shaded regions. The lower x -axis range is chosen to display the c -jet tagging efficiencies usually probed in these regions of phase space.	101
3114	6.11 A schematic showing the truth track origin and vertex information (left) compared with the predictions from GN1 (right). Vertices reconstructed by SV1 and JetFitter are also marked. Class probabilities p_b , p_c and p_u are rounded to three significant figures. GN1 improves over SV1 and JetFitter by successfully determining the origins and vertex compatibility of all the tracks in the jet with the exception of the truth OtherSecondary track, which is misidentified as pileup.	103
3121	6.12 A schematic showing the truth track origin and vertex information (left) compared with the predictions from GN1 (right). Vertices reconstructed by SV1 and JetFitter are also marked. Class probabilities p_b , p_c and p_u are rounded to three significant figures.	103
3125	6.13 The c -jet (left) and light-jet (right) rejections as a function of the b -jet tagging efficiency for $t\bar{t}$ jets with $20 < p_T < 250$ GeV, for the nominal GN1, in addition to configurations where no (GN1 No Aux), only the track classification (GN1 TC) or only the vertexing (GN1 Vert) auxiliary objectives are deployed. The ratio to the performance of the DL1r algorithm is shown in the bottom panels. A value of $f_c = 0.018$ is used in the calculation of D_b for DL1r and $f_c = 0.05$ is used for GN1. Binomial error bands are denoted by the shaded regions. At b -jet tagging efficiencies less than $\sim 65\%$, the light-jet rejection become so large that the effect of the low number of jets are visible. The lower x -axis range is chosen to display the b -jet tagging efficiencies usually probed in these regions.	105

3136	6.14 The c -jet (left) and light-jet (right) rejections as a function of the b -jet 3137 tagging efficiency for Z' jets with $250 < p_T < 5000$ GeV, for the nominal 3138 GN1, in addition to configurations where no (GN1 No Aux), only the track 3139 classification (GN1 TC) or only the vertexing (GN1 Vert) auxiliary objectives 3140 are deployed. The ratio to the performance of the DL1r algorithm is shown 3141 in the bottom panels. A value of $f_c = 0.018$ is used in the calculation of D_b 3142 for DL1r and $f_c = 0.05$ is used for GN1. Binomial error bands are denoted 3143 by the shaded regions. At b -jet tagging efficiencies less than $\sim 25\%$, the 3144 light-jet rejection become so large that the effect of the low number of jets 3145 are visible. The lower x -axis range is chosen to display the b -jet tagging 3146 efficiencies usually probed in these regions.	106
3147	6.15 Vertex finding efficiency as a function of jet p_T for b -jets in the $t\bar{t}$ sample 3148 using the exclusive (left) and inclusive (right) vertex finding approaches. 3149 Efficient vertex finding requires the recall of at least 65% of the tracks in 3150 the truth vertex, and allows no more than 50% of the tracks to be included 3151 incorrectly. Binomial error bands are denoted by the shaded regions.	109
3152	6.16 Inclusive vertex finding efficiency for multitrack truth vertices in b -jets in 3153 the $t\bar{t}$ sample (left) and jets in the Z' sample (right) as a function of jet p_T . 3154 Efficient vertex finding requires the recall of at least 65% of the tracks in 3155 the truth vertex, and allows no more than 50% of the tracks to be included 3156 incorrectly.	110
3157	6.17 ROC curves for the different groups of truth origin labels defined in Table 5.1 3158 for jets in the $t\bar{t}$ sample (left) and jets in the Z' sample (right). The 3159 FromB, FromBC and FromC labels have been combined, weighted by their 3160 relative abundance, into the Heavy Flavour category, and the Primary and 3161 OtherSecondary labels have similarly been combined into a single category. 3162 The mean weighted area under the ROC curves (AUC) is similar for both 3163 samples.	112
3164	6.18 The c -jet (left) and light-jet (right) rejections as a function of the b -jet 3165 tagging efficiency for $t\bar{t}$ jets with $20 < p_T < 250$ GeV, for the looser track 3166 selection trainings of GN1. The ratio to the performance of the DL1d 3167 algorithm is shown in the bottom panels. A value of $f_c = 0.018$ is used in 3168 the calculation of D_b for DL1d and $f_c = 0.05$ is used for GN1. Binomial 3169 error bands are denoted by the shaded regions.	114

3170	6.19 The c -jet (left) and light-jet (right) rejections as a function of the b -jet tagging efficiency for Z' jets with $250 < p_T < 5000$ GeV, for the looser track selection trainings of GN1. The ratio to the performance of the DL1d algorithm is shown in the bottom panels. A value of $f_c = 0.018$ is used in the calculation of D_b for DL1d and $f_c = 0.05$ is used for GN1. Binomial error bands are denoted by the shaded regions.	116
3176	7.1 Diagrams of the signal process (top) and the 0-lepton and 1-lepton $t\bar{t}$ back- grounds (middle, bottom). Object to the right of centre are reconstructed within the large- R jet. For the backgrounds, the large- R jet contains a mis-tagged c - or light-jet.	126
3180	7.2 Normalised leading large- R jet mass distribution from Z and $W+hf$ pro- cesses in the HP SR of the 0-lepton channel. The renormalisation scale μ_r has been varied by a factor of 2 (1up) and 0.5 (1down). An exponential function is fitted to the ratio between the nominal and variation samples.	136
3184	7.3 The comparison on m_J shapes between SHERPA and MADGRAPH samples from $V+hf$ process in p_T^V inclusive signal regions. The Kolmogorov-Smirnov test and χ^2/ndf are shown on the plots.	137
3187	7.4 Normalised leading large- R jet mass distribution from WZ and ZZ process, merged among all the signal regions and lepton channels. The renormalisa- tion scale μ_R has been varied by a factor of 2 (1up) and 0.5 (1down). The red line shape shows the fitting results of the hyperbolic tangent function.	139
3191	7.5 The comparison on m_J shapes between SHERPA and POWHEG+PYTHIA 8 samples from WZ and ZZ process in high and low purity signal regions. p_T^V regions and 0- and 1-lepton channels are merged. The dashed green line shows the fitted third order polynomial function and the blue lines show the function after a protection is added in the high mass region.	140

3196	7.6 The m_J post-fit distributions in (top) the 0-, (middle) 1- and (bottom) 3197 2-lepton SRs for (left) $250 \text{ GeV} < p_T^V < 400 \text{ GeV}$ and (right) $p_T^V \geq 400 \text{ GeV}$. 3198 The LP and HP regions are merged for the 0-lepton and 1-lepton channels. 3199 The fitted background contributions are shown as filled histograms. The 3200 Higgs boson signal ($m_H = 125 \text{ GeV}$) is shown as a filled histogram and 3201 is normalised to the signal yield extracted from data ($\mu_{VH}^{bb} = 0.72$), and 3202 as an unstacked unfilled histogram, scaled by the SM prediction times a 3203 factor of two. The size of the combined on the sum of the fitted signal and 3204 background is shown in the hatched band. The highest bin contains the 3205 overflow.	146
3206	7.7 The m_J post-fit distributions in the $t\bar{t}$ control region for (top) the 0-lepton 3207 channel and the 1-lepton channel for $250 \text{ GeV} < p_T^V < 400 \text{ GeV}$ and (bot- 3208 tom) the 0-lepton channel and the 1-lepton channel for $p_T^V > 400 \text{ GeV}$. 3209 The background contributions after the likelihood fit are shown as filled 3210 histograms. The Higgs boson signal ($m_h = 125 \text{ GeV}$) is shown as a filled 3211 histogram on top of the fitted backgrounds normalised to the signal yield 3212 extracted from data ($\mu_{VH}^{bb} = 0.72$), and unstacked as an unfilled histogram, 3213 scaled by the SM prediction times a factor of 2. The size of the combined 3214 statistical and systematic uncertainty for the sum of the fitted signal and 3215 background is indicated by the hatched band. The highest bin in the 3216 distributions contains the overflow.	147
3217	7.8 m_J distribution in data after subtraction of all backgrounds except for the 3218 WZ and ZZ diboson processes. The contributions from all lepton channels 3219 and signal regions are summed and weighted by their respective values of 3220 the ratio of fitted Higgs boson signal and background yields. The expected 3221 contribution of the associated WH and ZH production of a SM Higgs 3222 boson with $m_H = 125 \text{ GeV}$ is shown scaled by the measured combined 3223 signal strength ($\mu_{VH}^{bb} = 0.72$). The diboson contribution is normalised to 3224 its best-fit value of $\mu_{VZ}^{bb} = 0.91$. The size of the combined statistical and 3225 systematic uncertainty is indicated by the hatched band. This error band is 3226 computed from a full signal-plus-background fit including all the systematic 3227 uncertainties defined in Section 7.2, except for the VH/VZ experimental 3228 and theory uncertainties.	148

3229	7.9 Signal strength compatibility test between the (3+1)-POI fit (with the three	
3230	lepton channels splitted) and the default (1+1)-POI fit. The compatibility	
3231	of the three channels is evaluated via a χ^2 difference test and results in a	
3232	p-value of 49%.	149
3233	7.10 Impact of systematic uncertainties on the fitted VH signal-strength pa-	
3234	rameter μ_{VH}^{bb} sorted in decreasing order. The boxes show the variations	
3235	of $\hat{\mu}$, referring to the top x -axis, when fixing the corresponding individual	
3236	nuisance parameter to its post-fit value modified upwards or downwards by	
3237	its post-fit uncertainty, i.e. $\hat{\theta} \pm \sigma_{\hat{\theta}}$, and repeating the fit. The impact of	
3238	up- and down-variations can be distinguished via the dashed and plane box	
3239	fillings. The yellow boxes show the pre-fit impact (top x -axis) by varying	
3240	each nuisance parameter by ± 1 . The filled circles show the deviation of the	
3241	fitted value for each nuisance parameter, $\hat{\theta}$, from their nominal input value	
3242	θ_0 expressed in standard deviations with respect to their nominal uncer-	
3243	tainties $\Delta\theta$ (bottom x -axis). The error bars show the post-fit uncertainties	
3244	on $\hat{\theta}$ with respect to their nominal uncertainties. The open circles show	
3245	the fitted values and uncertainties of the normalization parameters that are	
3246	freely floating in the fit. Pre-fit, these parameters have a value of one.	151

3247 List of tables

<small>3248</small>	2.1 The fermions of the SM [14]. Three generations of particles are present. Also present (unlisted) are the antiparticles, which are identical to the particles up to a reversed charge sign.	<small>14</small>
<small>3249</small>		
<small>3250</small>		
<small>3251</small>	2.2 The bosons of the SM [14]. The photon, weak bosons and gluons are gauge bosons arising from gauge symmetries, and carry the four fundamental forces of the SM. The recently discovered Higgs boson is the only fundamental scalar particle in the SM.	<small>15</small>
<small>3252</small>		
<small>3253</small>		
<small>3254</small>		
<small>3255</small>	3.1 Overview of the different LHC runs [32, 33]. The average number of interactions per bunch-crossing is denoted as $\langle \mu \rangle$ (see Section 3.2.3), and is here averaged over the entire run. Numbers for Run 3 are preliminary and are only provided to give an indication of expected performance.	<small>28</small>
<small>3256</small>		
<small>3257</small>		
<small>3258</small>		
<small>3259</small>	5.1 Truth origins which are used to categorise the physics process that led to the production of a track. Tracks are matched to charged particles using the truth-matching probability [55]. A truth-matching probability of less than 0.5 indicates that reconstructed track parameters are likely to be mismeasured and may not correspond to the trajectory of a single charged particle. The “OtherSecondary” origin includes tracks from photon conversions, K_S^0 and Λ^0 decays, and hadronic interactions.	<small>69</small>
<small>3260</small>		
<small>3261</small>		
<small>3262</small>		
<small>3263</small>		
<small>3264</small>		
<small>3265</small>		
<small>3266</small>	5.2 Input features to the fake track classification NN. Basic jet kinematics, along with information about the reconstructed track parameters and constituent hits are used. Shared hits, are hits used on multiple tracks which have not been classified as split by the cluster-splitting neural networks [55], while split hits are hits used on multiple tracks which have been identified as merged.	<small>73</small>
<small>3267</small>		
<small>3268</small>		
<small>3269</small>		
<small>3270</small>		
<small>3271</small>		

3272	5.3 Quality selections applied to tracks, where d_0 is the transverse IP of the track, z_0 is the longitudinal IP with respect to the PV and θ is the track polar angle. Shared hits are hits used on multiple tracks which have not been classified as split by the cluster-splitting neural networks [55]. Shared hits on pixel layers are given a weight of 1, while shared hits in the SCT are given a weight of 0.5. A hole is a missing hit, where one is expected, on a layer between two other hits on a track.	74
3279	5.4 Good and fake track selection efficiencies for the combined $t\bar{t}$ and Z' samples. Two working points are defined, cutting on the NN output at 0.06 and 0.12. The continuous output of the model allows for the tuning of good and fake track identification efficiencies.	75
3283	6.1 Input features to the GN1 model. Basic jet kinematics, along with information about the reconstructed track parameters and constituent hits are used. Shared hits, are hits used on multiple tracks which have not been classified as split by the cluster-splitting neural networks [55], while split hits are hits used on multiple tracks which have been identified as merged. A hole is a missing hit, where one is expected, on a layer between two other hits on a track. The track leptonID is an additional input to the GN1Lep model.	87
3290	6.2 A summary of GN1's different classification networks used for the different training objectives. The hidden layers column contains a list specifying the number of neurons in each layer.	91
3293	6.3 The area under the ROC curves (AUC) for the track classification from GN1, compared to a standard multilayer perceptron (MLP) trained on a per-track basis. The unweighted mean AUC over the origin classes and weighted mean AUC (using as a weight the fraction of tracks from the given origin) is provided. GN1, which uses an architecture that allows track origins to be classified in a conditional manner as discussed in Section 6.4.3, outperforms the MLP model for both $t\bar{t}$ and Z' jets.	112
3300	7.1 Summary of the definition of the analysis regions. Signal enriched regions are marked with the label SR. There are regions with relatively large signal purity (HP SR) and with low purity (LP SR). Background enriched regions are marked with the label CR. The shorthand “add” stands for additional small- R jets, i.e. number of small- R jets not matched to the Higgs-jet candidate.	120

3306	7.2 Signal and background processes with the corresponding generators used for the nominal samples. If not specified, the order of the cross-section calculation refers to the expansion in the strong coupling constant (α_s). (★) The events were generated using the first PDF in the NNPDF3.0NLO set and subsequently reweighted to the PDF4LHC15NLO set [156] using the internal algorithm in POWHEG-Box v2. (†) The NNLO(QCD)+NLO(EW) cross-section calculation for the $pp \rightarrow ZH$ process already includes the $gg \rightarrow ZH$ contribution. The $qq \rightarrow ZH$ process is normalised using the cross-section for the $pp \rightarrow ZH$ process, after subtracting the $gg \rightarrow ZH$ contribution. An additional scale factor is applied to the $qq \rightarrow VH$ processes as a function of the transverse momentum of the vector boson, to account for electroweak (EW) corrections at NLO. This makes use of the VH differential cross-section computed with HAWK [157, 158].	122
3318	7.3 Event selection requirements for the boosted VH , $H \rightarrow b\bar{b}$ analysis channels and sub-channels. Various channel dependent selections are used to maximise the signal efficiency and reduce the number of background events in each analysis region.	124
3322	7.4 Different sources of uncertainty (i.e. variations in the model) considered for the $V+jets$ background, and the corresponding implementation. For each uncertainty, acceptance and shape uncertainties are derived.	130
3325	7.5 0-lepton $W+jets$ nominal sample flavour composition and total event yield. . .	132
3326	7.6 1-lepton $W+jets$ nominal sample flavour composition and total event yield. . .	132
3327	7.7 0-lepton $Z+jets$ nominal sample flavour composition and total event yield. . .	132
3328	7.8 2-lepton $Z+jets$ nominal sample flavour composition and total event yield. . .	132
3329	7.9 $V+jets$ acceptance uncertainties. $W+jets$ SR and CR uncertainties marked with a superscript † are correlated. The 1L $W+jets$ H/M uncertainty marked by * is applied as independent and uncorrelated NPs in both HP and LP signal regions. The 0L $W+jets$ Wbb Norm uncertainty is only applied when a floating normalisation for Wbb cannot be obtained from the 1L channel. A 30% uncertainty for $Z \rightarrow b\bar{b}$ norm is applied in the 1L channel when a floating normalisation for $Z \rightarrow b\bar{b}$ cannot be obtained from the 0L or 2L channels.	134

3337	7.10 Diboson acceptance uncertainties. All uncertainties except channel extrapolation uncertainties are fully correlated between ZZ and WZ processes and channels.	139
3340	7.11 Factors applied to the nominal normalisations of the $t\bar{t}$, $W+\text{hf}$, and $Z+\text{hf}$ backgrounds, as obtained from the likelihood fit. The errors represent the combined statistical and systematic uncertainties.	144
3343	7.12 Breakdown of the observed absolute contributions to the uncertainty on the signal strength μ_{VH}^{bb} obtained from the (1+1)-POI fit. The average impact represents the average between the positive and negative uncertainties on μ_{VH}^{bb} . The sum in quadrature of the systematic uncertainties attached to the categories differs from the total systematic uncertainty due to correlations.	153